Contribution of tectonic processes to the exhumation of the Cycladic blueschist unit, Greece and Turkey

Dissertation
zur Erlangung des Grades
Doktor der Naturwissenschaften

am Fachbereich Geowissenschaften
der Johannes Gutenberg-Universität Mainz

Christine Maria Kumerics
geb. am 11.10.1974 in Wiesbaden

Mainz, 2004

Erklärung

Ich versichere hiermit, die vorliegende Arbeit selbständig und nur unter Verwendung der angegebenen Quellen und Hilfsmittel verfaßt zu haben.

All views and results presented in this thesis are those of the author, unless stated otherwise.

Mainz, November 2004

Tag der mündlichen Prüfung: 28.01.2005

Summary

In this study structural, metamorphic and geochronological data are used to quantify how the different tectonic exhumation processes, such as normal faulting and vertical ductile thinning, contribute to the overall exhumation of the deeply buried Cycladic blueschist unit in the Aegean and western Turkey. Additionally, the data allow an elucidation of the evolution of the extensional fault system on Ikaria Island and an evaluation of the tectonic significance of extensional shearing.

A finite-strain analysis with the R_f/ϕ method on samples of the Cycladic blueschist unit in the Aegean and western Turkey demonstrates how much vertical ductile thinning contributed to the total exhumation of the high-pressure rocks to the surface. The samples indicate principal stretches of S_X:S_Y:S_Z = 1.24:1.06:0.70. Calculations with a one-dimensional numerical model of Feehan and Brandon (1999), which integrates velocity gradients along a vertical flow path with a steady-state wedge, suggest that ductile thinning contributed only ~10% to the total exhumation. The proposition made by Platt et al. (1998) that vertical ductile thinning of 75% exhumed deep-seated high-pressure metamorphic rocks very quickly at rates of 4.5 km Myr^{-1} in the Alboran Sea is considered unrealistic. The rocks have a similar tectonic position as the Cycladic blueschist unit in the Aegean Sea, which allows the comparison of both regions. A backcalculation of the finite vertical shortening and the finite maximum extension in the Alboran Sea with the one-dimensional numerical model indicates that, assuming plane-strain constant-volume deformation, the high-grade rocks must have a S_Z of 0.03 to account for a total of 97% of vertical ductile thinning of their overburden. Thus, the calculated value for the maximum stretch S_X must be at least 30. Such values are considered unrealistic.

Kinematic, metamorphic and geochronological data elucidate the tectonic nature and evolution of the ductile extensional Messaria shear zone and the associated brittle Messaria and Fanari detachment faults. A matter of debate in extensional ductile shear zones is how much exhumation was caused by ductile flow associated with a subhorizontal foliation relative to faulting-related exhumation. Numerous deformed pegmatite veins in the Messaria shear zone allow the reconstruction of deformation and flow parameters. The mean kinematic vorticity number, W_m, ranges from 0.13 to 0.69 indicating that shearing deviated significantly from simple shear and that vertical ductile thinning occurred in the subhorizontal shear zone. Thermobarometric data show that the greenschist-facies Messaria shear zone formed at 3-4 kbar and 350-400°C at a depth of ~15 km. Zircon and apatite fission track and apatite (U-Th)/He ages demonstrate rapid cooling in the footwall of the Messaria shear zone between 11-3 Ma. The data indicate that the Messaria shear zone and the Messaria detachment slipped at

fast rates of ~7-8 km Myr^{-1}. Age data obtained by different dating methods imply that ductile deformation in the Messaria shear zone occurred at ~11 Ma. Calculations with the Feehan and Brandon model (1999) demonstrate that ductile flow contributed only ~20% to exhumation during extensional shearing.

A significant amount of exhumation of the Cycladic blueschist unit is attributed to Late Miocene low-angle normal fault detachments, which are well documented on several islands in the Aegean (Buick 1991; Kumerics et al. 2004; Vandenberg & Lister 1996; Avigad & Garfunkel 1989; Lee & Lister 1992; Lister & Foster 1996; Ring et al. 2003). However, the late-stage normal faults accomplished only the final ~5-15 km of the overall exhumation of the high-pressure rocks. Thus, a certain amount of exhumation of the Cycladic blueschist unit must have occurred before the Miocene. This exhumation in early orogenic phases occurred by an extrusion wedge in western Turkey, whose basal thrusting was coeval with the normal faulting at its top. $^{40}Ar/^{39}Ar$ and $^{87}Rb/^{86}Sr$ dating of mylonite of the normal fault contact between the Selçuk nappe and the underlying Ampelos/Dilek nappe of the Cycladic blueschist unit as well as of the thrust contact between the Ampelos/Dilek nappe and the underlying Menderes nappes shows that both mylonite zones formed at ~35 Ma. Available P-T data show that ~30-35 km of exhumation of the Ampelos/Dilek nappe of the Cycladic blueschist unit was accomplished in this Late Eocene/Early Oligocene extrusion wedge.

The results imply that the bulk of exhumation of the Cycladic blueschist unit in western Turkey occurred in early orogenic phases by a Late Eocene/Early Oligocene extrusion wedge. Late-stage Miocene low-angle normal faults exhumed the high-pressure rocks from mid-crustal depths. Vertical ductile thinning does not appear to be an important exhumation process.

Zusammenfassung

In dieser Studie werden strukturgeologische, metamorphe und geochronologische Daten benutzt, um eine Quantifizierung verschiedener tektonischer Prozesse vorzunehmen, die für die Exhumierung der Kykladischen Blauschiefereinheit in der Ägäis und der Westtürkei verantwortlich waren. Bei den beiden tektonischen Prozessen handelt es sich um: (1) Abschiebungen und (2) vertikale duktile Ausdünnung. Die Daten geben zudem sowohl Aufschluß über die Evolution des Extensionsstörungssystems auf der Insel Ikaria in der östlichen Ägäis als auch eine Evaluierung der tektonischen Bedeutung von Extensionsstörungen.

Eine finite Verformungsanalyse an Proben der Kykladischen Blauschiefereinheit in der Ägäis und der Westtürkei mit der R_f/ϕ-Method ermöglicht eine Abschätzung des Beitrags von vertikaler duktiler Ausdünnung an der gesamten Exhumierung der Hochdruckgesteine. Die Proben weisen prinzipielle Streckungen von $S_X{:}S_Y{:}S_Z$ = 1.24:1.06:0.70 auf. Kalkulationen mit einem eindimensionalen, numerischen Model von Feehan und Brandon (1999), das Geschwindigkeitsgradienten entlang eines vertikalen Fließpfades mit einem Gleichgewichts-Orogenkeil integriert, zeigt, daß duktile Ausdünnung nur ca. 10% an der gesamten Exhumierung ausmacht. Die Behauptung von Platt et al. (1998), daß vertikale Ausdünnung von ca. 75% die Hochdruckgesteine in der Alboran See mit einer Rate von 4.5 km/Ma exhumierte, wird als unrealistisch angesehen. Die Gesteine in der Alboran See haben eine ähnliche tektonische Position wie die Kykladische Blauschiefereinheit in der Ägäis, was den Vergleich beider Regionen erlaubt. Eine Rückkalkulation der finiten vertikalen Verkürzung und der finiten maximalen Extension in der Alboran See mit dem eindimensionalen, numerischen Model zeigt (bei angenommener planarer Verformung und konstanter Volumensverformung), daß die Hochdruckgesteine eine vertikale Verkürzung von S_Z = 0.03 aufweisen müßten, damit eine vertikale duktile Ausdünnung von 97% erklärt werden kann. Der kalkulierte Wert für die maximale Extension S_X liegt bei mindestens 30. Solche Werte werden als unrealistisch erachtet.

Kinematische, metamorphe und geochronologische Daten erklären die tektonische Natur und die Evolution der duktilen Messaria Scherzone und der assoziierten spröden Messaria und Fanari Abschiebungen. Generell steht bei duktilen Extensionsscherzonen zur Debatte, welchen Beitrag vertikale duktile Ausdünnung, die mit subhorizontaler Foliation verbunden ist, zur Exhumierung leistet. Zahlreiche deformierte Pegmatitadern in der Messaria Scherzone erlauben die Rekonstruktion von Verformungs- und Fließparametern. Die durchschnittliche kinematische Drehzahl, W_m, erstreckt sich von 0.13 bis 0.69 und beweist, daß die Scherung

deutlich von einfacher Scherung abweicht und vertikale duktile Ausdünnung in subhorizontalen Scherzonen stattfindet. Kalkulationen mit dem Feehan und Brandon Model (1999) zeigen, daß während der Extensionsscherung duktiles Fließen nur einen Beitrag von ca. 20% zur gesamten Exhumierung leistete. Thermobarometrische Daten lassen erkennen, daß sich die grünschieferfazielle Messaria Scherzone bei einem Druck von 3-4 kbar und einer Temperatur von 350-400°C bildete, was einer Tiefe von ~15 km entspricht. Sowohl Apatit- und Zirkonspaltspurenalter als auch Apatit (U-Th)/He-Alter zeigen, daß es zwischen 11 und 3 Ma zu einer schnellen Abkühlung im Liegenden der Scherzone kam. Die Altersdaten lassen erkennen, daß die Messaria Scherzone und die Messaria Abschiebung mit einer rapiden Rate von ca. 7-8 km/Ma gleiten. Die schnell exhumierenden Störungen bewirken die Exhumierung der Gesteine des Liegenden aus ~15 km Tiefe. Ein bedeutender Anteil an der Exhumierung der Kykladischen Blauschiefereinheit wird den Spät-Miozänen flachen Abschiebungen beigemessen, die bereits auf einigen Insel in der Ägäis gut dokumentiert wurden (Buick 1991; Vandenberg & Lister 1996; Avigad & Garfunkel 1989; Lee & Lister 1992; Lister & Foster 1996; Ring et al. 2003a). Diese späten Abschiebungen tragen aber nur zur Exhumierung der letzten ~5-15 km der Hochdruckgesteine bei. Aus diesem Grund muß ein Großteil der Exhumierung der Kykladischen Blauschiefereinheit vor dem Miozän stattgefunden haben. Diese Exhumierung in frühen Orogenphasen wurde in der Westtürkei durch einen Extrusionskeil ermöglicht. Die Überschiebung an dessen Basis agierte gleichzeitig mit der Abschiebung im Hangendem. $^{40}Ar/^{39}Ar$ und $^{87}Rb/^{86}Sr$ Datierungen von Myloniten des Abschiebungskontaktes zwischen der Selçuk Decke und der darunterliegenden Ampelos/Dilek Decke der Kykladischen Blauschiefereinheit also auch des Überschiebungskontaktes zwischen der Ampelos/Dilek Decke und der darunterliegenden Menderes Decken zeigen, daß beide mylonitischen Scherzonen vor ~35 Ma entstanden. Vorliegende P-T-Daten geben Aufschluß darüber, daß ca. 30-35 km der Exhumierung der Ampelos/Dilek Decke mit Hilfe des Spät-Eozänen/Früh-Oligozänen Extrusionskeils ermöglicht wurde.

Die Resultate implizieren, daß ein Großteil der Exhumierung der Kykladischen Blauschiefereinheit in der Westtürkei in frühen Orogenphasen durch einen Spät-Eozänen/Früh-Oligozänen Extrusionskeil stattfand. Späte Miozäne flache Abschiebungen exhumierten die Hochdruckgesteine aus mittlerer Krustentiefe. Vertikale duktile Ausdünnung war kein signifikanter Exhumierungsprozeß.

Zusammenfassung für Fachfremde

Unser Forschungsgebiet liegt in der Ägäis und der Westtürkei. In der Ägäis driften die afrikanische und die europäische Platte aufeinander zu, wobei die afrikanische Platte aufgrund ihrer höheren Dicht unter die europäische Platte abtaucht. Zur gleichen Zeit schreitet die afrikanische Platte Richtung Süden zurück. Dieses Zurückschreiten beruht darauf, daß die Geschwindigkeitsrate, mit der die beiden Platten aufeinander zudriften, langsamer ist als die Abtauchrate der afrikanischen Platte. Die Folge ist eine Extension in der europäischen Platte, was zur Entstehung der Ägäischen See führte.

Auf einigen Ägäischen Inseln und in der westlichen Türkei findet man heute Gesteine, die unter hohem Druck und niedrigen Temperaturen in ca. 60 km Tiefe gebildet wurden und unter dem Begriff Kykladische Blauschiefereinheit zusammengefaßt werden. Das Ziel dieser Studie ist es, die verschiedenen Prozesse zu untersuchen, die dafür verantwortlich waren, diese Gesteine an die Erdoberfläche zu bringen (Exhumierung) und deren Gewichtung zu untersuchen. Es gibt dafür zwei wichtige Exhumierungsprozesse: (1) Verwerfungen und (2) vertikale duktile Ausdünnung (Abb. 1). Verwerfungen transportieren Material von auflagernden Gesteinsformationen ab und legen somit darunterliegende Gesteine frei. Vertikale duktile Ausdünnung bedeutet eine Verkürzung von Gesteinen durch plastische Verformung in der zur Erdoberfläche vertikalen Richtung.

Verformungsmessungen an Gesteinen der Kykladischen Blauschiefereinheit zeigen, daß die Gesteine nur gering vertikal verkürzt wurden. Hingegen tragen Verwerfungen, die sich im späten Miozän formten, einen Großteil zur Exhumierung der Kykladischen Blauschiefereinheit bei. Dies spiegeln auch bereits frühere Untersuchungen auf anderen Ägäischen Inseln wider. Allerdings wurde nur ein Teil der Kykladischen Blauschiefereinheit von diesen relativ jungen Verwerfungen exhumiert. Auf der Insel Ikaria, in der östlichen Ägäis, haben wir Verwerfungen, die durch Extension entstanden, genauer untersucht und deren Beitrag zur Exhumierung von Gesteinen diskutiert.

Frühere Studien zeigen, daß ein größerer Teil der Kykladischen Blauschiefereinheit bereits schon zu einem früheren Zeitpunkt exhumiert worden sein muß. In der Westtürkei gibt es Anzeichen für einen sogenannten Extrusionskeil, der sich im späten Eozän/frühen Oligozän formte und einen beträchtlichen Beitrag zur Exhumierung der Hochdruckgesteine leistete. Das typische Charakteristikum für einen solchen Extrusionskeil ist eine Verwerfung im oberen Teil des Keils und eine Überschiebung an der Basis des Keils, d.h. eine relative Aufwärtsbewegung einer Gesteinsscholle gegenüber der darunterliegenden (Abb. 2). Beide Kontakte müssen gleichzeitig agiert haben. Altersbestimmungen an Gesteinsproben des

oberen Verwerfungskontaktes als auch des unteren Überschiebungskontaktes belegen die Existenz eines Extrusionskeils in der Westtürkei.

Zusammenfassend kann gesagt werden, daß der Spät-Eozäne/Früh-Oligozäne Extrusionskeil und Spät-Miozäne Verwerfungen größtenteils für die Exhumierung der Kykladischen Blauschiefereinheit in der Ägäis und der Westtürkei verantwortlich waren. Vertikale duktile Ausdünnung leistete nur einen geringen Beitrag zur gesamten Exhumierung.

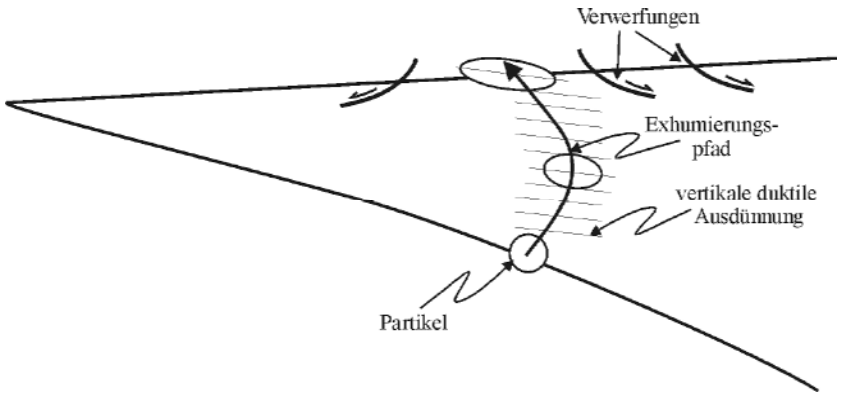

Abb. 1. Schematische Skizze zeigt die Vorgänge, die einen durch einen Orogenkeil entlang eines idealisierten Exhumierungspfades wandernden Partikel beeinflussen.

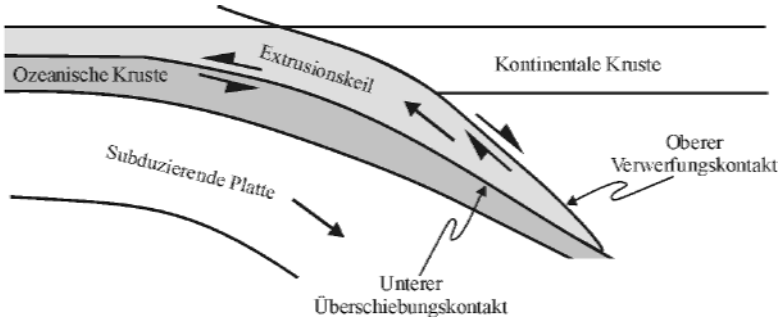

Abb. 2. Schematische Skizze eines Extrusionskeils.

Acknowledgements

My special thanks go to my supervisor, who guided me through my thesis and had always time for me. Many thanks go also to my colleagues for the collaboration. And I would like to thank my friends and my family for their help and constant assistance in many ways.

Table of content

Preface

This study aims at quantifying the contribution of tectonic processes to the exhumation of the deep-seated metamorphic rocks of the famous Cycladic blueschist unit in the Aegean and western Turkey. The two competing processes are (1) normal faulting and (2) vertical ductile thinning.

The Hellenic subduction zone in the Aegean is one of the best examples of a retreating plate-boundary zone. Some features of retreating subduction zones are extensional detachments forming intra arc and back arc basins and are exhuming deeply buried high-pressure rocks in the Late Miocene (Lister et al. 1984). It is to elucidate how much of the exhumation of the Cycladic blueschist unit in the Aegean and western Turkey is accomplished by these late-stage extensional detachments and the amount of exhumation, which vertical ductile thinning contributes to total exhumation. Earlier studies suggested that the Late Miocene low-angle normal faults did not cause much exhumation, but were important for the total exhumation process. A critical question is whether there are pre-Miocene extensional detachments and what their contribution to exhumation during the early orogenic history was.

The three chapters of this study imply that normal faulting was an important process for exhuming the Cycladic blueschist unit from mid-crustal depth to the surface. Vertical ductile thinning appears as an unimportant exhumation process. During early (i.e. pre-Miocene) orogenic phases an extrusion wedge exhumed a significant amount of the high-pressure rocks. All investigations are based on structural, metamorphic and geochronological data.

Chapter 1 discusses the contribution of vertical ductile thinning to the overall exhumation of high-pressure metamorphic rocks in the Aegean. The chapter comprises an evaluation of the proposition made by Platt et al. (1998), that vertical ductile thinning contributed a significant amount (~75%) to the exhumation of deeply buried rocks in the Alboran Sea, a setting which is similar to the Aegean. A finite-strain study in the Cycladic blueschist unit in the Aegean and western Turkey shows that vertical ductile thinning contributed only a small amount (~10%) to the total exhumation of the high-pressure rocks in the eastern Mediterranean.

Chapter 2 deals with the Late Miocene Messaria extensional fault system on Ikaria Island which was studied using kinematic, geochronological and metamorphic data for constraining the amount of exhumation achieved by the late-stage intra/back-arc extensional detachments in the Aegean. This work accrued in collaboration with some co-workers. S. Brichau provided the thermochronologic data of the islands of Ikaria and Samos, and the thermobarometric data for Ikaria Island have been produced by J.-L. Régnier. Both of them were colleagues of mine at the University of Mainz. J. Glodny of the GeoForschungsZentrum Potsdam dated two

samples with the $^{87}Rb/^{86}Sr$ method. The $^{40}Ar/^{39}Ar$ dating have been produced at the University of Montpellier, France, under the supervision of P. Monié.

Chapter 3 investigates the pre-Miocene exhumation of the Cycladic blueschist unit and provides evidence for a Late Eocene/Early Oligocene extrusion wedge in western Turkey that accomplished a significant amount (~30-35 km) to the exhumation of the Cycladic blueschist unit. $^{40}Ar/^{39}Ar$ and $^{87}Rb/^{86}Sr$ dating have been used to constrain the timing of the tectonic contacts and thus to prove the existence of an extrusion wedge. Co-workers for this study was again J. Glodny of the GeoForschungsZentrum Potsdam, who dated samples with the $^{87}Rb/^{86}Sr$ method. P. Monié advised the $^{40}Ar/^{39}Ar$ dating at the University of Montpellier, France.

Chapter 2 is the extended version of a manuscript submitted to 'Journal of Geological Society of London' entitled 'The extensional Messaria shear zone and associated brittle detachment faults, Aegean Sea, Greece'. Co-authors are U. Ring, S. Brichau, J.-L. Régnier, J. Glodny and P. Monié. Chapter 1 and 3 are written as manuscripts and shall be published in the near future.

Chapter 1

How contributes vertical ductile thinning to the total exhumation of the high-pressure rocks in the Mediterranean?

Abstract

In this study we evaluate the proposition that vertical ductile thinning of 75% exhumed deep-seated rocks very quickly at rates of 4.5 km Myr^{-1} in the Alboran Sea. The Aegean Sea in the eastern Mediterranean represents a similar tectonic setting as the Alboran Sea. Our study focuses on the Cycladic blueschist unit in the Aegean and western Turkey. We carried out a finite-strain analysis to elucidate how much vertical ductile thinning contributed to the total exhumation of the high-pressure rocks. Samples were collected on the Aegean islands of Sifnos, Syros, Tinos, Naxos and Samos and also from western Turkey. The R_f/ϕ method was used on one augen gneiss sample and on 13 conglomerates. The samples indicate principal stretches of $S_X = 1.27 - 2.76$, $S_Y = 0.71 - 1.07$ and $S_Z = 0.34 - 0.96$ with a tensor average of $S_X : S_Y : S_Z = 1.24 : 1.06 : 0.70$. A one-dimensional numerical model, which integrates velocity gradients along a vertical flow path with a steady-state wedge, is used to estimate the contribution of deformation to ductile thinning of the overburden during exhumation. Using a strain-rate law that is proportional with depth, our results show that ductile flow contributed only ~10% to the total exhumation, despite a vertical shortening strain of ~30%. Using the same model we backcalculate the finite vertical shortening in the high-pressure rocks from the Alboran Sea on which the above mentioned proposition was based. Assuming plane strain and constant volume deformation, we calculate principal stretches of $S_X = 30$ and $S_Z = 0.03$ (i.e. vertical shortening of 97%) that are needed, to produce a ductile thinning of 75%. We conclude that ductile thinning does not appear to be an important exhumation process.

Introduction

Deep-seated metamorphic rocks are commonly found in the interior of orogens. Subduction and crustal thickening can account for high-pressure metamorphism. The exhumation of these metamorphosed crustal rocks to the Earth's surface occurred by different processes, such as vertical ductile thinning, normal faulting and erosion. Ductile thinning is defined as the change in thickness of the overburden above a material point because of ductile deformation within that overburden and is associated with a subhorizontal foliation (Ring & Brandon 1999). In our study we focus specifically on a recently proposition by Platt et al. (1998) that

vertical ductile thinning is responsible for 75% at rates of 4.5 km Myr^{-1} of the exhumation of deeply buried rocks in the Alboran Sea. This proposition is in contrast to Ring et al. (1999a), who argued that exhumation by ductile thinning is generally operating at significantly slower rates.

The Mediterranean is a well-known example of subduction zone rollback at convergent plate margins (Fig. 1). The beginning of convergence between the African and European plates occurred in the Upper Cretaceous and continued throughout the Tertiary. This shortening process produced many collisional orogens like the Rif-Betic Cordillera in the western Mediterranean and the Hellenides in the eastern part. At the same time, the northward subduction of the African plate with associated subduction rollback to the south led to the onset of extension and caused the formation of back arc basins in the overriding plate (Lonergan & White 1997). Subduction zone rollback was controlled by the gravitational instability produced by subduction of cold and dense oceanic lithosphere (Rosenbaum et al. 2002), where the subduction rate is faster than the overall convergence rate. The late-orogenic Miocene extension, as documented in the Alboran Sea at the western end of the Mediterranean and in the Aegean Sea at the eastern end is best regarded as a consequence of such slab retreat. Therefore, it seems that the tectonic evolution of both regions is comparable.

Platt et al. (1998) assumed that homogeneous stretching of the whole lithosphere with associated vertical ductile thinning is exhuming high-pressure metamorphic rocks in the Alboran Sea. They base their assumption on the modeling of the P-T path (Fig. 2) obtained from the high-grade metamorphic rocks drilled at Ocean Drilling Program Site 976 (Fig. 3). They show that the only way to explain the P-T path (Fig. 2) is a combination of high postcollisional radiogenic heating combined with a significant postcontractional pause, wholesale removal of lithospheric mantle below the orogenic crust, followed by rapid stretching of the lithosphere.

From the Aegean is known that after a period of crustal thickening with the formation of high-pressure complexes, internal thrusts were reactivated as extensional structures, such as low-angle normal faults, which are primarily exhuming the high-pressure rocks to the surface (Lister et al. 1984). The contribution of vertical ductile thinning to exhumation is wholly unknown in the Aegean.

The purpose of this chapter is to evaluate the assumption made by Platt et al. (1998) in their modeling. Therefore, it is needed to backcalculate the finite vertical shortening and the finite maximum extension in the Alboran Sea. A finite-strain study on the Cycladic blueschist unit in the Aegean and western Turkey is carried out to obtain an estimate of how much vertical

ductile thinning contributed to the overall exhumation of high-pressure metamorphic rocks in the Aegean and western Turkey.

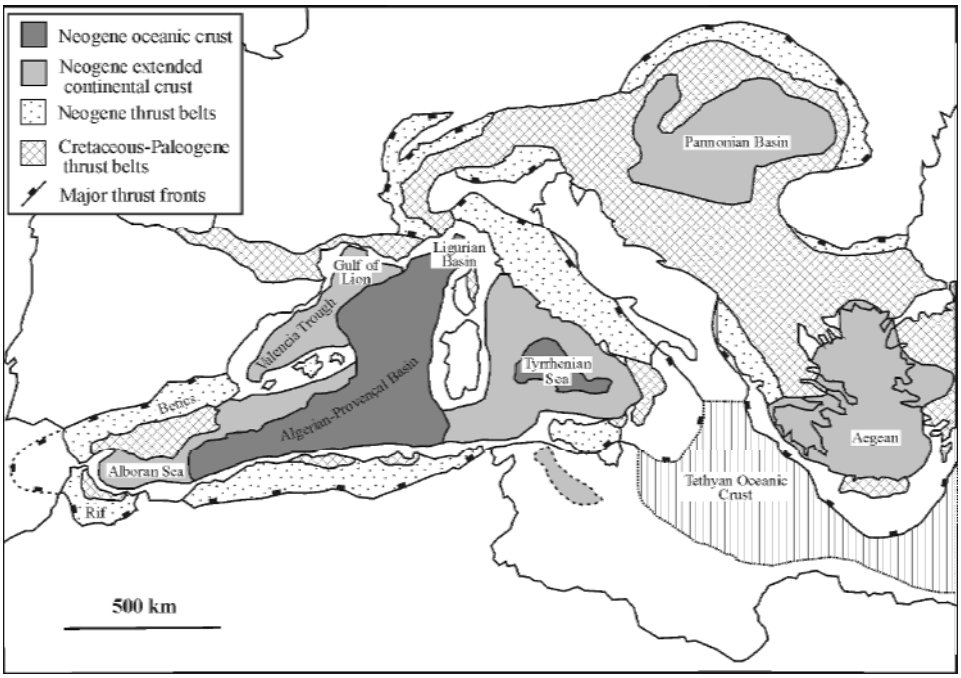

Fig. 1. Overview map of the Mediterranean Sea (after Lonergan & White 1997).

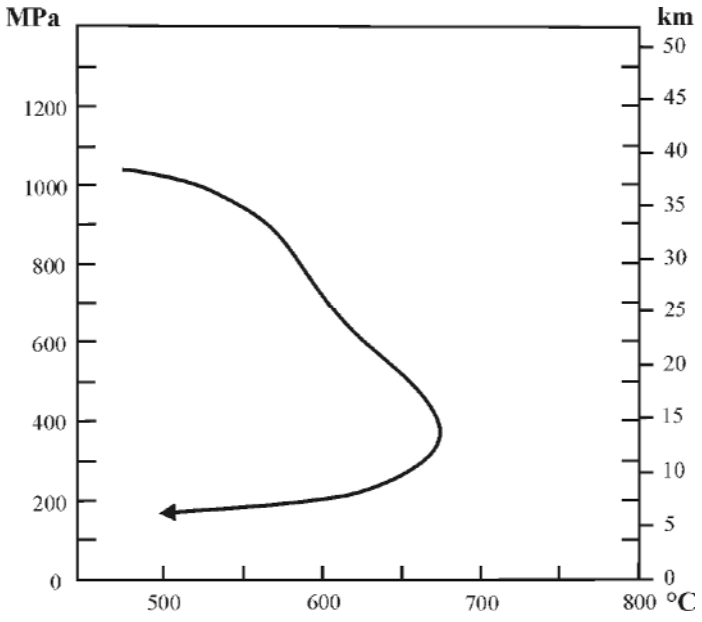

Fig. 2. P-T path of the high-grade metamorphic rocks drilled at Ocean Drilling Program Site 976 in the Alboran Sea.

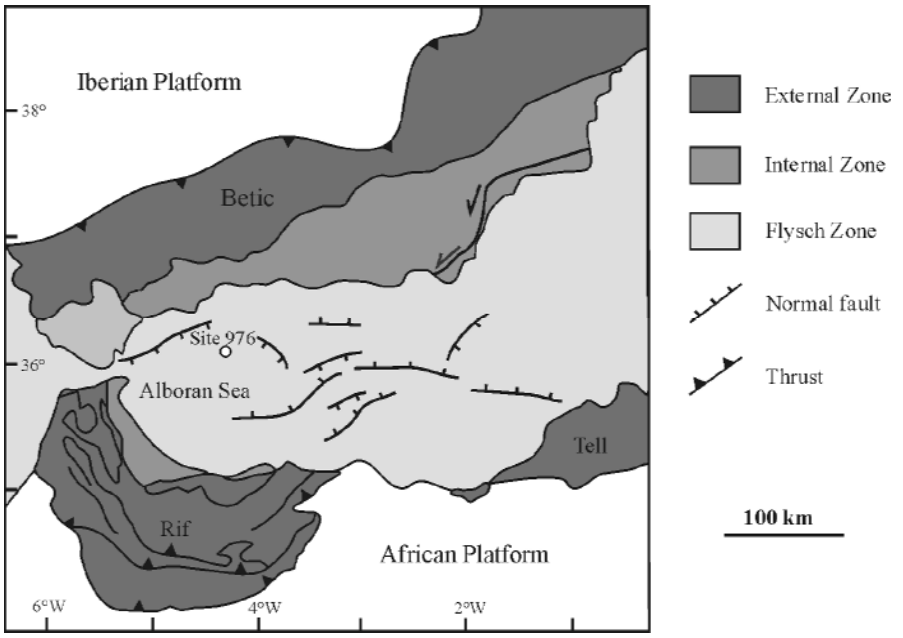

Fig. 3. Geological map of the Alboran Sea and the Betic-Rif Cordillera (after Platt & Vissers 1989) with the location of Site 976.

Regional setting

The Hellenide-Anatolide orogen in the eastern Mediterranean forms an arcuate orogen to the north of the present-day active margin which marks the site of northeastwards subduction of the African plate beneath the Apulian-Anatolian microplate. The orogen is an amalgamation of various tectonic units (Fig. 4). The Hellenides can be subdivided from top (north) to bottom (south) in: (1) the Internal zone, (2) the Vardar-İzmir-Ankara zone, (3) the Lycian nappes, (4) the Cycladic zone and (5) the External Hellenides. In the Anatolides of western Turkey the Menderes nappes as part of Anatolia form the lowermost tectonic unit, instead of the External Hellenides.

The Internal zone consists of continental fragments of the Eurasian plate, underneath which oceanic crust of the Neotethys was subducted during Cretaceous convergence (Şengör & Yilmaz 1981). The related suture is the ophiolitic Vardar-İzmir-Ankara zone (Şengör et al. 1984) which in part was metamorphosed under blueschist-facies conditions (18-22 kbar, 400°- 460°C) in the Late Cretaceous (Sherlock et al. 1999). The underlying Lycian nappes are a thin-skinned thrust belt, which are assumed to root in the Vardar-İzmir-Ankara zone (Collins & Robertson 1997) and was in part metamorphosed under incipient high-pressure conditions (Franz & Okrusch 1992). The Cycladic zone consists of continental fragments of the Adriatic plate and can be subdivided into three tectonic units. From top to bottom there are following tectonic units: (1) the non- to weakly metamorphosed ophiolitic Upper unit with

Pliocene sediments, which is overlain on the islands of Syros and Tinos by the Vari/Akrotiri unit, (2) the high-pressure rocks of the Cycladic blueschist unit which is subdivided in three separate members: (a) an ophiolitic mélange, (b) a Permo-Carboniferous to latest Cretaceous passive-margin sequence and (c) a Carboniferous basement nappe, which also occurs as slices in the passive-margin sequence. The metamorphic evolution of the Cycladic blueschist unit includes an Early Tertiary high-pressure event (15-20 kbar and 450-550°C) at ~55 Ma followed by a greenschist-facies overprint (4-7 kbar and ~400°C on most islands) at 21-16 Ma (Altherr et al. 1982; Wijbrans et al. 1990; Bröcker et al. 1993, Tomaschek et al. 2003; Ring & Layer 2003). (3) The Basal unit as part of the External Hellenides consists of Mesozoic and Early Cenozoic platform carbonates found in several tectonic windows (Avigad & Garfunkel 1989). It is a parautochthonous unit, which is metamorphosed under high-pressure conditions and underthrust below the Cycladic blueschist unit.

In contrast to parts of the External Hellenides, the Menderes nappes do not show Alpine high-pressure metamorphism (Ring et al. 2001b). Another difference is that the basement of the Menderes nappes, the Çine nappe, is of Neoproterozoic to Cambrian age (Régnier et al. 2003). The absence of Alpine high-pressure metamorphism in the Menderes nappes and the lack of a well-defined subduction zone to the south of western Turkey indicate that subduction ceased after the collision of the exotic Anatolide microcontinent in the Eocene (Gessner et al. 2001b; Ring et al. 2001b).

In the Middle to Late Miocene, the Cyclades became part of the magmatic arc of the southward retreating Hellenic subduction zone as evidenced by arc-related volcanic rocks ranging from ~5-12 Ma (Fytikas et al. 1984; Weidmann et al. 1984) and granites spanning an age range from ~10-14 Ma (Keay 1998). The granites are synkinematic to major extensional detachments (Faure et al. 1991; Lee & Lister 1992).

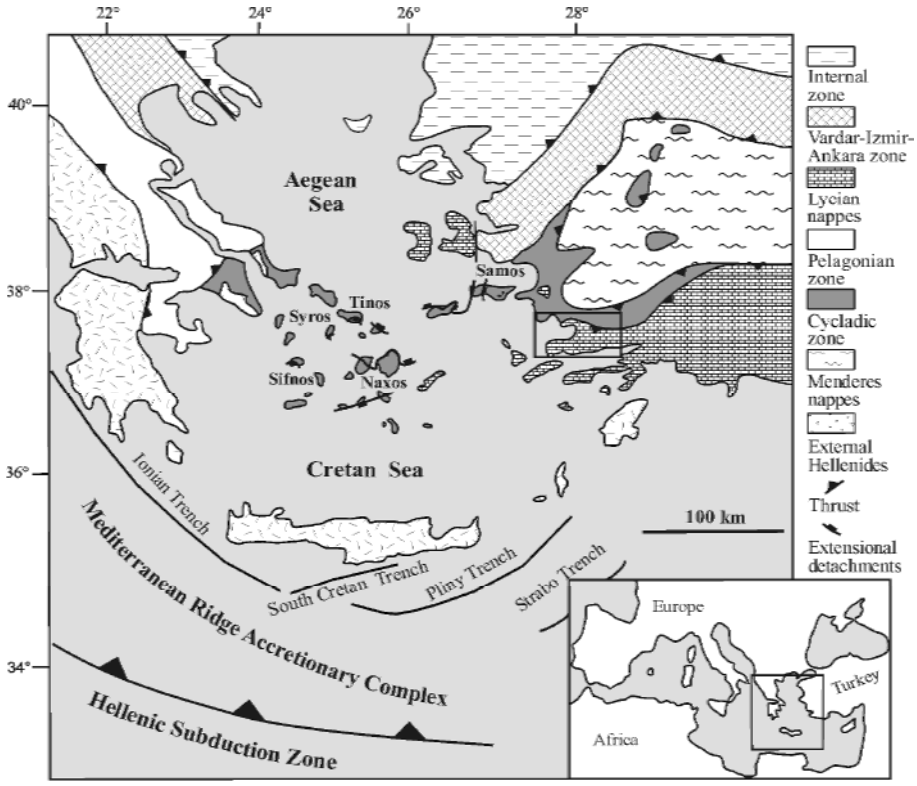

Fig. 4. Generalized map of the Aegean and adjacent mainlands showing tectonometamorphic units and Hellenic subduction zone. The rectangle represents the sampling area in western Turkey. Inset shows location of main map.

Geology of the sampling area

Our study area is the Cycladic blueschist unit exposed on several islands in the Aegean and in the western part of Turkey. We collected samples on Sifnos, Syros, Tinos, Naxos, Samos and also in western Turkey. In the following a general geological overview of the different areas is given. Also the geological setting of the Alboran Sea in the western Mediterranean is outlined because of our evaluation of the assumptions made by Platt et al. (1998).

Geology of Sifnos

The island of Sifnos is made up entirely of rocks of the Cycladic blueschist unit (Fig. 5). The stratigraphic sequence includes four lithological units (Davis 1966), which are from top to bottom: (1) the Upper marble unit, (2) the Blueschist-eclogite unit, (3) the Main marble unit and (4) the Greenschist unit. The Blueschist and Greenschist units are composed of very similar volcano-sedimentary successions and all units were subjected to Eocene high-pressure metamorphism under analogous blueschist- to eclogite-facies conditions (Schmädike & Will 2003). Typical high-pressure rocks are blueschist and eclogite in basic lithologies, jadeite-

gneiss in acidic compositions, and glaucophane-bearing micaschist, calcschist and marble in the sedimentary layers (Schmädicke & Will 2003). The high-pressure rocks are preserved in the Blueschist unit and only a few high-pressure relics are retained in the Greenschist unit (Schliestedt 1990). The greenschist-facies overprint is attributed to the middle-pressure Barrovian-type metamorphic event (Schmädicke & Will 2003).

For the finite-strain analysis two metamorphic conglomerates samples were collected from the Upper marble unit (Fig. 5).

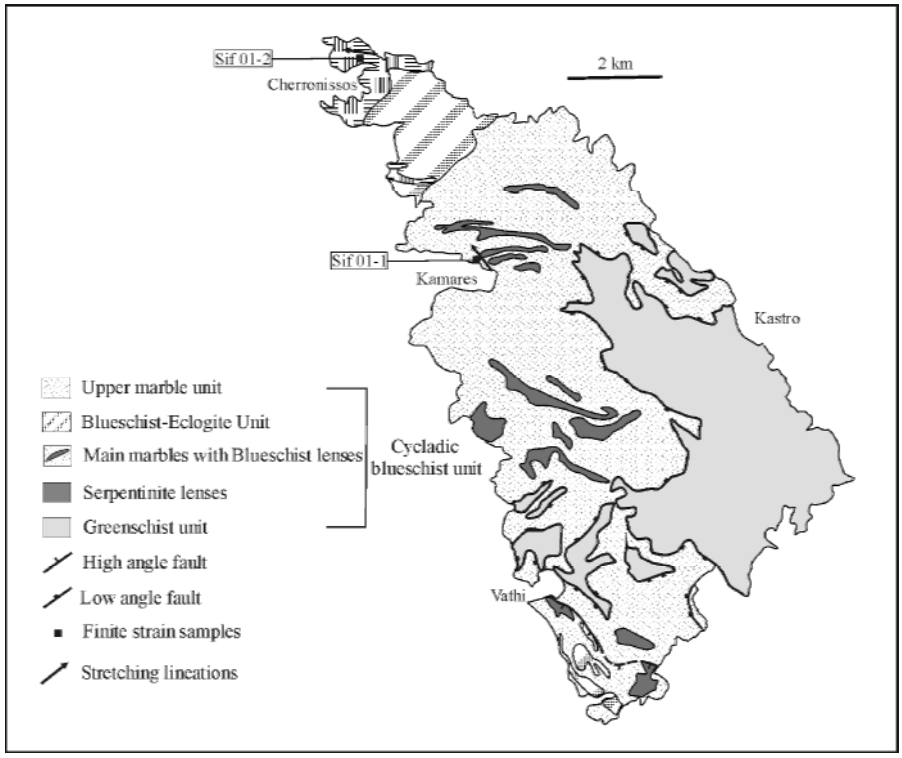

Fig. 5. Simplified geological map of Sifnos Island (after Trotet et al. 2001) with sample locations and orientation of stretching lineations.

Geology of Syros

The main tectonic units of Syros are the Vari unit, the Upper unit and the underlying Cycladic blueschist unit (Fig. 6). The Vari unit consists of chloritic schists, metabasites and acidic gneisses metamorphosed at amphibolite conditions and is only exposed in southeast Syros (Bröcker & Enders 2001). The Vari unit is separated from the underlying Upper unit and the Cycladic blueschist unit by the top-to-the-NE Vari detachment (Ring et al. 2003a). The greenschist-facies Upper unit contains phyllites. The Cycladic blueschist unit is subdivided from top to bottom into three subunits: (1) metabasalts, metagabbros, quartzites and metagraywackes metamorphosed under eclogite- and blueschist-facies conditions, and (2)

marbles with relics of eclogites and lenses of metasediments and metavolcanics metamorphosed under albite-epidote-blueschist conditions. (3) Quartzites, pelites, gneisses and basic rocks metamorphosed under greenschist-facies conditions (Trotet et al. 2001). Two metamorphic calcareous conglomerates samples from the upper subunit of the Cycladic blueschist unit were collected for the strain measurements (Fig. 6).

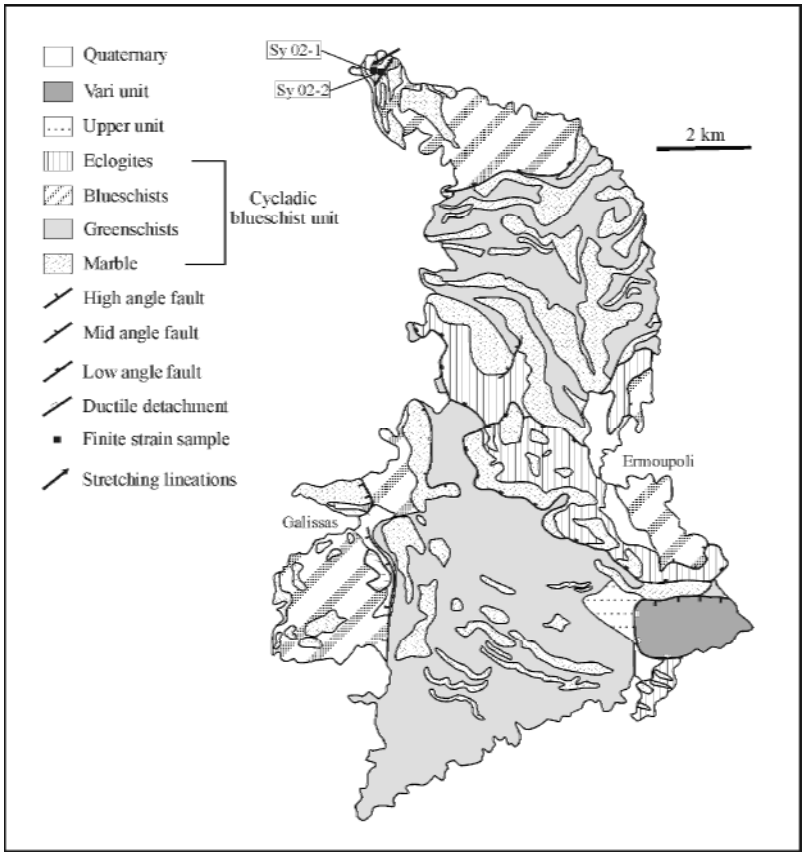

Fig. 6. Simplified geological map of Syros Island (after Trotet et al. 2001) with sample locations and orientation of stretching lineations.

Geology of Tinos

Tinos can be sudivided into four units (Bröcker & Franz 2000). From top to bottom these are (1) the Akrotiri unit, (2) the Upper unit, (3) the Cycladic blueschist unit and (4) the Basal unit (Fig. 7). The Akrotiri unit is only exposed in southern Tinos and contains amphibolites, paragneisses and minor silicate marbles (Patzak et al. 1994). This unit is separated from the underlying Upper unit by the low-angle top-to-the-NE Vari detachment (Avigad & Garfunkel 1989; Ring et al. 2003a). The Upper Unit shows greenschist-facies metamorphism and consists of serpentinites, meta-gabbros, ophicalcites and phyllitic rocks (Melidonis 1980) and is interpreted as a disrupted meta-ophiolite (Katzir et al. 1996). The Cycladic blueschist unit

consists of marbles, calcschists, siliciclastic metasediments, cherst as well as basic and acid metavolcanic rocks (Melidonis 1980). One metamorphic conglomerate sample for the finite-strain measurement has been derived from this succession (Fig. 7). The main part of the unit shows greenschist-facies mineral assemblages with P-T conditions of ~450-500°C and ~4-7 kbar. But there are also relics of the earlier high-pressure event preserved with ~450-500°C and 15 ± 3 kbar (Bröcker et al. 1993). The Basal unit is only exposed in the northeast of the island and contains various metamorphic carbonate rocks (Avigad & Garfunkel 1989). During the low to medium P-T metamorphism in the Miocene I- and S-type granites intruded into the units and caused intensive contact metamorphism (Altherr et al. 1982).

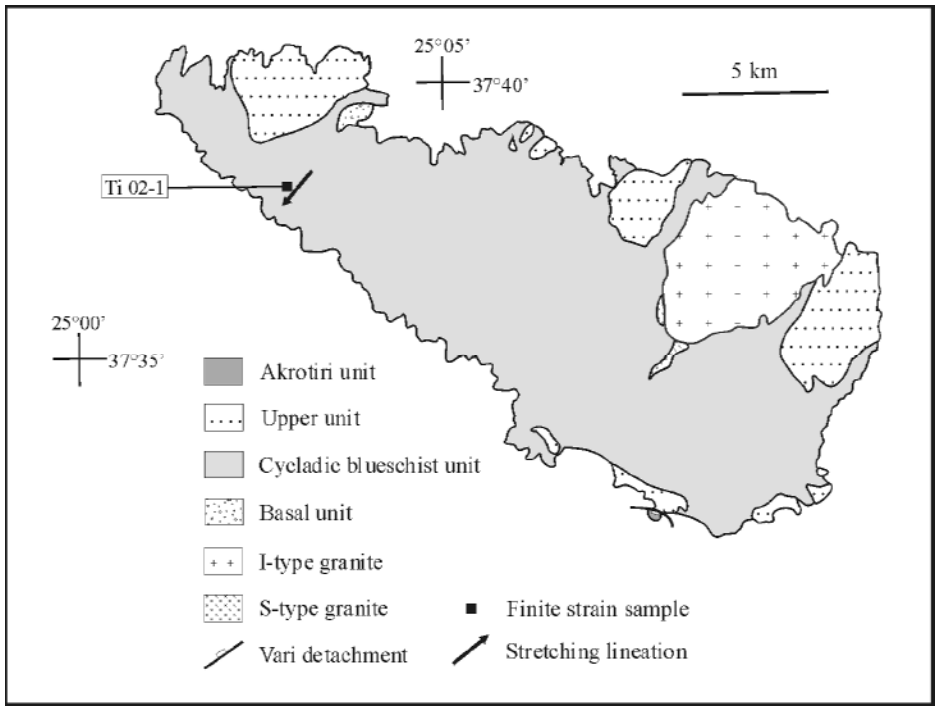

Fig. 7. Simplified geological map of Tinos Island (after Altherr et al. 1982) with sample location and orientation of stretching lineation.

Geology of Naxos

Naxos is divided into the Upper Unit and the Cycladic blueschist unit which is subdivided into a passive margin and a basement sequence unit (Fig. 8) (Jansen & Schuiling 1976). From former subunit two marble meta-conglomerate samples were collected for the finite-strain analysis (Fig. 8). The N-S oriented metamorphic dome on Naxos is the lowermost structural unit (basement sequence) and is comprised of migmatized gneissic quartzofeldspathic rocks containing marble, metapelite and amphibolite. Above is the passive-margin sequence consisting of Mesozoic metabauxite-bearing marbles, schists and metavolcanics (Dürr et al.

1978). Two types of granites intruded into the island, a S-type granite in the north and an I-type granite in the western part of Naxos. The former intruded between 15 ± 0.1 and 11.3 ± 0.2 Ma (Keay et al. 2001) and the latter at ~12 Ma (Andriessen et al. 1979). On Naxos, the-top-to-the-NNE Mountsouna extensional fault system separates the Upper unit from the I-type granite and the Cycladic blueschist unit.

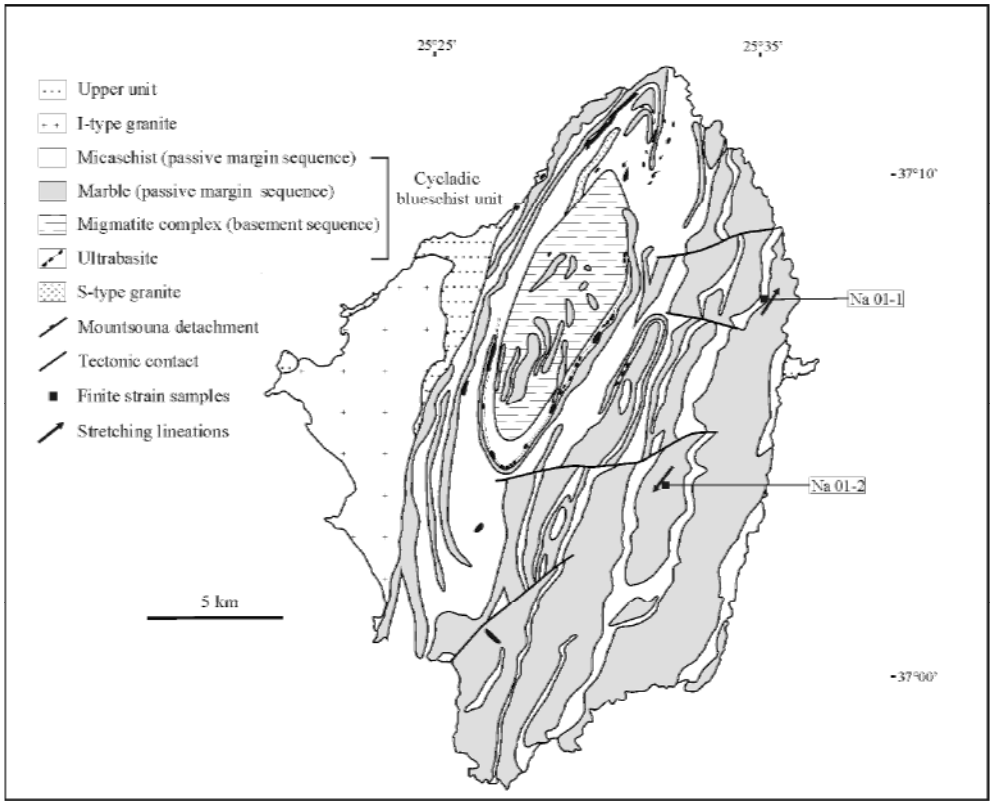

Fig. 8. Simplified geological map of Naxos Island (after Urai et al. 1990) with sample locations and orientation of stretching lineations.

Geology of Samos

On Samos Island, an E-dipping nappe pile is exposed. From top to bottom there is the non-metamorphic Kallithea nappe (Upper unit), which is underlain by the Selçuk (ophiolitic mélange), the Ampelos (Post-Carboniferous cover) and Agios Nikolaos (Carboniferous basement) nappes (Fig. 9). The last three nappes are belonging to the Cycladic blueschist unit, which again is underlain by the Kerketas nappe (Basal unit). The Selçuk nappe contains blocks of metagabbro in a matrix of serpentinite and garnet-mica schist. Ring et al. (1999b) argued that this nappe was correlative with the ophiolitic mélange on another Cycladic islands. The P-T conditions of the Selçuk nappe are ~8 ± 2 kbar and ~410°C ± 40°C to ~480°C ± 80°C (Will pers. commun. 2004). The Ampelos nappe which has been interpreted

as a former passive continental margin sequence (Altherr & Seidel 1977) consists of quarzite, metapelite and metabasite and is overlain by marble containing metabauxite (Dürr et al. 1978). The augen gneiss sample for our finite-strain study was collected from latter unit (Fig. 9). The underlying Agios Nikolaos nappe contains marble and garnet-mica schist which are intruded by Carboniferous orthogneiss. The nappe represents part of the former basement of the shelf sequence. The P-T conditions of the Agios Nikolaos nappe is ~12-19 kbar and 450-550°C (Will et al. 1998). The basal Kerketas nappe consists of marbles capped by post-middle Eocene metaflysch. This unit underwent Oligocene to Miocene high-pressure metamorphism (Ring et al. 1999b) with about 8-10 kbar and 350-400°C (Avigad et al. 1997). A subsequent Barrovian metamorphism overprinted all high-pressure units and reached greenschist-facies conditions. Middle Miocene to Pliocene sediments occur in three graben.

Three extensional fault systems occur on Samos: (1) The top-to-the-N Kallithea detachment, which separates the Kallithea nappe from the Cycladic blueschist unit and the Kerketas nappe. (2) The top-to-the-ENE Kerketas detachment between the Kerketas nappe and the overlying Ampelos nappe. The Kerketas detachment is associated with the development of Middle Miocene graben (Weidmann et al. 1984; Ring et al. 1999b). (3) The top-to-the-ENE Selçuk extensional system between the Ampelos nappe and the Selçuk nappe.

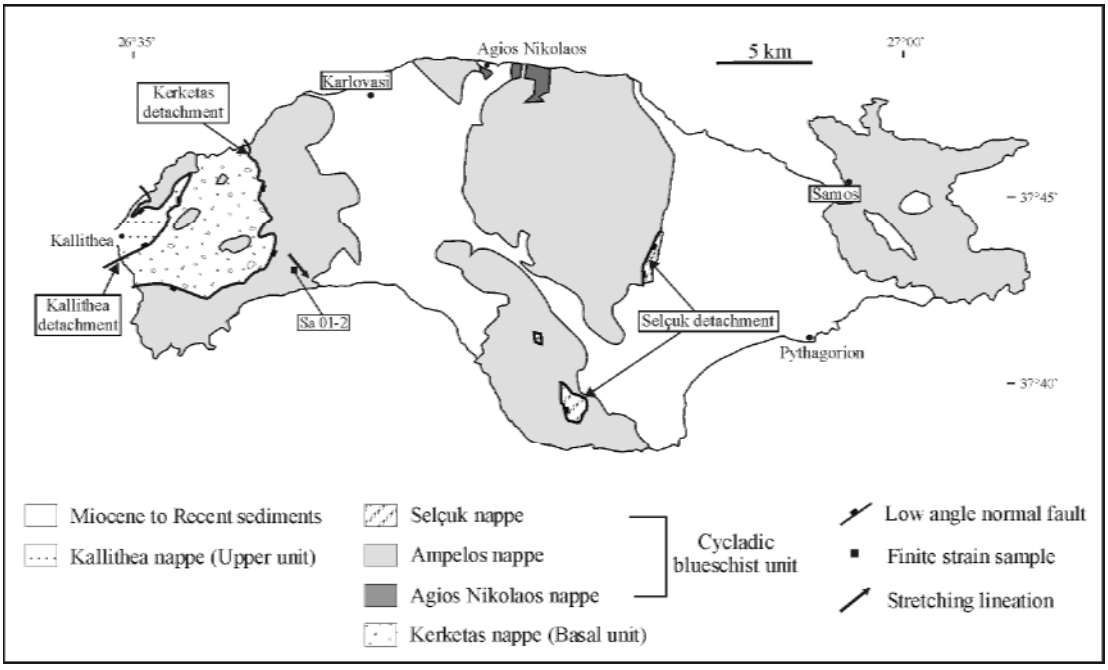

Fig. 9. Simplified geological map of Samos Island with sample location and orientation of stretching lineation (modified after Ring et al. 1999b).

Geology of western Turkey

In western Turkey the Cycladic blueschist unit is made up by the Selçuk mélange and the underlying Dilek nappe (Fig. 10) (Ring et al. 1999c). The Selçuk mélange correlates with the Selçuk nappe in Samos and the ophiolitic mélange of the Cycladic islands. The mélange consists of blocks of metagabbro, which are surrounded by a matrix of serpentinite and garnet-mica schist. The underlying Dilek nappe is a metamorphosed Permo-Mesozoic shelf sequence which includes a quarzite conglomerate with interlayered kyanite-chloritoid schist, metabasite, phyllite and marble containing metabauxite. This nappe is correlative with the Ampelos nappe on Samos (Ring et al. 1999c). The Dilek nappe shows 10 kbar and <470°C for high-pressure metamorphism (Candan et al. 1997) which is largely similar with the conditions of the Ampelos nappe on Samos (~15 kbar and 500°C, Will et al. 1998). The passive-margin sequence can also be correlated with the Post-Carboniferous cover of the Cycladic islands. The Dilek nappe is overlain by lower to middle Palaeocene flysch (Özer et al. 2001), but no Carboniferous basement is exposed below the nappe (Ring et al. 1999c). Seven conglomerate samples for the strain measurements were collected from the lower Dilek nappe (Fig. 10).

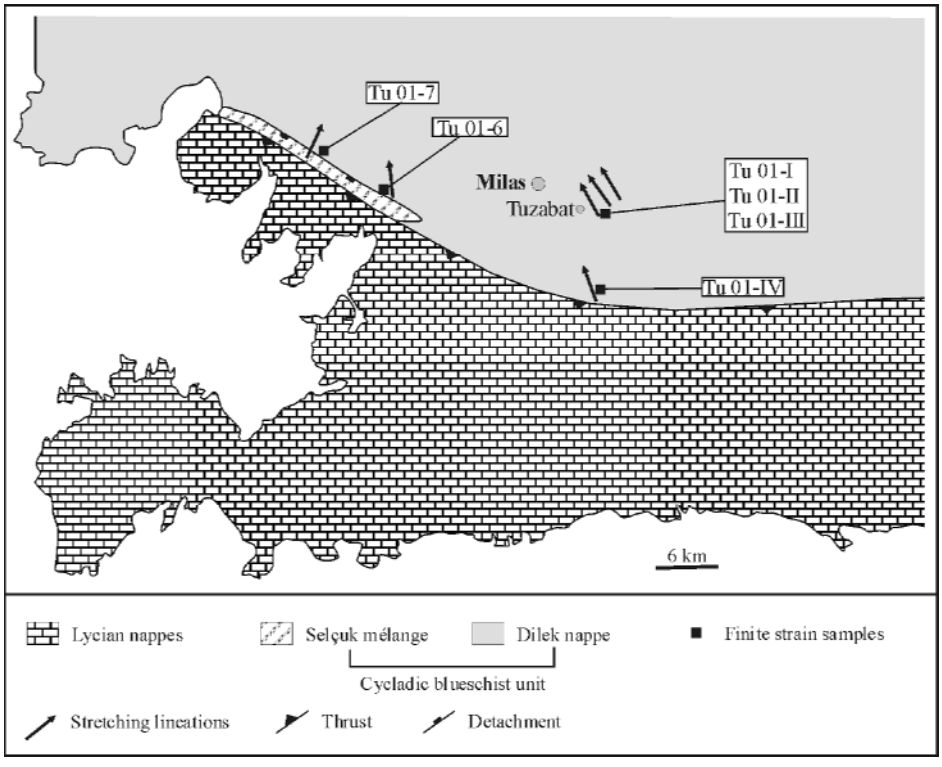

Fig. 10. Simplified geological map showing the western part of Turkey with sample locations and orientation of stretching lineations.

Setting of the Alboran Sea

The Alboran Sea is surrounded by the mountains of the Rif-Betic Cordillera in southern Spain and the Rif and Tell mountains in northern Morocco, which together form an arc shape orogenic belt in the westernmost end of the Mediterranean (Fig. 3). The rocks of the Rif-Betic Cordillera are divided into three main zones: (1) the Internal Zone, (2) the External Zone and (3) the Flysch Zone. The allochthonous Paleozoic to Early Miocene rocks of the Internal Zone were thrust onto the External Zone during the Miocene (Crespo-Blanc & Campos 2001). During the Cretaceous and the Tertiary the Internal Zone was affected by the Alpine deformation and metamorphism. Crustal rocks were buried to great depths and underwent high-pressure metamorphism (de Jong 1990). The External Zone comprises of Mesozoic to Tertiary rocks, which represent the passive margin of Africa and Iberia and were deformed during Alpine orogeny. The Flysch Zone consists of Early Cretaceous to Early Miocene deep marin clastic deposits (Wildi 1983).

During the Late Oligocene to Early Miocene extensional deformation took place and was associated with rapid exhumation of the high-pressure rocks. $^{40}Ar/^{39}Ar$ ages of muscovite and apatite fission track analyses indicate that the final exhumation and cooling of the high-pressure metamorphic rocks occurred very fast between 20.5 Ma and 18 Ma (Platt et al. 1998). The first magmatic intrusions occurred at 23-22 Ma in the central and internal zones of the Betics and continued until the late Miocene (Lonergan & White 1997; Platt et al. 1998).

The basin of the Alboran Sea is underlain by 13-20 km thick continental crust (Platt et al. 1989) and comprise similar rocks as in the Rif-Betic Cordillera, which are covered by Early Miocene syn-rift deposits and post-rift marine sediments (Platt et al. 1998). This means the region was subjected to extension during the Middle Miocene that led to the formation of the Alboran Sea. During the extension in the Alboran Sea thrusting and folding took place in the External Zones of the Rif-Betic Cordillera (Platt & Vissers 1989).

Model of Platt et al. (1998)

Platt et al. (1998) carried out thermal modeling of the P-T path obtained from the high-grade metamorphic rocks drilled at Ocean Drilling Program Site 976 in the Alboran Sea in the western Mediterranean (Fig. 3). The P-T path (Fig. 2) shows decompression from ~40 km depth (1050 MPa) to ~13 km (350 MPa), which is increasing from ~550° ± 50°C to 675° ± 25°C (Platt et al. 1998). Platt et al. (1998) considered for the modeling several variables: the thickness and thermal gradient of the postorogenic lithosphere, the radiogenic heat production in the thickened crust, the pause between the end of contractional tectonics and the start of

extension, the removal of lithospheric mantle at different depths within the lithosphere and the rate of extension. The only combination of variables which shows the observed characteristics of the P-T path (Fig. 2) involves postcollisional high radiogenic heat production combined with a significant postcontractional pause, the removal of lithosphere at a depth of 60-70 km, extension by a factor of 3 in 6 Ma and final fast exhumation and cooling between 20.5 to 18 Ma. The modeling results predict a huge vertical ductile thinning of the whole lithosphere in the Alboran Sea. Platt et al. (1998) assume that vertical thinning constitutes the primary process for the exhumation of the high-grade metamorphic rocks.

Potential problems of vertical ductile thinning

In the simplest case, where ductile deformation is entirely exhuming high-pressure rocks, vertical ductile thinning is given by the average vertical stretch S_{vert} because it represents how much the vertical has changed in thickness. For complete exhumation of deep-seated rocks S_{vert} must be zero. Ductile thinning by itself cannot fully exhume rocks and therefore additional shallow exhumation processes, such as normal faulting or erosion, are required to bring the rocks back to the Earth's surface (Fig. 11a) (Platt et al. 1998; Feehan & Brandon 1999; Ring et al. 1999). If shallow exhumation processes are active, the overburden thins at a faster rate than it would occur only by ductile thinning. Therefore, the contribution of ductile thinning to the overall exhumation is more difficult to quantify. Feehan & Brandon (1999) introduced a one-dimensional numerical model, which tracks the vertical rate at which a rock moved through its overburden. The rate of thinning of the remaining overburden at each step of the exhumation path must be considered. The increment of vertical strain is then distributed over a thinner section of overburden and so the increment of ductile thinning is smaller than in the case where ductile thinning is entirely exhuming the rocks. The deformation rate along the exhumation path is represented by the velocity-gradient tensor, L(z), which is a function of depth. Using a depth-proportional strain-rate law, L(z) is increasing linearly with depth (Feehan & Brandon 1999) (Fig. 11b). Vertical ductile thinning for a proportional strain-rate law is decreasing exponentially towards the Earth's surface, if L(z) is integrated along a vertical flow path with a steady-state wedge. The exponentially decrease of ductile thinning results from the coeval decrease of the overburden. The material is moving through the wedge along the exhumation path from a more rapidly deforming part at the base towards the top, whereas the rate of exhumation is changing (Fig. 11b).

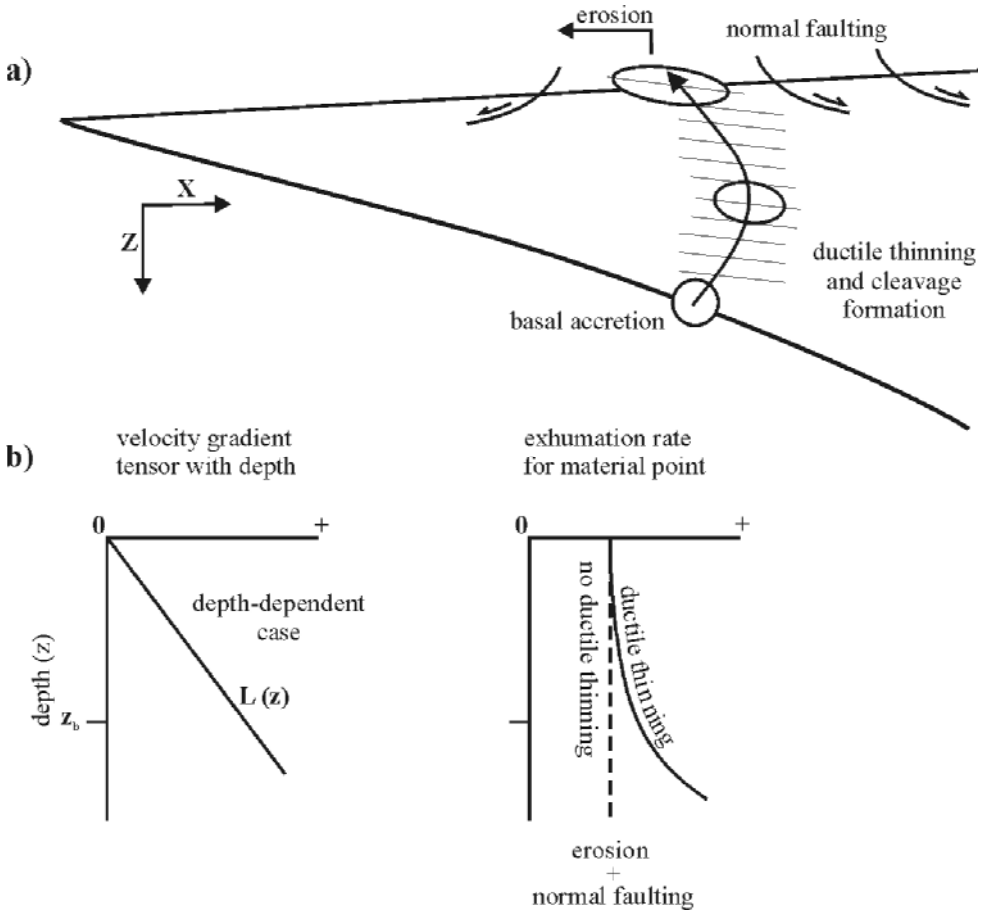

Fig. 11. (a) Schematic cross section of a steady-state accretionary wedge showing the major processes responsible for vertical thinning or thickening of the wedge and how they affect a particle moving through the wedge along an idealized exhumation path (Feehan & Brandon 1999). (b) Left: diagram shows that the velocity-gradient tensor L(z), which is a function of depth, is increasing proportionally with depth. Right: diagram shows that vertical ductile thinning for a proportional strain-rate law is decreasing exponentially towards the Earth's surface, if L(z) is integrated over the exhumation path.

Strain analysis

Basic concept of strain

To describe finite strain in a rock six independent variables are required. Three variables describe the orientation of the principal stretching directions *X*, *Y* and *Z*, where *X* represents the maximum stretching direction, *Y* the intermediate stretching direction, and *Z* the maximum shortening direction. The remaining three variables describe the magnitude of the principal strain along these directions which are represented by the absolute principal stretches S_X, S_Y and S_Z ($S_X \geq S_Y \geq S_Z$). $S = l_f/l_i$, where l_i and l_f are the initial and final lengths of a material line. Also the principal axial ratios R_{XY}, R_{XZ} and R_{YZ} are used to describe strain, where $R_{XY} = S_X/S_Y$, $R_{XZ} = S_X/S_Z$ and $R_{YZ} = S_Y/S_Z$. The volume strain S_V is normally also an important variable which is defined as $S_V = V_f/V_i$, where V_f is the final and V_i the initial volume of an elementary volume. For our calculation we assume constant volume, so $S_V = 1$.

For the strain analysis the axially ratios R_{XY}, R_{XZ} were first determined. Then R_{YZ} was calculated as follows:

$$R_{yz} = \frac{R_{xz}}{R_{xy}}.$$

S_X, S_Y and S_Z, are calculated with the following formulae:

$$S_y = \sqrt[3]{\frac{R_{xz}}{R_{xy}^2}},$$

$$S_x = R_{xy} \times S_y,$$

$$S_z = \frac{1}{S_x \times S_y}.$$

Method of strain measurement

R_f/ϕ-method

To test the assumption of Platt et al. (1998), that ductile thinning contributed significantly to the exhumation of high-pressure rocks, we quantified finite strain with the R_f/ϕ-method (Ramsay 1967; Ramsay & Huber 1983) in the Cycladic blueschist unit on several Aegean islands and also from western Turkey. We collected 13 samples from metamorphic conglomerates on the islands of Sifnos, Syros, Tinos, Naxos and from western Turkey. On Samos Island one augen gneiss sample was sampled (Table 1). The R_f/ϕ-method uses deformed objects which were initially elliptical and assumes homogeneous deformation between the objects and their matrix. If the undeformed objects were approximately ellipsoidal, it is possible to separate the initial ellipticity from that imposed by the strain and thereby to estimate the strain. In this manner the finite strain of the object can be determined (Twiss & Moores 1992). The final ellipticity R_f and the orientation of the longest axis ϕ of a deformed object depend on the initial ellipticity R_i and on the initial orientation θ of the undeformed object.

The *rphin* program was used to digitize and to process the data for the R_f/ϕ-method. The axial ratio (R_f) and the angle ϕ between the long axis of the grain and a reference line were determined in two perpendicular planes (*XY*, *XZ*). The third plane *YZ* was calculated ($X \geq Y \geq Z$). The corresponding finite two-dimensional strain ellipses were computed with the program *theta*. The reference lines were chosen parallel to one of the principal directions. For the R_f/ϕ analysis on the pebbles of the metamorphic conglomerates, the long and short axes of up to 30 pebbles per section were measured and mean aspect ratios for each section were calculated. We collected five samples and measured them in the laboratory. On seven localities this proved impossible and so the measurements were made on natural joint surfaces in the field or photos for the analysis were taken (for two samples), which were then blown up to DinA4 images of the different sections. Strain markers were traced on transparent overlays on the images, and the traces were then digitized. Tectonic strains were determined from the chi-squared minima of the R_f/ϕ analysis (Peach & Lisle 1979). The strain estimates from the mutually perpendicular planes were used to calculate the finite-strain ellipsoid according to the modified least-square technique of Owens (1984).

Table 1. *Strain measurements*

Sample number	Latitude Longitude	trend	plunge	S_X	trend	plunge	S_Y	trend	plunge	S_Z	R_{XY}	R_{YZ}	R_{XZ}
Sa 01-2	N 37°43'23" E 26°40'45"	140	10	1.27	50	0	0.79	318	80	0.59	1.61	1.34	2.14
Na 01-1	N 37°07'07" E 25°33'52"	34	9	1.27	304	1	0.82	215	81	0.96	1.55	0.85	1.31
Na 01-2	N 37°02'50" E 25°32'14"	218	5	1.60	308	2	0.85	38	85	0.74	1.88	1.15	0.85
Sif 01-1	N 36°59'48" E 24°40'19"	321	25	1.32	50	2	0.86	141	83	0.54	1.55	1.59	2.47
Sif 01-2	N 37°02'22" E 24°38'33"	278	12	1.38	7	1	0.79	98	86	0.92	1.75	0.86	1.51
Sy 02-1	N 37°30'49" E 24°52'46"	240	7	1.8	330	2	0.91	60	82	0.61	1.98	1.48	2.94
Sy 02-2	N 37°30'42" E 24°53'03"	34	6	1.69	303	1	0.82	224	65	0.72	2.07	1.13	2.34
Ti 01-1	N 37°38'26" E 25°00'44"	220	8	2.76	310	2	1.07	40	78	0.34	2.59	3.13	8.12
Tü 01-6	N 37°18'12" E 27°38'26"	354	2	1.48	265	18	0.81	84	72	0.84	1.83	0.97	1.77
Tü 01-7	N 37°18'40" E 27°36'20"	15	0	1.48	115	0	0.71	270	90	0.95	2.08	0.75	1.56
Tü 01-I	N 37°18'09" E 27°54'03"	329	1	1.45	239	48	0.88	60	42	0.78	1.65	1.13	1.86
Tü 01-II	N 37°18'09" E 27°54'03"	324	4	1.51	235	37	0.75	55	53	0.89	1.34	0.84	1.70
Tü 01-III	N 37°18'09" E 27°54'03"	331	2	1.46	241	42	1.04	61	48	0.55	1.39	1.90	2.65
Tü 01-IV	N 37°14'35" E 27°48'30"	340	4	2.04	250	22	0.79	70	68	0.62	2.57	1.28	3.28
tensor average		**350**	**2**	**1.24**	**259**	**11**	**1.06**	**91**	**79**	**0.70**	-	-	-

Sa 01 2, Na 01-1, Na 01-2, Sif 01-2 and Tü 01-6: laboratory analyses; Tü 01-I, Tü 01-III, Tü 01-IV, Sy 02-1, Sy 02-2, Sif 01-1 and Ti 02-1: field analyses; Tü 01-7 and Tü 01-II: photo analyses.

Results of strain measurement

Principal strain directions

The principal strain directions are plotted in lower-hemisphere stereograms (Table 1, Fig. 12). Before plotting the axes in stereograms, the principal axes of the samples from western Turkey were rotated by 90° around a vertical axis. The rotation is based on the field study by Régnier et al. (2003) in western Turkey who showed that the Cycladic blueschist unit passively rotated after ductile strain accumulated. They show that the stretching lineations in the study area swing from an original SSW trend into an ESE-WNW trend near the Eocene Cyclades-Menderes thrust. To undo this subsequent rotation, the collected samples from the Cycladic blueschist unit in western Turkey were rotated until the *X*, *Y* and *Z* axes acquired their original positions with the stretching lineation trending NNE-SSW. The intermediate axis, *Y*, and the maximum shortening direction, *Z*, are reconstructed following the right-hand-rule.

An important observation is that the individual principal strain directions are variable in orientation, showing a scattering in the stereograms (Fig. 12). The observed variability is too large to be attributed to measurement error alone. Thus, averages for these data were calculated with the *meandefm* program of Brandon (1995). The *X*-axes of the samples show a general N-S trend with plunges between 0 and 25°. The calculated tensor average is trending NNW (350/02). The orientations of the intermediate axes are subhorizontal with a tensor average showing a WSW trend (259/11). The *X* and *Y* axes demonstrate almost great-circle distribution with weakly defined maxima. The maximum shortening direction *Z* of the samples show steeply plunges. The calculated average is 91/79. The foliation of the samples is subhorizontal indicating ductile thinning.

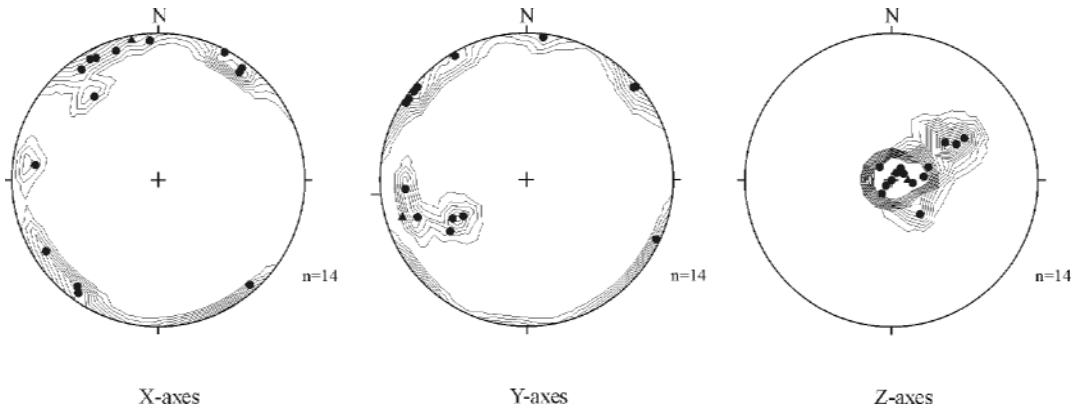

Fig. 12. Lower-hemisphere equal-area stereograms for the principal stretch directions *X*, *Y* and *Z*. The triangles are representing the tensor averages of the respective axes.

Finite-strain data from the high-pressure rocks of the Cycladic blueschist unit

The relative finite-strain data are summarized in Table 1 and plotted in a Flinn diagram (Flinn 1962) in Figure 13. The plot is useful for distinguishing the relative shapes of the strain ellipsoids, whether prolate or oblate. Following Hossack (1968), this classification is called *strain symmetry*.

The Flinn plot (Fig. 13) indicates that the strain ellipsoids generally have a prolate symmetry with two data points in the oblate field close to the plane-strain line. The axial ratio R_{XZ} ranges from 0.85 to 8.12 with S_X ranging from 1.27 to 2.76 (Table 1). The stretches in the Z direction, S_Z, range from 0.34 to 0.96, indicating vertical shortening of 66% to 4%, and S_Y ranges from 0.71 to 1.07. For addressing aspects of the regional deformation, averages of the strain tensor were calculated from single measurements. The principal strain axes of each sample show a high variability in their orientations. This variability can be attributed to the

local variations of the deformation or the error in measurements. The average extension parallel to the *X*-direction of the tensor average is 24% (S_X = 1.24). The *Y*-axis shows a extension of 6% (S_Y = 1.06) and the *Z*-axis a shortening of 30% (S_Z = 0.70). The tensor averages always lie on the low side of the distribution of the single measurements unless the individual strain tensors all have the same orientation (Brandon 1995). In our case, the tensor average shows approximately plane strain instead of the general trend of the single measurements. S_X and S_Y are near one because at the local scale, the *X* and *Y* directions vary considerably in orientation, which means that their stretch contributions are averaged out at the regional scale.

The calculation was done with the *meandefm* program of Brandon (1995), which is based on the Hencky-tensor method. Strain and rotation tensor measurements are averaged using the constant velocity-gradient method. For details about the methods see the Appendix A of Brandon (1995).

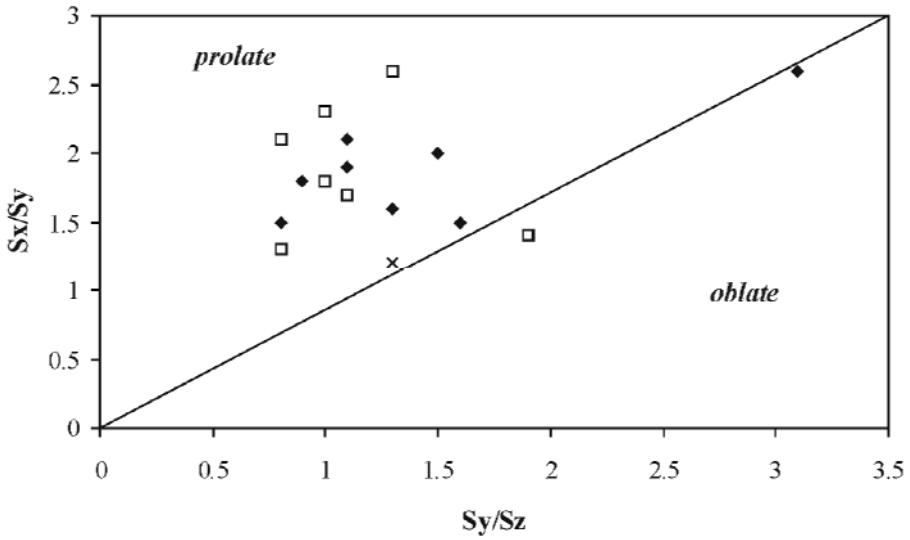

Fig. 13. Flinn diagram (Flinn 1962) showing strain symmetries obtained by the R_f/ϕ analysis. The white squares are representing the samples from the Aegean island and the black rhombuses the samples from western Turkey. The cross is demonstrating the tensor average of all samples.

Vertical ductile thinning in steady-state wedges

To estimate the contribution that vertical ductile thinning made to the total exhumation of the high-grade metamorphic rocks, we used the one-dimensional model of Feehan & Brandon (1999). The model tracks the vertical rate at which a rock moved through its overburden, and also the rate of thinning of the remaining overburden at each step along the exhumation path

(Fig. 11). To model vertical ductile thinning, we need to know the directions and magnitudes of the principles stretches, the depth from which the rocks where exhumed, the residence time of the exhuming rocks in the ductile crust and the azimuth of the transport direction during the accumulation of ductile strain. The principal stretches represent means of the data shown in Table 1 and are S_X:S_Y:S_Z = 1.24:1.06:0.70. The P-T data show that the exhumation depth is ~60 km (Will et al. 1998). The residence time for the rocks inside the ductile crust is ~40 Ma, which results from the fact that the high-pressure event occurred at ~55 Ma and the cooling below ~280°C as recorded by zircon fission track ages of ~15 Ma (Ring & Layer 2003).

Plotting the different stretches against the exhumation depth and the residence time at each step along the exhumation path (Fig. 14) show that the value for S_Z is decreasing with time towards the Earth's surface, i.e. vertical shortening is increasing. The values for S_X and S_Y are increasing with time towards the surface, but for S_Y the amount of increasing extension is smaller than for S_X.

The calculation indicates that ductile thinning contributed about 10% to the total exhumation. We conclude that ductile thinning accounts for only about 6 km of the exhumation. The remaining 54 km must have been accommodated by other processes such as normal faulting or erosion. We have no control on erosion. Topography above a retreating subduction zone is generally considered to be subdued (Royden 1993) and therefore erosion rates were probably small. Assumed erosion rates of 0.2-0.4 km Myr^{-1} yield a total erosion of 8-16 km. It follows that ~40 km of exhumation must have been due to normal faulting. These findings also show that homogeneous stretching was not the primary agent achieving large-magnitude extension in the Aegean.

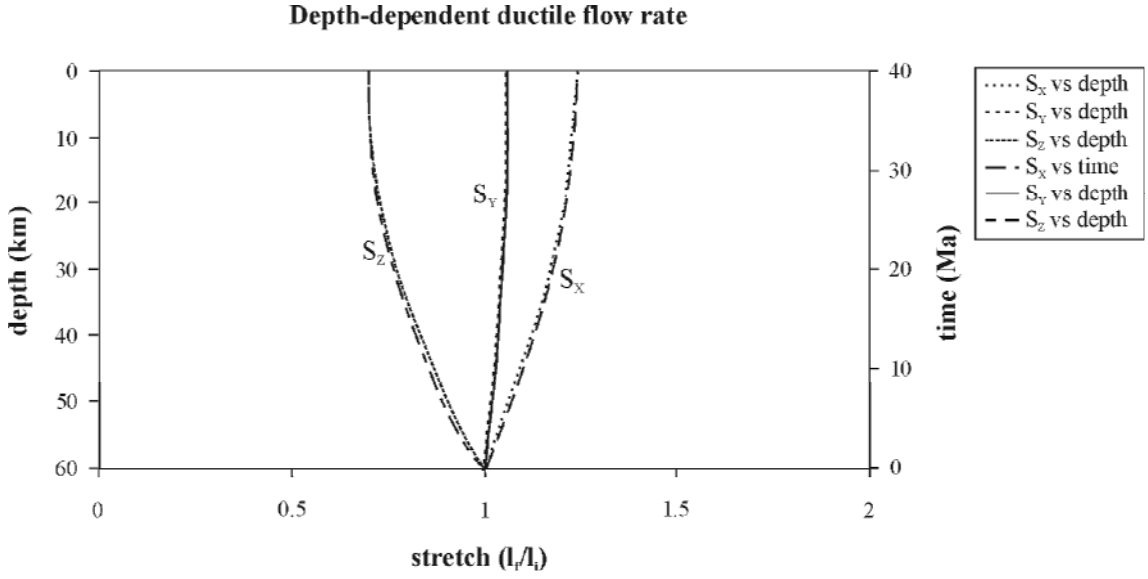

Fig. 14. The exhumation model as applied to the Cycladic blueschist unit.

Calculated finite-strain data for high-pressure rocks of the Alboran basin

We have applied the one-dimensional numerical model of Feehan and Brandon (1999) to the data which Platt et al. (1998) used to model the P-T path from the Alboran Sea. Platt et al. (1998) assumed that a vertical stretch S_{vert} of 67.5% accumulated in 6 Ma with a rate of 4.5 km Myr^{-1}. Using the Feehan and Brandon model (1999) we can backcalculate finite vertical shortening in the high-grade rocks from the Alboran Sea. Assuming plane-strain constant-volume deformation we estimate that the high-grade rocks must have a S_Z of 0.03 to account for a total of 97% of vertical ductile thinning of their overburden. It follows that the calculated value for the maximum stretch S_X must be at least 30, i.e. the aspect ratios in the *XZ* section have to be of the order of 1000. We regard such values unrealistic. Therefore, the assumptions made by Platt et al. (1998) in their modeling approach are also considered unrealistic.

Discussion

Our one-dimensional numerical calculation shows that the contribution of ductile thinning to exhumation is less than the value indicated by the estimated finite vertical shortening in the rocks. It follows that significant vertical shortening and a huge value for the maximum stretch are needed for the ductile thinning to make the significant contribution to the exhumation of the high-pressure rocks. For the case considered by Platt et al. (1998), we estimate that vertical shortening of 97% is needed in the exhumed high-pressure rocks in the Alboran Sea. This value is considered unrealistic. After Ring et al. (1999) ductile thinning by itself cannot completely exhume the rocks to the surface and therefore additional exhumation processes are required for the whole exhumation.

Our results for the strain measurements and the calculation of exhumation of the high-pressure rocks in the Aegean and western Turkey indicate that ductile thinning contributed only a small amount of ~10% to the overall exhumation. Vertical shortening in the exhumed high-pressure rocks is ~30%. Erosion is not a dominant process for the exhumation of the high-pressure rocks. Royden (1993) showed that topography above a retreating subduction zone is generally considered to be subdued and therefore erosion rates are probably small. Thus, normal faulting must be the primary agent exhuming the high-grade rocks to the Earth's surface.

The Aegean is well-known for its brittle low-angle detachment faults (Lister et al. 1984; Ring et al. 2001a), which placed unmetamorphosed or low-grade metamorphic rocks on high-grade rocks. On some Aegean islands, e.g. on the islands of Naxos (Buick 1991) and Ios

(Vandenberg & Lister 1996), brittle detachments are underlain by extensional ductile shear zones. Some authors have been suggested that Late Miocene extensional detachments accomplished the complete exhumation of the Cycladic blueschist unit in the Aegean (Lister et al. 1984). The subhorizontal foliation in the Cycladic blueschist unit shows that extensional faulting was accompanied by vertical shortening. Earlier studies indicated that vertical ductile thinning contributed to the total exhumation of metamorphic rocks caused by extensional fault systems. A matter of debate in these extensional fault systems is how much of exhumation was achieved by ductile flow relative to faulting-related exhumation.

Conclusions

Our calculations show that vertical ductile thinning constitutes only a small rate to the total exhumation of high-grade metamorphic rocks in the Mediterranean. The assumption made by Platt et al. (1998), that ductile thinning displays an important rate for exhuming deep-seated rocks to the surface is considered unrealistic. We conclude that normal faulting is the primary process that is exhuming the high-pressure rocks to the Earth's surface.

References

ALTHERR, R., KREUZER, H., WENDT, I., LENZ, H., WAGNER, G.A., KELLER, J., HARRE, W. & HÖHNDORF, A. 1982. A late Oligocene/early Miocene high temperature belt in the Attic-Cycladic crystalline complex (SE Pelagonian, Greece). *Geologisches Jahrbuch*, **E23**, 97-164.

ALTHERR, R. & SEIDEL, E. 1977. Speculations on the geodynamic evolution of the Attic-Cycladic crystalline complex during alpidic times. *In*: Kallergis, G. (ed.) Geology of the Aegean region, Proceedings VI Colloquium, Athens. Institute of Geology and Mineral Exploration, 347-351.

ANDRIESSEN, P.A.M., BOELRIJK, N.A.I.M., HEBEDA, E.H., PRIEM, H.N.A., VERDURMEN, E.A.T. & VERSCHURE, R.H. 1979. Dating the events of metamorphism and granitic magmatism in the Alpine orogen of Naxos (Cyclades, Greece). *Contributions to Mineralogy and Petrology*, **69**, 215-225.

AVIGAD, D., GARFUNKEL, Z., JOLIVET, L. & AZAÑÓN, J.M. 1997. Back-arc extension and denudation of Mediterranean eclogites. *Tectonics*, **16**, 924-941.

AVIGAD, D. & GARFUNKEL, T. 1989. Low-angle faults above and below a blueschist belt-Tinos Island, Cyclades, Greece. *Terra Nova*, **1**, 182-187.

BRANDON, M.T. 1995. Analysis of geologic strain data in strain-magnitude space. *Journal of Structural Geology*, **17** (10), 1375-1385.

BRÖCKER, M., KREUZER, H., MATTHEWS, A. & OKRUSCH, M. 1993. $^{40}Ar/^{39}Ar$ and oxygen isotope studies of polymetamorphism from Tinos Island, Cycladic blueschist belt, Greece. *Journal of Metamorphic Geology*, **11**, 223-240.

BRÖCKER, M. & ENDERS, M. 2001. Unusual bulk-rock compositions in eclogite-facies rocks from Syros and Tinos (Cyclades, Greece): implications for U-Pb zircon geochronology. *Chemical Geology*, **175**, 581-603.

BRÖCKER, M. & FRANZ, L. 2000. Contact metamorphism on Tinos (Cyclades, Greece). Part II: aureole characteristics, mineral chemistry and Rb-Sr chronology. *Mineral. Petrology* in press.

BUICK, I.S. 1991. Mylonite fabric development on Naxos, Greece. *Journal of Structural Geology*, **13** (6), 643-655.

CANDAN, O. 1997. Blueschist relics in the Mesozoic cover series of the Menderes Massif and correlations with Samos Island, Cyclades. *Schweizerische Mineralogische und Petrographische Mitteilungen*, **77**, 95-99.

COLLINS, A.S. & ROBERTSON, A.H.F. 1997. The Lycian Melange, southwest Turkey; an emplaced accretionary complex. *Geology*, **25**, 255-258.

CRESPO-BLANC, A. & CAMPOS, J. 2001. Structures and kinematics of the South Iberian paleomargin and its relationships with the Flysch Trough units: extensional tectonics within the Gibraltar Arc fold-and-thrust belt (western Betics). *Journal of Structural Geology*, **23**, 1615-1630.

DAVIS, E. 1966. Der geologische Bau der Insel Siphnos. *Geol. Geophys. Res. Athens*, **10**, 161-220.

DE JONG, K. 1990. Alpine tectonics and rotation pole evolution of Iberia. *Tectonophysics*, **184**, 279-296.

DÜRR, S., ALTHERR, R., KELLER, J., OKRUSCH, M. & SEIDEL, E. 1978. The Median Aegean Crystalline Belt: Stratigraphy, structure, metamorphism, magmatism. *In*: Alps, Apennines, Hellenides, Cloos, H., Roeder, D. & Schmidt, K., E. Schweizerbart'sche Verlagsbuchhandlung, Stuttgart, 455-477.

FAURE, M., BONNEAU, M. & PONS, J. 1991. Ductile deformation and syntectonic granite emplacement during the late Miocene extension of the Aegean (Greece). *Bulletin de la Société Géologique de France*, **162**, 3-11.

FEEHAN, J.G. & BRANDON, M.T. 1999. Contribution of ductile flow to exhumation of low-temperature, high-pressure metamorphic rocks: San Juan-Cascade nappes, NW Washington-State. *Journal of Geophysical Research*, **104** (B5), 10883-10902.

FLINN, D. 1962. On folding during three-dimensional progressive deformation. *Quarternary Journal of Geological Society of London*, **118**, 385-433.

FRANZ, L. & OKRUSCH, M. 1992. Aragonite-bearing blueschists on Arki Island, Dodekanese, Greece. *European Journal of Mineralogy*, **4**, 527-537.

FYTIKAS, M., INNOCENTI, F., MANETTI, P., MAZZUOLI, R., PECCERILLO, A. & VILLARI, L. 1984. Tertiary to Quaternary evolution of volcanism in the Aegean region. *In*: The geological evolution of the eastern Mediterranean (eds A.H.F. Robertson and J.E. Dixon). *Geological Society of London, Special Publication*, **17**, 687-699.

GESSNER, K., PIAZOLO, S., GÜNGÖR, T., RING, U., KRÖNER, A. & PASSCHIER, C.W. 2001b. Tectonic significance of deformation patterns in granitoid rocks of the Menderes nappes, Anatolide belt, southwest Turkey. *International Journal of Earth Sciences*, **89**, 766-780.

HOSSACK, J.R. 1968. Pebble deformation and thrusting in the Bygdin Area, Soroy, Southern Norway. *Tectonophysics*, **5**, 315-339.

JANSEN, J.B.H. & SCHUILING, R.D. 1976. Metamorphism on Naxos: Petrology and geothermal gradients. *American Journal of Science*, **276**, 1225-1253.

KATZIR, Y., MATTHEWS, A., GARFUNKEL, Z. & SCHLIESTEDT, M., 1996. The tectono-metamorphic evolution of a dismembered ophiolite (Tinos, Cyclades, Greece). *Geological Magazine*, **133**, 237-254.

KEAY, S.M. 1998. The geological evolution of the Cyclades, Greece: constraints from SHRIMP U-Pb geochronology. PhD thesis, Australian National University, Canberra.

LEE, J. & LISTER, G.S. 1992. Late Miocene ductile extension and detachment faulting, Mykonos, Greece. *Geology*, **20**, 121-124.

LISTER, G.S., BANGA, G. & FEENSTRA, A. 1984. Metamorphic core complexes of Cordilleran type in the Cyclades, Aegean Sea, Greece. *Geology*, **12**, 221-225.

LONERGAN, L. & WHITE, N. 1997. Origin of the Betic-Rif mountain belt. *Tectonics*, **16**, (3), 504-522.

MELIDONIS, N.G. 1980. The Geological Structure and Mineral Deposits of Tinos Island (Cyclades – Greece). – *The Geology of Greece*, **13**, 1-80.

ÖZER, S., SÖZBILIR, H., ÖZKAR, I., TOKER, V. & SARI, B. 2001. Stratigraphy of Upper Cretaceous-Paleocene sequences in the southern and eastern Menderes Massif. *International Journal of Earth Sciences*, **89**, 852-866.

OWENS, W.H. 1984. The calculation of a best fit ellipsoid from elliptical sections on arbitrarily oriented planes. *Journal of Structural Geology*, **6**, 571-578.

PATZAK, M., OKRUSCH, M. & KREUZER, H. 1994. The Akrotiri Unit on the island of Tinos, Cyclades, Greece: Witness to a lost terrane of Late Cretaceous age. *Neues Jahrbuch Geologischer und Paläontologischer Abhandlungen*, **194**, 211-252.

PEACH, C.J. & LISLE, R.J. 1979. A Fortran IV program for the analysis of tectonic strain using deformed elliptical markers. *Computers and Geoscience*, **5**, 325-334.

PLATT, J.P. & VISSERS, R.L..M. 1989. Extensional collapse of thickened continental lithosphere: a working hypothesis for the Alboran Sea and the Gibraltar arc. *Geology*, **17**, 540-543.

PLATT, J.P., SOTO, J.-I., HURFORD, A.J. & KELLEY, S.P. 1998. Thermal evolution, rate of exhumation, and tectonic significance of metamorphic rocks from the floor of the Alboran extensional basin, western Mediterranean. *Tectonics*, **17**, (5), 671-689.

RAMSAY, J.G. 1967. Folding and fracturing of rocks. McGraw-Hill, New York, 568p.

RAMSAY, J.G. & HUBER, M.I. 1983: The Techniques of Modern Structural Geology. Volume 1:Strain analysis. Academic Press, London, 307p.

RÉGNIER, J.L., RING, U., PASSCHIER, C.W., GESSNER, K. & GÜNGÖR, T. 2003. Contrasting metamorphic evolution of metasedimentary rocks from the Çine and Selimiye nappes in the Anatolide belt, western Turkey. *Journal of Metamorphic Geology*, **21**, 1-23.

RING, U. & BRANDON, M.T. 1999. Ductile deformation and mass loss in the Franciscan Subduction Complex: implications for exhumation processes in accretionary wedges. *In*: Exhumation Processes: Normal faulting, ductile flow and erosion, Ring, U., Brandon, M.T., Lister, G.S., Willett, S. (eds.). *Geological Society London Special Publications*, **154**, 55-86.

RING, U., BRANDON, M.T., WILLETT, S.D. & LISTER, G.S. 1999a. Exhumation processes. *In*: Exhumation Processes: Normal faulting, ductile flow and erosion, Ring, U., Brandon, M.T., Lister, G.S., Willett, S. (eds.). *Geological Society London Special Publications*, **154**, 1-27.

RING, U., LAWS, S. & BERNET, M. 1999b. Structural analysis of a complex nappe sequence and late-orogenic basins from the Aegean Island of Samos, Greece. *Journal of Structural Geology*, **21**, 1575-1601.

RING, U., GESSNER, K., GÜNGÖR, T. & PASSCHIER, C.W. 1999c. The Menderes Massif of western Turkey and the Cycladic Massif in the Aegean - do they really correlate? *Journal Geological Society London*, **156**, 3-6.

RING, U., WILLNER, A.P. & LACKMANN, W. 2001b. Stacking of nappes with unrelated pressure-temperature paths: an example from the Menderes nappes of western Turkey. *American Journal of Science*, **301**, 912-944.

RING, U., THOMSON, S.N. & BRÖCKER, M. 2003a. Fast extension but little exhumation: the Vari detachment in the Cyclades, Greece. *Geological Magazine*, **140**, 245-252.

RING, U. & LAYER, P.W. 2003. High-pressure metamorphism in the Aegean, eastern Mediterranean: Underplating and exhumation from the Late Cretaceous until the Miocene to Recent above the retreating Hellenic subduction zone. *Tectonics*, **22** (3),1022, doi: 10.1029/2001ITC001350, 23p.

ROYDEN, L. 1993. The tectonic expression of slab pull at continental convergent boundaries. *Tectonics*, **12**, 303-325.

ROSENBAUM, G., LISTER, G.S. & DUBOZ, C. 2002. Reconstruction of the tectonic evolution of the western Mediterranean since the Oligocene. *In*: Rosenbaum, G. & Lister, G.S. 2002. Reconstruction of the evolution of the Alpine-Himalayan Orogen. *Journal of the Virtual Explorer*, **8**, 107-130.

SCHLIESTEDT, M. 1990. Occurrences and stability conditions of low-temperature eclogites. *In*: Eclogite Facies Rocks (ed. Carswell, D.A.), Chapman & Hall, New York, 160-179.

SCHMÄDIKE, E. & WILL, T.M. 2003. Pressure-temperature evolution of blueschist facies rocks from Sifnos, Greece, and implications for the exhumation of high-pressure rocks in the Central Aegean. *Journal of Metamorphic Geology*, **21**, 799-811.

ŞENGÖR, A.M.C., SATIR, M. & AKKÖK, R. 1984. Timing of the tectonic events in the Menderes massif, western Turkey: implications for tectonic evolution and evidence for Pan-African basement in Turkey. *Tectonics*, **3**, 693-707.

ŞENGÖR, A.M.C. & YILMAZ, Y. 1981. Tethyan evolution of Turkey: a plate tectonic approach. *Tectonophysics*, **75**, 181–241.

SHERLOCK, S., KELLEY, S., INGER, S., HARRIS, N. & OKAY, A. 1999. ^{40}Ar-^{39}Ar and Rb-Sr geochronology of high-pressure metamorphism and exhumation history of the Tavsanli Zone, NW Turkey. *Contribution to Mineralogy and Petrology*, **137**, 46-58.

TOMASCHEK, F., KENNEDY, A., VILLA, I.M. & BALLHAUS, C. 2003. Zircons from Syros, Cyclades, Greece- Recrystallization and mobilisation during high pressure metamorphism. *Journal of Petrology*, **44**, 1977-2002.

TROTET, F., VIDAL, O. & JOLIVET, L. 2001. Exhumation of Syros and Sifnos metamorphic rocks (Cyclades, Greece). New constraints on the P-T paths. *European Journal of Mineralogy*, **13**, 901-920.

TWISS, R.J. & MOORES, E.M. 1992. Structural Geology, published by W.H. Freeman and Company, New York, 532p.

URAI, J.L., SCHUILING, R.D. & JANSEN, J.B.H. 1990. Alpine deformation on Naxos (Greece). *In*: Deformation Mechanisms, Rheology and Tectonics, Knipe, R.J. & Rutter, E.H. (eds). *Geological Society Special Publication*, **54**, 509-522.

VANDENBERG, L.C. & LISTER, G.S. 1996. Structural analysis of basement tectonites from the Aegean metamorphic core complex of Ios, Cyclades, Greece. *Journal of Structural Geology*, **18**, 1437-1454.

WEIDMANN, M., SOLOUNIAS, N., DRAKE, R.E. & CURTIS, G.H. 1984. Neogene stratigraphy of eastern basin, Samos Island, Greece. *Geobis*, **17**, 477-490.

WIJBRANS, J.R., SCHLIESTEDT, M. & YORK, D. 1990. Single grain argon laser probe dating of phengites from the blueschist to greenschist transition on Sifnos (Cyclades, Greece). *Contributions to Mineralogy and Petrology*, **104**, 582-593.

WILDI, W. 1983. La chaine tello-rifaine (Algérie, Maroc, Tunisie): structure stratigraphie et évolution du Trias au Miocène. *Revue de Géologie Dynamique et de Géographie Physique*, **24**(3), 201-297.

WILL, T., OKRUSCH, M., SCHMÄDICKE, E. & CHEN, G. 1998. Phase relations in the greenschist-blueschist-amphibolite-eclogite facies in the system Na_2O-CaO-FeO-MgO-Al_2O_3-SiO_2-H_2O (NCFMASH), with application to metamorphic rocks from Samos, Greece. *Contributions to Mineralogy and Petrology*, **132**, 85-102.

Chapter 2

The extensional Messaria shear zone and associated brittle detachment faults, Aegean Sea, Greece

Abstract

Kinematic, thermochronologic and metamorphic data are used to elucidate the tectonic nature and evolution of the ductile extensional Messaria shear zone and the associated brittle Messaria and Fanari detachment faults, which exhumed their footwall from mid-crustal depths on Ikaria Island in the Aegean. Thermobarometric data indicate that the Messaria shear zone formed at 350-400°C and 3-4 kbar, i.e. at a depth of ~15 km. Normal faulting was accompanied by the intrusion of two granites, which together with the thermobarometric data indicate a high thermal field gradient of 25-35°C km^{-1}. Zircon and apatite fission track and apatite (U-Th)/He ages demonstrate rapid cooling in the footwall of the Messaria shear zone from ~300°C to ~80°C between 11-3 Ma. The data indicate that the Messaria shear zone and the Messaria detachment slipped at rates of ~7-8 km Myr^{-1}. Kinematic indicators in the Messaria shear zone and the Messaria detachment at the northern slope of Ikaria Island show a consistent top-to-the-NNE shear sense. The sense of shear at the Fanari detachment on the southern side of the island is also top-to-the-NNE. At the southern part of the Messaria detachment, some late-stage shear-sense indicators are top-to-the-SSW and are assumed to be associated with updoming of the footwall. Numerous deformed pegmatite veins in the Messaria shear zone allow the reconstruction of deformation and flow parameters. The mean kinematic vorticity number, W_m, ranges from 0.13 to 0.69 indicating that shearing deviated significantly from simple shear and that vertical ductile thinning occurred in the subhorizontal shear zone. Finite strain shows oblate strain geometries and axial ratios of the finite strain ellipse in sections parallel to tectonic transport and normal to the mylonitic foliation range from 1.8 to 19.9. We calculate, using a one-dimensional numerical model, that ductile flow contributed ~20% to exhumation during extensional shearing. Normal faulting was the major agent exhuming the footwall from ~15 km depth.

Introduction

The extending Hellenide orogen in the Aegean Sea of Greece (Fig. 1) exposes a number of spectacular brittle low-angle normal faults (detachments) (Lister et al. 1984; Lee & Lister

1992; Gautier & Brun 1993; Ring et al. 2001a). On some Aegean islands, the brittle detachments are associated with underlying extensional ductile shear zones and impressive examples of these ductile-to-brittle extensional fault systems have been reported from the Cycladic islands of Naxos (Buick 1991) and Ios (Vandenberg & Lister 1996). It has been suggested that detachment faulting was the primary agent achieving >250 km of extension since the Miocene (Ring et al. 2003a). Some authors have even claimed that Miocene extensional faulting accomplished the complete exhumation of the Cycladic blueschist unit in the central Aegean (Lister et al. 1984).

The subhorizontal foliation in the Cycladic blueschist unit shows that ductile extensional shearing was accompanied by vertical shortening and therefore deviated from simple shear. Evidence that natural shear zones deviate significantly from progressive simple shear and are characterized by pronounced shortening perpendicular to the shear zone has been demonstrated by a number of studies (Coward 1976; Choukroune & Gapais 1983; O'Hara 1990; Bailey et al. 1994; Ring 1999). These studies indicate that ductile flow contributes to the exhumation of metamorphic rocks in footwalls of shear zones in both extensional and contractional settings. For extensional shear zones this implies that tectonic exhumation involves two exhumation processes: (1) normal faulting and (2) vertical ductile thinning (Ring et al. 1999a). A matter of debate in extensional ductile shear zones is how much ductile flow caused exhumation relative to faulting-related exhumation.

On the Island of Ikaria in the eastern Aegean Sea, a subhorizontal extensional ductile shear zone and two associated brittle detachment faults are well exposed. We have studied this extensional fault system in detail. Numerous deformed pegmatite veins in the shear zone allow the reconstruction of deformation and flow parameters (Passchier 1990). In combination with metamorphic petrology and geochronological work this allows us to constrain the amount of vertical ductile thinning associated with extension and thus to evaluate fully the tectonic significance of extensional shearing.

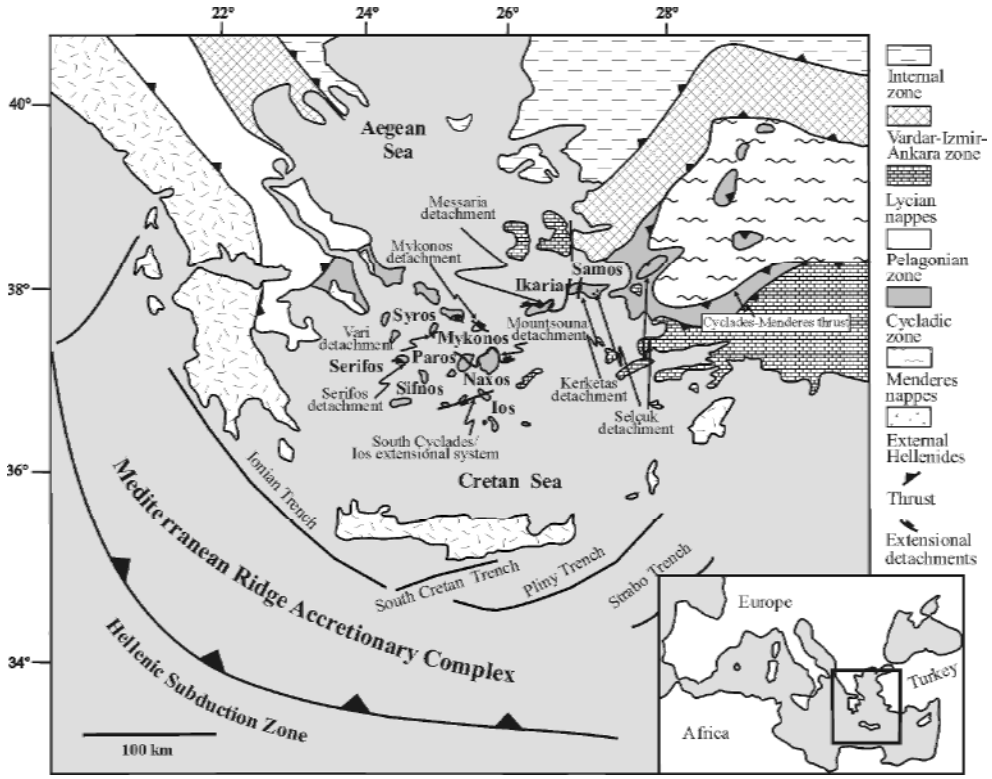

Fig. 1. Generalized map of the Aegean and adjacent mainlands showing tectonometamorphic units and Hellenic subduction zone. Inset shows location of main map.

Geological Setting

Previous research has distinguished several tectonic zones in the Hellenides characterized by rock type, stratigraphy, tectonometamorphic history and pre-orogenic palaeogeography (Robertson et al. 1991). The Cycladic zone is fringed to the north by the oceanic Vardar-İzmir-Ankara suture zone and the continental Lycian/Pelagonian zone (Fig. 1). The dominant tectonic unit of the Cycladic zone is the Cycladic blueschist unit, which comprises from top to bottom three composite nappes: (1) An ophiolitic mélange; (2) a Permo-Carboniferous to latest Cretaceous passive-margin sequence (blueschist series of Vandenberg & Lister 1996) and, (3) a Carboniferous basement, which also occurs as slices in the passive-margin sequence. The Cycladic blueschist unit is overlain on some islands by the Upper unit, which is a non- to weakly metamorphosed ophiolitic nappe that contains Pliocene sediments. In some windows in the Cycladic zone, the Basal unit, as part of the External Hellenides, crops out below the Cycladic blueschist unit (Godfriaux 1968; Avigad & Garfunkel 1989). The Cycladic blueschist unit and the External Hellenides were part of the Adriatic microcontinent. A major difference between the Aegean and adjacent western Turkey is that in the latter the Menderes nappes instead of the External Hellenides form the lowermost tectonic unit. In contrast to parts of the External Hellenides, the Menderes nappes do not show Tertiary high-

pressure metamorphism (Gessner et al. 2001a; Ring et al. 2001b; Régnier et al. 2003). The Menderes nappes are part of the Anatolian microcontinent, which collided with Eurasia further east than Adria (see tectonic reconstruction of Gessner et al. 2001a; their fig. 16). A distinctive feature of the Anatolian microcontinent is that it has a 550 Ma-age basement (Gessner et al. 2001a, 2004).

The metamorphic evolution of the Cycladic blueschist unit includes an Early Tertiary high-pressure event (~15-20 kbar and 500 ± 50°C) at ~55 Ma followed by a greenschist-facies overprint (~4-7 kbar and 400 ± 50°C on most islands; the amphibolite-facies overprint on Naxos Island is exceptional) at ~21-16 Ma (Altherr et al. 1982; Wijbrans et al. 1990; Bröcker et al. 1993, Tomaschek et al. 2003; Ring & Layer 2003). High-pressure metamorphism in the Basal unit on Evia and Samos islands is dated at 21-24 Ma (Ring et al. 2001a; Ring & Reischmann 2002).

In the Middle to Late Miocene, the Cyclades became part of the magmatic arc of the southward retreating Hellenic subduction zone as evidenced by arc-related volcanic rocks ranging from ~12-5 Ma (Fytikas et al. 1984; Weidmann et al. 1984) and granites spanning an age range from ~14-10 Ma (Keay 1998). The granites were emplaced synkinematically during major extensional detachment faulting (Faure et al. 1991; Lee & Lister 1992).

Structure and geology of Ikaria and Samos islands

The island of Ikaria belongs to the Cycladic zone. Three tectonic units can be distinguished; they are from top to bottom: (a) the non-metamorphic Fanari nappe; (b) the Messaria nappe and (c) the Ikaria nappe (Fig. 2). The general structure of Ikaria is dominated by a ~300-500 m thick ductile extensional shear zone, the Messaria shear zone, and two associated brittle detachment faults, the Messaria and Fanari detachments. The Messaria detachment is the upper crustal expression of the ductile Messaria shear zone. In the reminder of the paper we refer to this extensional detachment/shear-zone system as the Messaria extensional fault system. The Fanari detachment is not associated with an underlying carapace shear zone. The Ikaria and Messaria nappes are separated from one another by the Messaria detachment. The Messaria shear zone developed in the upper parts of the Ikaria nappe. The Fanari detachment separates the Messaria nappe from Pliocene conglomerates of the Fanari nappe. The island has an asymmetric dome-shaped architecture (Figs 2, 3). The northwestern slopes of the island dip gently to the north, which mimics the shallow northern dip of the Messaria extensional fault system. The southern slopes of Ikaria Island dip more steeply to the south.

The Pliocene conglomerates of the Fanari nappe, which is part of the Upper unit of the Cycladic zone, contain pebbles of metamorphic rocks, which are not exposed on Ikaria Island (Dürr et al. 1978). The Messaria nappe comprises metabauxite-bearing marble, graphite-rich calc-mica schist, chloritoid-kyanite-bearing phyllite, quartzite and greenschist (Altherr et al. 1982) and can be correlated with the Ampelos nappe on nearby Samos Island (Ring et al. 1999b) (Fig. 4). Both nappes are part of the passive-margin sequence of the Cycladic blueschist unit. Will et al. (1998) estimated peak pressure-temperature (P-T) conditions of ~15 kbar and ~500°C for the Ampelos nappe on Samos Island and we regard these estimates as a reasonable approximation for high-pressure P-T conditions in the Messaria nappe. The Ikaria nappe at the base is more than 1000 m thick and consists of a huge succession of metapelite as well as marble, calcsilicate rocks, amphibolite and quartzite. The Ikaria nappe was intruded by two synkinematic granites: a large I-type granite in the west and a small S-type granite in the southern part of the island (Altherr et al. 1982). The metapelite contains the amphibolite-facies mineral assemblage garnet-kyanite-staurolite-biotite-plagioclase (Altherr et al. 1982). An important question is whether the Ikaria nappe shows evidence for pre-amphibolite-facies high-pressure metamorphism, which is typical for the nappes of the Cycladic blueschist unit. If so, the P-T evolution of the Ikaria nappe would be comparable to that of the Cycladic blueschist unit on Naxos Island. Alternatively, the Ikaria nappe might be an exotic non-high-pressure unit in the Aegean and would probably correlate with the Menderes nappes of western Turkey.

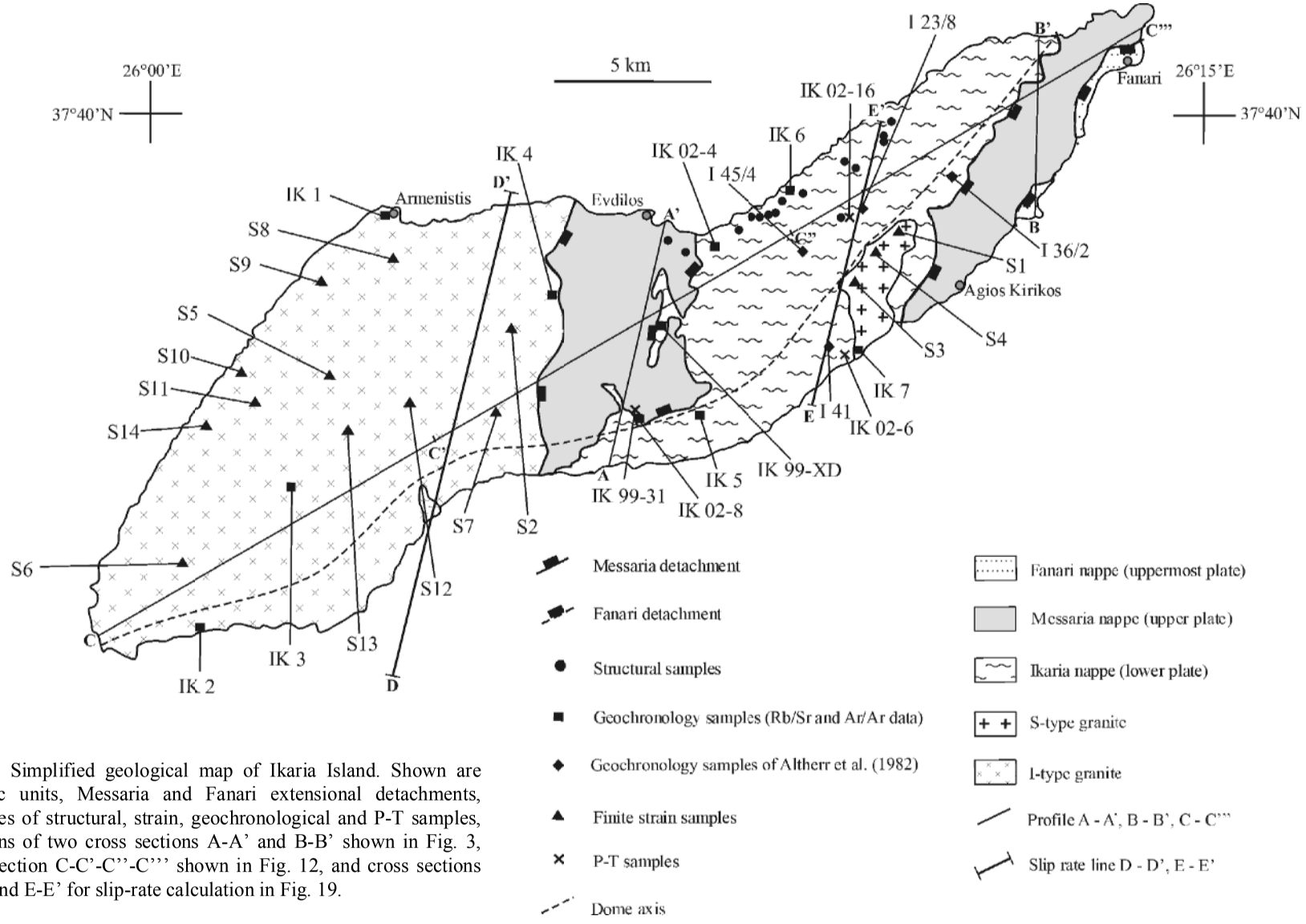

Fig. 2. Simplified geological map of Ikaria Island. Shown are tectonic units, Messaria and Fanari extensional detachments, localities of structural, strain, geochronological and P-T samples, positions of two cross sections A-A' and B-B' shown in Fig. 3, cross section C-C'-C''-C''' shown in Fig. 12, and cross sections D-D' and E-E' for slip-rate calculation in Fig. 19.

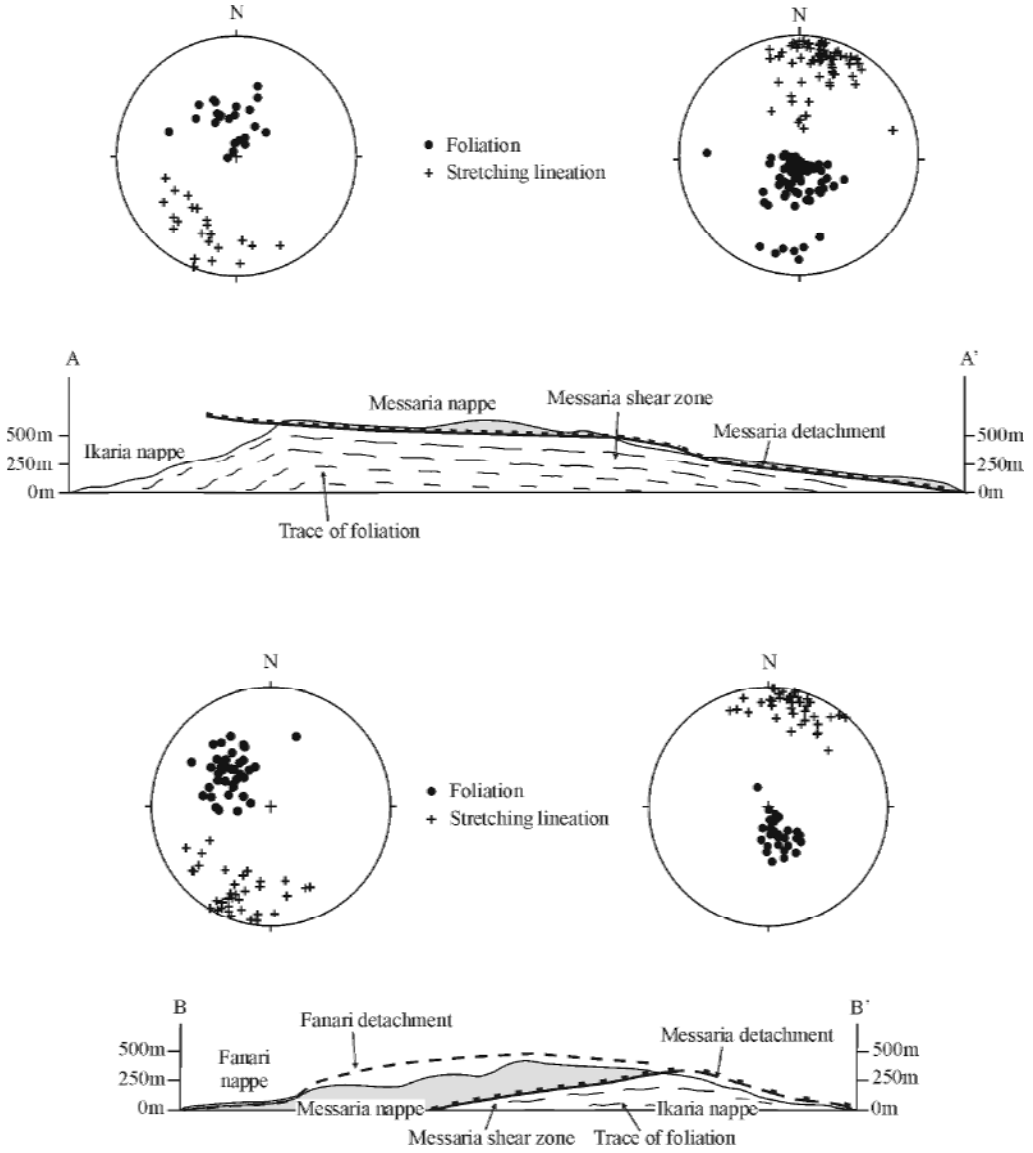

Fig. 3. Cross sections A-A' and B-B' illustrating domed architecture, which is also expressed by dip/plunge of foliations and stretching lineations on both sides of the island.

Samos Island to the east of Ikaria is made up from top to bottom by the non-metamorphic Kallithea nappe (Upper unit), which is underlain by the Selçuk (ophiolitc mélange), Ampelos and Agios Nikolaos (Carboniferous basement) nappes, all three of which belong to the Cycladic blueschist unit. Below the Cycladic blueschist unit is the Kerketas nappe, which is part of the Basal unit. Middle Miocene to Pliocene sediments occur in three graben.

Three extensional fault systems occur on Samos (Fig. 4): (1) The top-to-the-N Kallithea detachment, which separates the Kallithea nappe from the Cycladic blueschist unit and the Kerketas nappe. (2) The top-to-the-ENE Kerketas detachment between the Kerketas nappe and the overlying Ampelos nappe. The Kerketas detachment is associated with the

development of Middle Miocene graben (Weidmann et al. 1984; Ring et al. 1999b). (3) The top-to-the-ENE Selçuk extensional system between the Ampelos nappe and the Selçuk nappe.

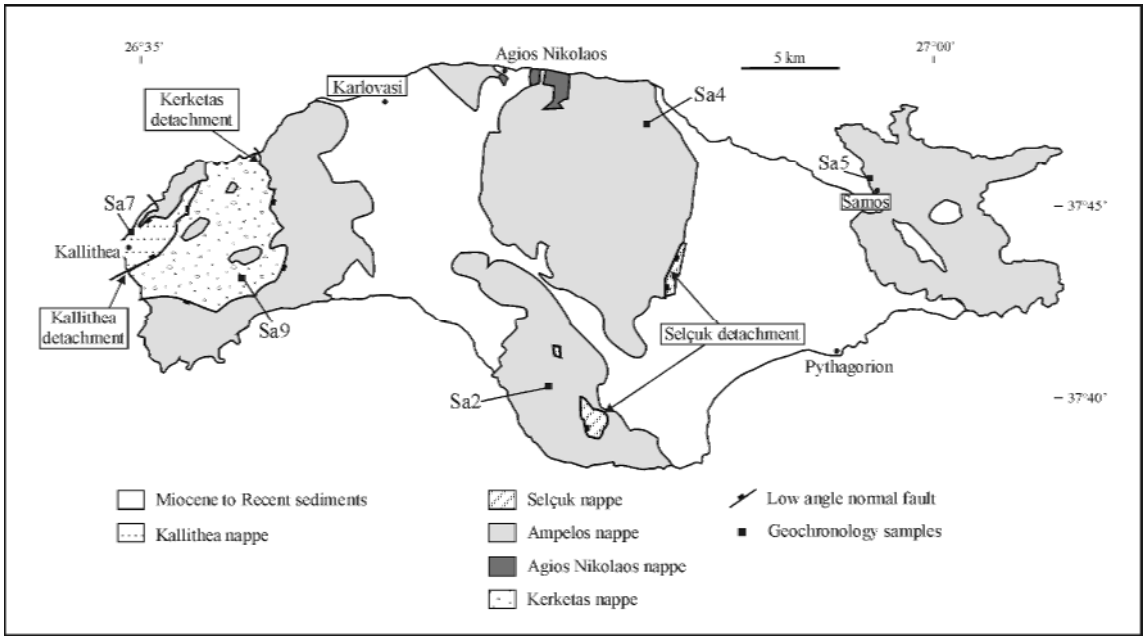

Fig. 4. Simplified geological map of Samos Island showing tectonic units with zircon fission track ages (S. Brichau, unpublished data), and Kallithea, Kerketas and Selçuk extensional fault systems.

Methods and sampling

Pressure-temperature estimates

Samples IK 02-6a and IK 02-16 from the Ikaria nappe (Fig. 2, Table 1) were studied to constrain P-T conditions of the Ikaria nappe, especially for unravelling a possible pre-amphibolite-facies high-pressure metamorphism. Sample IK 99-31 is a mylonite from the Messaria shear zone (Fig. 2, Table 1) and should constrain P-T conditions during mylonitization and thus the depth from which the shear zone was exhumed.

The mineral analyses were obtained with a Jeol Superprobe (JXA 8900RL) at Johannes Gutenberg-Universität in Mainz, Germany. A complete set of mineral analyses is given in Table 2. Operating conditions were an acceleration voltage of 15 kV, a beam current of 15 nA and 20 s counting time per element. Standards used were wollastonite for Si, corundum for Al, pyrophanite for Ti, hematite for Fe, MgO for Mg, wollastonite for Ca, albite for Na, orthoclase for K, tugtupite for Cl, F-phlogopite for F, Cr_2O_3 for Cr, rhodochrosite for Mn, ZnS for Zn. The mineral analyses are considered to be accurate within a range of ~3% (relative) on any given grain. Abbreviations used are adopted from Powell et al. (1998): bi = biotite, cd = cordierite, chl = chlorite, ctd = chloritoid, ep = epidote, fsp = plagioclase, g =

garnet, ky = kyanite, and = andalusite, sill = sillimanite, mu = muscovite, q = quartz, st = staurolite. P-T pseudosections were calculated with the THERMOCALC software (version 3.2.1) (Powell et al. 1998). Structural formulae were calculated from microprobe analyses (Table 2) using the AX software (Holland 2000).

Table 1. *P-T estimates from samples of Ikaria Island*

Sample	Latitude Longitude	P (kbar)	T (°C)	Mineral paragenesis
IK 02-16	N 37°37'31" E 26°11'13"	6-7	600	staurolite, biotite, plagioclase, kyanite
IK 02-6a	N 37°35'38" E 26°15'02"	6-8	600-650	staurolite, biotite, garnet, epidote
IK 99-31	N 37°34'48" E 26°10'32"	3.5	350-400	chloritoid, chlorite, kyanite, andalusite

Strain and rotation analysis

To quantify finite strain, quartz aggregates from deformed granites were analyzed by the R_f/ϕ and Fry methods (Ramsay 1967; Fry 1979; Ramsay & Huber 1983). The granites were emplaced during Miocene extension (see later) and therefore record extension-related finite-strain. The Fry method was applied to three samples for comparing the results with those obtained by the R_f/ϕ method (14 samples). Two-dimensional strain measurements were made on XY, XZ and YZ sections ($X \geq Y \geq Z$, finite-strain axes) in order to estimate the three-dimensional strain geometry. A least-squares best-fit ellipse was calculated for each marker outline as well as its relative position and orientation. For R_f/ϕ analysis on quartz aggregates, the long and short axes of up to 40 grains per section were measured and mean aspect ratios for each section were calculated. Tectonic strains were determined from the chi-squared minima of the R_f/ϕ analyses (Peach & Lisle 1979). For Fry analysis, the central points of more than 100 quartz and feldspar grains per section were used to calculate strain. The strain estimates were used to calculate the finite-strain ellipsoid according to the modified least-square technique of Owens (1984).

Material markers such as deformed pegmatite and quartz veins have been used for strain analysis and quantitative assessment of the non-coaxiality of deformation (Fig. 5). Passchier (1990) showed that it is sufficient to know the orientation of the boundaries between domains of material lines with different stretch histories to determine the parameters of finite

deformation, i.e. the kinematic vorticity number, W_m, the finite strain ratio, R_f, and the rate of area change, A, if deformation has accumulated by approximately steady-state flow (Passchier 1988). The technique is suitable for any exposure in which numerous veins show a variety of orientations and are shortened and extended. Deformed veins were measured in sections perpendicular to the Y axis of the strain ellipsoid. The veins can be separated into: (a) those which have only been shortened; (b) those which were shortened and then extended, and (c) those which have only been extended. The veins were plotted as vectors from a central point and cluster in four sectors which are separated by four material lines that lie parallel to the lines of no instantaneous longitudinal strain (L axes) at the beginning of deformation and at the end of deformation (Passchier 1990) (Fig. 6a). After Passchier (1990), these four lines are La_1, La_2 (La lines = "after" deformation) and Lb_1, Lb_2 (Lb lines = "before" deformation). The parameters of finite deformation can be calculated from Mohr diagrams. We used the Mohr circle for the stretch tensor, H (Fig. 6b), which relates particle positions in the deformed state back to the original undeformed state compared to the reciprocal tensor, F. The position and size of the circle can be defined by the parameters T, Q and R, which are also used for the calculation of W_m [$W_m = Q/R$] and R_f [$(T+R)/(T-R)$]. The angle ψ between La_1 and La_2 can be used to calculate A [$A = \cos(\psi/2)$] (Fig. 6b).

Another method to estimate W_m is to measure the axial ratio, R, of a particle and the angle between the maximum elongation of the particle and the shear plane (blocked-object method of Passchier 1987). For $W_m = 1$, i.e. simple shear, all particles which behave as active markers with $R \geq 1$ will rotate freely as the shear strain increases and the rate of rotation equals the rate of stretching. If W_m is lower than 1, i.e., a component of pure shear accompanies shearing (general or sub-simple shear of Simpson and De Paor 1993), the rotation of particles with progressively smaller aspect ratios is subdued (Cowan 1990). For any flow regime with $W_m < 1$, not all rigid particles are free to rotate continuously. Particles with an aspect ratio above a certain critical value, R_c, will rotate until they reach a stable orientation. For aspect ratios less than the critical value, rotation is unrestricted. The value of R_c that divides freely rotating objects from those that have reached a stable orientation is a function of the degree of non-coaxiality: $W_m = (R_c^2 - 1)/(R_c^2 + 1)$ (Passchier 1987).

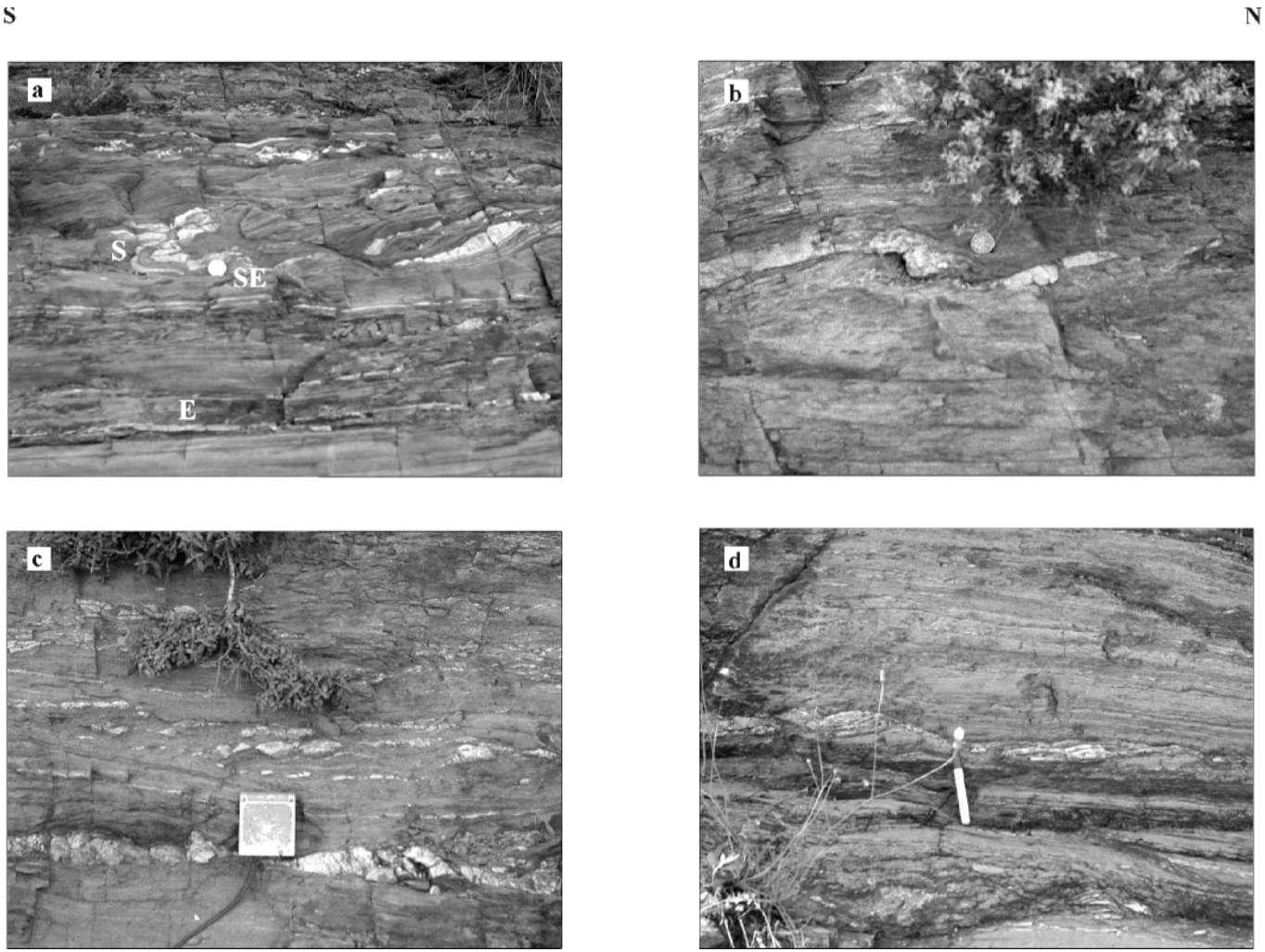

Fig. 5. Photographs of sheared quarzite and pegmatite veins in metapelite of the Ikaria nappe. The shear sense is always top-to-the-N. (a) Outcrop with folded pegmatitic veins (S), extended veins (E) and also folded and boudinaged veins (SE). (b) Folded pegmatitic vein. (c) Outcrop with boudinaged veins. (d) Folded and then extended veins.

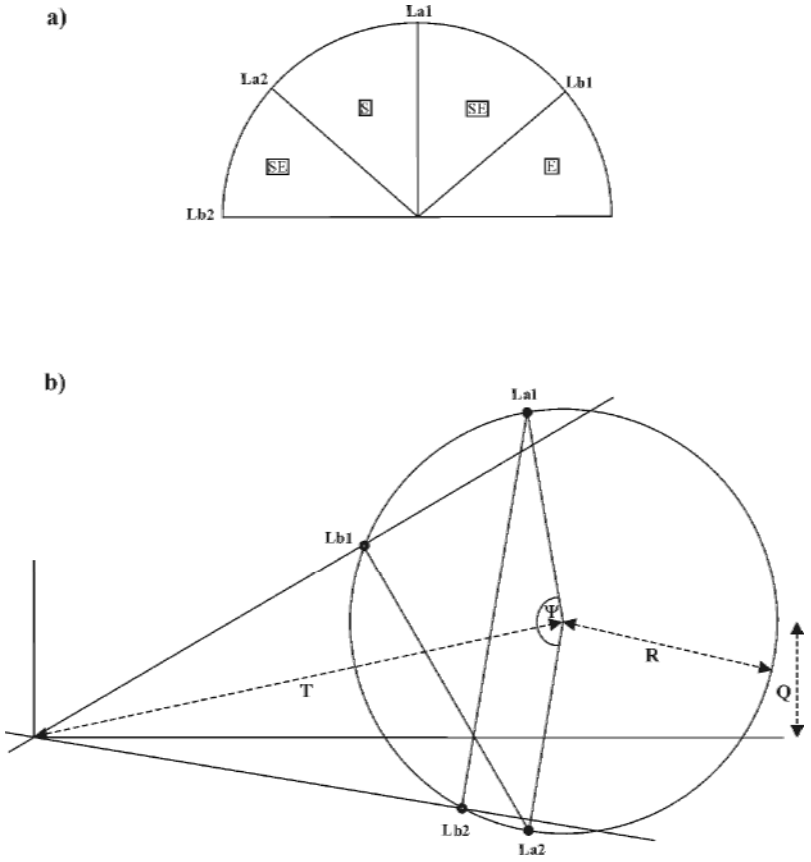

Fig. 6. (a) Classification of the veins in four sectors. La_1 and La_2 are the boundaries between the material lines that were only shortened and those that were first shortened and then extended. Lb_1 and Lb_2 are the boundaries between lines that were first shortened followed by extension and those which were only extended. (b) Mohr circle for H representing finite deformation in stretch space. The size and position of the circle can be defined by three parameters: the distance of the centre of the circle from the origin (T), the radius of the circle (R) and the distance of the centre of the circle from the horizontal axis (Q). Also the boundaries of the different sectors (La_1, La_2 and Lb_1, Lb_2) are produced into the circle. The angle between La_1 and La_2 is Ψ.

$^{87}Rb/^{86}Sr$ geochronology

Rocks of the shear zone generally show a very strong mylonitic foliation. However, the last fabric-forming deformation increments occurred at conditions close to the lower temperature limit of crystal-plastic deformation of albitic feldspar. This resulted in local, partial preservation of high-shear-strength mineral clasts (like plagioclase 'augen') within the mylonites.

Various attempts at dating mylonitic deformation in felsic rocks have shown that the late increments of synkinematic recrystallization may be successfully dated using $^{87}Rb/^{86}Sr$ mineral systematics (Müller et al. 1999, Hetzel & Glodny 2002, Reddy et al. 2003, Müller 2003). Crucial for linking isotope information unequivocally to textural evolution is (a) that deformation fabrics formed at temperatures lower than necessary for thermally induced intermineral diffusional isotope exchange, and (b) that sampling is texturally controlled, i.e.

that only minerals from thoroughly recrystallized domains are used. As we will show below, temperatures during mylonitization were 350-400°C, i.e. below the activation temperatures for Sr diffusion in white mica and feldspar. However, the identification of rock domains with microtexturally pervasive synkinematic recrystallization posed difficulties.

Two samples were selected for $^{87}Rb/^{86}Sr$ mineral analysis. Sample IK 99XD is a very fine-grained, mylonitic quartzitic schist composed of quartz and K-feldspar, with minor albite, white mica, apatite, and biotite. Obvious feldspar and mica textural relics are not observed. Sample IK02-4 is an intensely deformed granitic pegmatite, further referred to as metapegmatite. The mineral assemblage comprises quartz, K-feldspar, albitic plagioclase, white mica, apatite, tourmaline, and garnet. While most of the rock is synkinematically recrystallized, the pegmatitic nature of the protolith is still obvious from local megacrystic relics of phases with high shear strength (plagioclase, garnet, tourmaline, white mica). Mica fish reach sizes of up to 1 cm. $^{87}Rb/^{86}Sr$ isotope systematics of texturally defined generations of white mica in metapegmatites can be used to define both deformation and protolith age (Glodny et al. 1998). We therefore analyzed separated minerals from an apparently pervasively deformed, 5 cm^3-sized domain as well as only slightly bent and kinked inner portions of two primary, pegmatitic white mica crystals. Analytical procedure details are those of Glodny et al. (2002).

$^{40}Ar/^{39}Ar$ geochronology

For the $^{40}Ar/^{39}Ar$ dating single grains were degassed with a laser-probe using spot ablation on grains in sections. The $^{40}Ar/^{39}Ar$ dating has been applied to sections (~1 x 0.5 cm), which were polished on one side and afterwards cleaned in ethanol and distilled water. The sections were packed in aluminium foil and irradiated for 70 hours in the McMaster nuclear reactor (Canada) with MMHb hornblende neutron flux monitor dated at 520.4 ± 1.7 Ma (Samson & Alexander 1987). After irradiation, the sections were placed on a Cu-holder inside an UHV gas extraction system and baked for 48 hours at 200°C. The analytical device consists of: (1) a multiline continuous 6 W argon-ion laser, (2) a beam shutter for selection of exposure times, (3) divergent and convergent lenses for definition of the beam diameter, which can produce a pit with a size varying from 50 to 100 μm in diameter for the spot fusion, (4) a CCD camera to monitor the experiments, (5) a small inlet line for the extraction and purification of gases and (6) a MAP 215-50 noble gas mass spectrometer.

The sections were placed on a copper plate, and the spot ablation was achieved using an exposure time of 30 ms for each spot on the beam shutter. Heating for the analyses was made

with a focussed or defocussed laser beam depending on the procedure chosen for degassing. Each analysis involves 5 min for lasering and gas cleaning and 15 min for data acquisition by peak switching from mass 40 to 36, through 10 sets of data. System blanks were evaluated every three analyses and range around 2.10^{-12} cc for ^{40}Ar and 3.10^{-14} cc for ^{36}Ar. For each spot ablation analysis, classical isotope corrections including blanks, mass discrimination radioactive decay of ^{37}Ar and ^{39}Ar and irradiation-induced mass interference were applied. The quoted errors represent one-sigma deviation and were calculated following McDougall and Harrison (1988).

Low-temperature thermochronology

Seven samples for fission track analysis on zircon and apatite and for (U-Th)/He dating on apatite were collected on Ikaria and another five samples on Samos (Figs 2, 4, Table 7). Spontaneous fission tracks were revealed by etching polished apatite and zircon grain mounts with 6.5 % HNO_3 at 20°C for 40 s and a mixture of potassium hydroxide and sodium hydroxide at 225°C for 30 to 40 h, respectively. The samples were irradiated with muscovite external detectors and Corning dosimeter glass CN-5 (apatite) and CN-2 (zircon) at the radiation center of Oregon State University, USA. The neutron doses applied on apatite were $1{\cdot}10^{16}$ ncm^{-2} for apatite and $8{\cdot}10^{14}$ ncm^{-2} for zircon. Fission track densities were measured on grains oriented parallel to the C axis using a Zeiss Axioplan optical microscope at 1250x magnification at the University of Montpellier, France. Ages ($\pm 1\sigma$) were calibrated by the zeta method (Hurford & Green 1982), using a zeta factor of 127 ± 4 (apatite) and 330 ± 8.5 (zircon) determined by multiple analyses of zircon and apatite age standards following the recommendations of Hurford (1990). Ages were calculated using the central-age method of Galbraith (1992) which allows for non-Poissonian variation within a population of single-grain ages belonging to an individual sample. Between ~300-200°C (for zircon, Tagami et al. 1998) and ~110-60°C (for apatite, Green et al. 1986), tracks are partially annealed (shortened). The regions in the crust that coincide with these temperature ranges are the partial annealing zones (PAZ). At temperatures below 200°C for zircon and 60°C for apatite, tracks are generally retained at their initial lengths.

(U-Th)/He dating on apatite is based on the accumulation of radiogenic He from the decay of U and Th series nuclides (Zeitler et al. 1987). Laboratory diffusion experiments on a range of apatites indicate that the helium is partially retained at temperatures between 80°C and 40°C. These values are apparently insensitive to chemical composition and only slightly sensitive to grain size (Wolf et al. 1996). The depth range that corresponds to this temperature range is the

helium partial retention zone (PRZ). At temperatures below 40°C most helium is retained in the apatite crystal while above 80°C most of the helium is lost. He age determinations were made at the California Institute of Technology, USA, and analytical details are described in House et al. (1997). He, U and Th determinations are made on a single aliquot of four apatite grains, typically 100 μm in minimum dimension. Helium was determined by mass spectrometry after quantitative He degassing of apatites at 1050°C for 5 min with a Nd-YAG laser. Grains were retrieved from the vacuum system, dissolved in 10% HNO_3, spiked with ^{230}Th and ^{235}U, and analyzed for U and Th on an ICP-MS. Reported He ages are corrected for alpha ejection effects based on measured grain dimensions (Farley et al. 1996). Ages were determined in replicate and the mean is reported. The estimated analytical uncertainty for He ages is about 6% (1σ), in agreement with the reproducibility observed for most samples.

Metamorphism of the Ikaria nappe

Mineralogy

Sample IK 02-06a contains the mineral assemblage garnet, staurolite, biotite and rare epidote (+ muscovite + quartz). Garnet has a general grain size of about 3 mm and its composition is almandine (70-73%), pyrope (5-10%), spessartine (5-10%) and grossular (12-18%). Garnet has no major element zoning (Table 2), mineral formulae do not show significant Fe^{3+} and therefore we assumed that $Fe^{2+} = Fe^{total}$. Staurolite occurs, together with chlorite, as inclusions in garnet or in the matrix in equilibrium with biotite and garnet (Fig. 7). Epidote also forms inclusions in garnet or occurs in the matrix in equilibrium with biotite. Chlorite only occurs as inclusions in garnet. The Si content of white mica in the matrix is 3.11-3.12 (on the basis of 11-oxygen structural formula).

The general paragenesis in sample IK 02-16 is staurolite-biotite-plagioclase-kyanite-chlorite (Fig. 7). Plagioclase has andesine composition and shows a zonation from An_{43} (core) to An_{50} (rim) (Table 2). Kyanite occurs in plagioclase, and in textural equilibrium with staurolite, plagioclase and biotite in the matrix. Rare chlorite is in equilibrium with biotite and staurolite. The Mg content of chlorite is ~3 per formulae unit (based on 14-oxygen structural formula) and therefore we consider chlorite to be primary. Staurolite is widespread in the matrix, and also occurs as inclusions in plagioclase. The Si content in white mica varies from 3.10 to 3.15 (on the basis of 11-oxygen structural formula).

In sample IK 99-31 chloritoid is in equilibrium with kyanite, andalusite and chlorite. Kyanite also occurs as an inclusion in chloritoid. The sample is characterized by the lack of biotite.

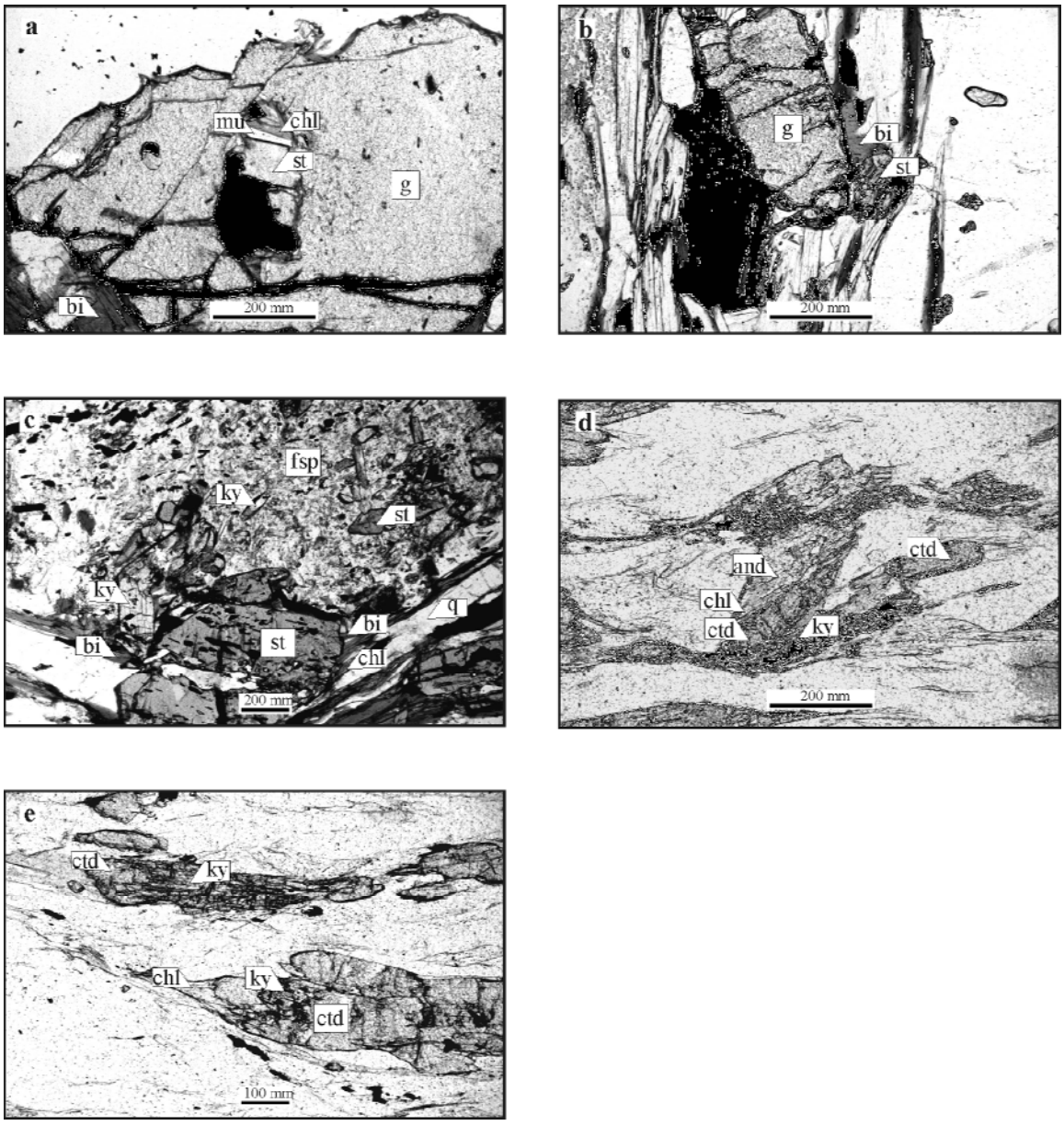

Fig. 7. Microphotographs of samples from the Ikaria nappe and the Messaria shear zone. (a) Sample IK 02-6a showing staurolite-biotite-garnet paragenesis. Staurolite, chlorite and muscovite are inclusions in garnet. (b) Staurolite, chlorite and muscovite in equilibrium with biotite and garnet in the matrix; sample IK 02-6a. (c) Sample IK 02-16 showing chlorite-staurolite-biotite-kyanite paragenesis. Staurolite is in equilibrium with plagioclase and biotite or occurs as an inclusion in plagioclase. Kyanite is an inclusion in plagioclase or is in equilibrium with staurolite, plagioclase and biotite. Chlorite is in equilibrium with biotite and staurolite in the matrix. (d) Chloritoid in equilibrium with kyanite, chlorite and andalusite in sample IK 99-31. (e) Kyanite as an inclusions in chloritoid; sample IK 99-31.

Table 2. *Mineral analyses*

Sample	IK 02-06a	IK 02-16	Sample	IK 02-06a	IK 02-06a	IK 02-06a	IK 02-06a	IK 02-06a	IK 02-06a	IK 02-06a	IK 02-06a	IK 02-06a	IK 02-06a	IK 02-16	IK 02-16	IK 02-16	IK 02-16	IK 02-16	IK 02-16	IK 02-16	IK 02-16
WR	W %	W %	Min.	bi/65	st/52	g/60/rim	g	g/core	g	g /rim	ep	mu	mu	bi /83	st/84	chl /92	bi /93	st/100	mu	mu	fsp /rim
SiO_2	63.64	62.99																			
TiO_2	1.29	1.50	SiO_2	35.80	28.15	37.89	37.80	38.04	37.88	37.89	37.82	45.82	45.96	36.13	27.96	25.55	36.05	27.91	45.41	45.27	54.74
Al_2O_3	16.74	16.86	TiO_2	1.63	0.58	0.03	0.01	0.02	0.01	-	0.17	0.38	0.48	1.39	0.43	0.12	1.38	0.59	0.54	0.51	-
Cr_2O_3	-	-	Al_2O_3	20.89	52.60	21.11	20.88	20.81	20.81	20.87	25.07	33.86	33.27	19.09	53.74	22.98	19.04	53.53	33.41	33.07	27.91
Fe_2O_3	8.16	8.76	Cr_2O_3	0.13	0.08	0.04	-	0.09	-	-	0.01	0.05	-	0.07	0.03	-	0.02	0.07	0.05	0.06	0.04
FeO	-	-	Fe_2O_3	-	-	-	-	-	-	-	10.98	-	-	0.81	-	-	1.07	-	-	-	0.11
ZnO	-	-	FeO	17.47	12.36	32.66	32.81	32.61	32.69	33.24	0.10	2.60	2.69	15.56	12.33	17.94	14.80	12.75	2.73	0.05	-
MnO	0.08	0.08	ZnO	-	1.65	-	-	-	-	-	-	-	-	-	0.14	-	-	0.21	-	-	-
MgO	1.07	2.12	MnO	0.06	0.14	0.97	0.86	0.65	0.40	0.43	0.31	0.02	0.01	0.15	0.46	0.23	0.13	0.53	-	-	-
CaO	0.53	1.59	MgO	8.99	1.23	2.63	2.64	2.37	2.22	2.29	0.05	0.53	0.64	12.47	1.98	19.79	12.78	2.18	0.74	0.62	-
Na_2O	0.31	0.90	CaO	0.02	0.02	5.42	4.89	5.45	5.48	5.35	22.53	0.02	0.01	-	0.02	0.02	0.08	-	-	-	10.38
K_2O	4.48	3.06	Na_2O	0.24	-	-	0.03	0.08	0.03	0.01	-	0.87	0.92	0.25	0.01	0.01	0.27	-	1.08	1.01	5.67
P_2O_5	0.18	0.18	K_2O	9.38	-	0.01	-	-	-	-	-	9.74	9.84	8.95	0.01	-	8.67	-	9.51	9.65	0.08
fluid	2.81	1.75																			
Totals	99.29	99.79	Totals	94.62	96.81	100.77	99.92	100.11	99.51	100.08	97.06	93.90	93.84	94.88	97.12	86.64	94.29	97.77	93.48	90.24	98.92
	Mole %	Mole %	Oxygen	11	46	12	12	12	12	12	12.5	11	11	11	46	14	11	46	11	11	8
SiO_2	66.67	66.80																			
TiO_2	1.02	1.20	Si	2.71	7.91	3.01	3.03	3.04	3.04	3.03	3.01	3.11	3.12	2.71	7.78	2.62	2.71	7.74	3.10	3.15	2.49
Al_2O_3	10.33	10.54	Ti	0.09	0.12	-	-	-	-	-	0.01	0.02	0.02	0.08	0.09	0.01	0.08	0.12	0.03	0.03	-
Cr_2O_3	-	-	Al	1.86	17.41	1.98	1.97	1.96	1.97	1.97	2.35	2.71	2.67	1.69	17.62	2.78	1.69	17.49	2.69	2.72	1.50
Fe_2O_3	-	-	Cr	0.01	0.02	-	-	0.01	-	-	-	-	-	-	0.01	-	-	0.02	-	-	-
FeO	6.43	6.99	Fe^{3+}	-	-	-	-	-	-	-	0.66	-	-	0.05	-	-	0.06	-	-	-	-
ZnO	-	-	Fe^{2+}	1.11	2.90	2.17	2.20	2.18	2.20	2.22	0.01	0.15	0.15	0.98	2.87	1.54	0.93	2.96	0.16	-	-
MnO	0.07	0.07	Zn	-	0.34	-	-	-	-	-	-	-	-	-	0.03	-	-	0.04	-	-	-
MgO	1.67	3.35	Mn	-	0.03	0.07	0.06	0.04	0.03	0.03	0.02	-	-	0.01	0.11	0.02	0.01	0.12	-	-	-
CaO	0.59	1.81	Mg	1.01	0.51	0.31	0.32	0.28	0.27	0.27	0.01	0.05	0.07	1.39	0.82	3.02	1.43	0.90	0.08	0.06	-
Na_2O	0.31	0.93	Ca	-	0.01	0.46	0.42	0.47	0.47	0.46	1.92	-	-	-	0.01	-	0.01	-	-	-	0.51
K_2O	2.99	2.07	Na	0.04	-	-	0.01	0.01	-	-	-	0.11	0.12	0.04	-	-	0.04	-	0.14	0.14	0.50
P_2O_5	0.08	0.08	K	0.91	-	-	-	-	-	-	-	0.84	0.85	0.86	-	-	0.83	-	0.83	0.86	-
fluid	9.83	6.18																			
Totals	100.00	100.00	Sum	7.74	29.26	8.00	7.99	7.99	7.98	7.99	7.98	7.00	7.01	7.79	29.32	9.99	7.78	29.39	7.02	6.96	5.01

Thermobarometry

P-T conditions for the Ikaria unit (IK 02-06a and IK 02-16) were estimated via pseudosections using the KFMASH system based on whole-rock analyses (Table 2). P-T conditions for sample IK 99-31 were deduced from the mineral paragenesis.

The pseudosection and AFM projections (Fig. 8) constrain P-T estimates for IK 02-06a at 6-8 kbar for a temperature of 600-650°C. Isopleths of phengitic substitution do not provide precise information on pressure. This is mainly due to the influence of Na in white mica and small-scale variations of whole-rock compositions in the sample (Wei & Powell 2003). However, the isopleths suggest that the maximum pressure was <8 kbar. The size of garnet (3 mm) does not allow any significant fractionation of the whole-rock composition. Because chlorite and staurolite occur as inclusions in garnet, the P-T path is probably clockwise (Fig. 8a).

P-T estimates for IK 02-16 are better constrained because the bulk-rock composition of this sample allows the paragenesis staurolite-biotite, but not the paragenesis garnet-biotite-staurolite. This implies a pressure <7 kbar (Fig. 8b). Another indication for pressures <7 kbar is the chlorite-biotite-staurolite paragenesis, which is likely metastable in this sample (Fig. 8b). The stable field for this paragenesis is near the staurolite-biotite trivariant field at pressures <7 kbar. Because kyanite is present, pressures are >6 kbar for a temperature of 600°C.

A very important conclusion is that there is no evidence for any high-pressure metamorphism pre-dating amphibolite-facies metamorphism in samples IK 02-6a and IK 02-16 from the Ikaria nappe. Reconaissance thin-section work on samples from the Ikaria nappe also do not show any signs for high-pressure relics. Altherr et al. (1982) also did not report any evidence for high-pressure metamorphism in the Ikaria nappe.

The occurrence of kyanite and andalusite in equilibrium in IK 99-31 from the Ikaria shear zone constrains the pressure at 3-4 kbar. The presence of chloritoid with chlorite-aluminosilicate and the lack of biotite suggest temperatures of 350-400°C. The data indicate a relatively high thermal field gradient of 25-35°C km^{-1} during movement in the Messaria shear zone. The intrusion of the two synkinematic granites are in line with an elevated geotherm. The P-T data reflect the physical conditions during mylonitization in the Messaria shear zone.

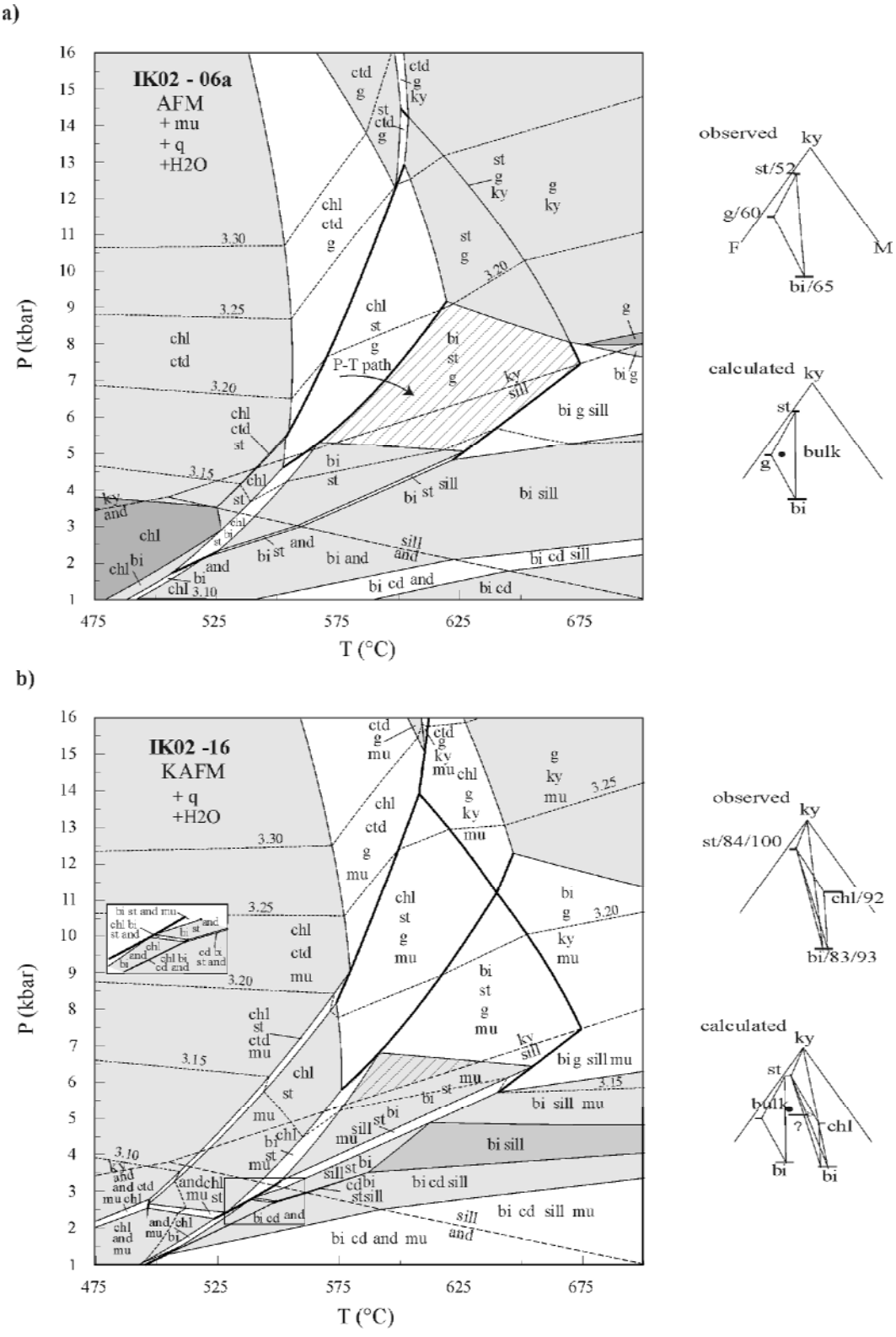

Fig. 8. Pseudosections and AFM diagrams; phengitic substitution in white mica are shown by dashed lines in both pseudosections; the projection of the bulk rock composition is labelled bulk for both samples in the AFM diagrams. (a) Sample IK 02-06a; projections into an AFM diagram are based on the mineral formulae (Table 2) of muscovite (pure end member), quartz and water; same projections calculated by THERMOCALC are also shown. P-T conditions of 6-8 kbar for a temperature of 600-650°C are indicated (hatched field in pseudosection); possible P-T path is shown. (b) Sample IK 02-16; projections based on mineral formulae (observed) and calculated by THERMOCALC are shown. P-T conditions of 6 kbar and 600°C (hatched field in pseudosection) are indicated.

Structural data

The stretching lineations associated with extensional shearing show a consistent NNE-SSW orientation, the lineations plunge to the north in the northeastern part of the island and to the south in the southern part (Fig. 3). Shear bands associated with the stretching lineations in the Messaria shear zone are consistently top-to-the-NNE (Fig. 9). The shear bands developed during greenschist-facies metamorphism and the amphibolite-facies mineral assemblages in the Ikaria nappe were completely retrograded under mid-greenschist-facies conditions in the shear zone. In incipiently sheared rocks, asymmetric strain shadows around garnet contain chlorite, white mica and quartz and developed during garnet break down. Biotite is converted to chlorite in the shear bands. Staurolite breaks down to white mica and chlorite. In highly sheared rocks, relics of the amphibolite-facies assemblage are completely lacking and the mylonite is made up of greenschist-facies mineral assemblages. In the Messaria nappe, kyanite and chloritoid in weakly sheared rocks have cracks that are filled with chlorite and quartz. Rare biotite is strongly chloritized. Mylonitic rocks usually have ribbon quartz and rotated albite porphyroclasts.

Large parts of the I-type granite in the southwestern corner of Ikaria are virtually undeformed and exhibit magmatic fabrics. Aligned igneous minerals of euhedral potassium feldspar, plagioclase, biotite and hornblende in an undeformed quartz matrix define a magmatic foliation. Thin-section analysis shows that the minerals forming the magmatic foliation do not show any signs of deformation or recrystallization. In the upper parts of the granite, the magmatic foliation has a subhorizontal orientation. Here a weak NNE-trending magmatic lineation is defined by preferred orientation of the long axes of prismatic potassium feldspar. In its uppermost parts, the I-type granite is progressively deformed into mylonite and ultramylonite with a subhorizontal tectonic foliation associated with a very strong NNE-trending stretching lineation. The mylonitic foliation is defined by medium- to fine-grained flattened and strongly elongated quartz grains, quartz-feldspar aggregates and aligned mica. The foliation may be spaced at the millimetre scale or is extremely narrowly spaced at the micron scale. The lineation is expressed by stretched quartz, smeared-out mica and recrystallized quartz tails around feldspar porphyroclasts. Quartz commonly formed polycrystalline ribbons and shows undulatory extinction, dynamic recrystallization and grain-boundary migration. Micas are commonly recrystallized into small new grains, which define C planes that lie at a small angle to the mylonitic foliation. The smaller S-type granite shows basically the same structural development and we argue that both granites were intruded synkinematically into the Messaria shear zone.

In the Messaria shear zone, asymmetric folds occur on the dm to m scale (Fig. 5a, b). The asymmetry of the folds is consistent with top-to-the-NNE shear (Fig. 9b). The shear direction

as deduced from the asymmetric folds is consistent with the orientation of the stretching lineations. The ductile structures show a progressive evolution into semi-ductile and brittle deformation associated with the brittle Messaria detachment. The detachment zone is made up of brecciated cataclasite in which rocks from the foot- and hangingwall are intermixed. In the Messaria nappe, marble is brecciated and jointed. Faults with offsets on the 10-100 m scale subdivide the marble into a number of tilted blocks in the hangingwall of the detachment. The sense of tilting is consistent with top-to-the-NNE displacement. Fault-slip analysis on faults in the Messaria nappe also indicates a consistent NNE-SSW-oriented extension direction (Fig. 10a-f). Throughout the upper parts of the I-type granite, potassium feldspar porphyroclasts and hornblende show brittle micro-normal faults at moderate to high angles to the mylonitic foliation. These microfaults are commonly pulled apart feldspar and hornblende and growth of new quartz and biotite occurred between the displaced crystals. Directly underneath the detachment fault, granite mylonite is brecciated and fractured and cataclasite and ultracataclasite occur. Very fine-grained retrograde chlorite is common in the breccia zones and feldspar is severely altered to sericite.

The Fanari detachment at the contact between the Messaria and the Fanari nappe is a cataclasite zone. The cataclastic rocks have a rubbly to fragmental appearance and show numerous mesoscopic brittle faults. The fault planes are characterized by anastomosing clayey and carbonatic gouge layers with thin (1 mm to 10 cm) zones of cataclasite, breccia and hematite-clay-coated fractured rock. Bleaching and alteration of intact rock occurs in the vicinity of faults. Weakly oriented phacoid-shaped tectonic slivers of country rock within the fault zone are on the cm to dm scale. The fault surfaces contain Riedel shears associated with lunate and crescentric structures at their intersections with the fault plane. The cataclastic fabrics record a top-to-the-NNE sense of shear. The cataclastic shear zone of the Fanari detachment is dissected by numerous small-scale faults. Fault-plane analysis shows that most of these faults have a normal sense of slip and dip at 50-70° to the south; a minor, conjugate set of normal faults dips at 60-80° to the N (Fig. 10g).

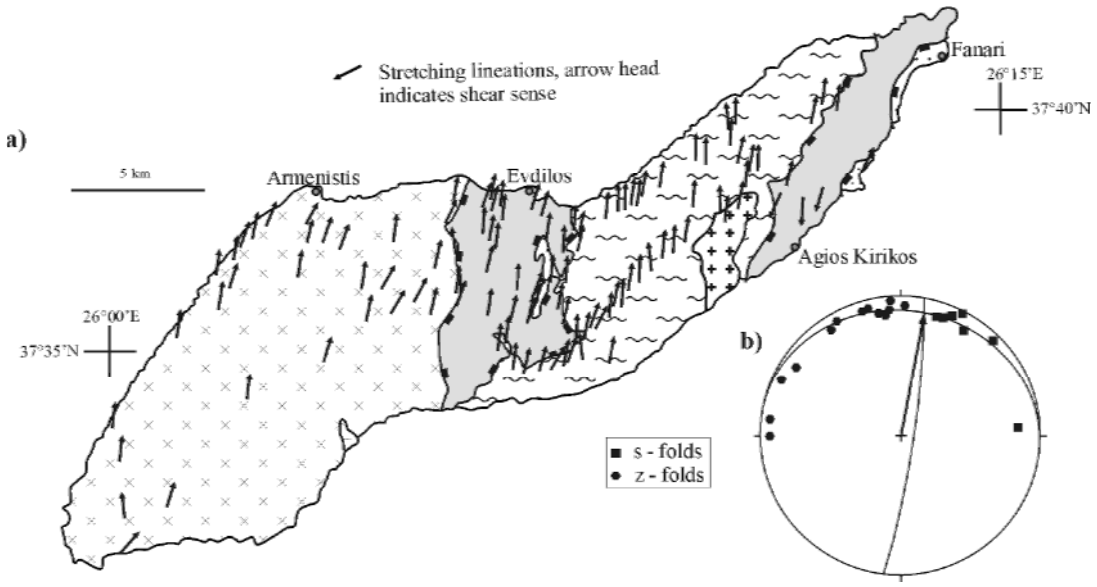

Fig. 9. (a) Map showing the orientation of stretching lineations; arrow head indicates sense of shear of hangingwall. (b) Stereogram showing asymmetric folds in the Messaria shear zone; the sense of asymmetry is assigned on the basis of the vergence of the fold when viewed in a down-plunge direction and the axis and the sense of asymmetry of each fold are plotted in a lower-hemisphere projection according to the convention of Cowan and Brandon (1994); the fold axes define a girdle, which parallels the orientation of the shear plane and plot as two distinct "S" and "Z" groups. The shear direction for the shear zone can be determined from the intersection of the shear plane (average girdle of "S" and "Z" axes) and the mirror plane; the shear direction is top-to-the-NNE.

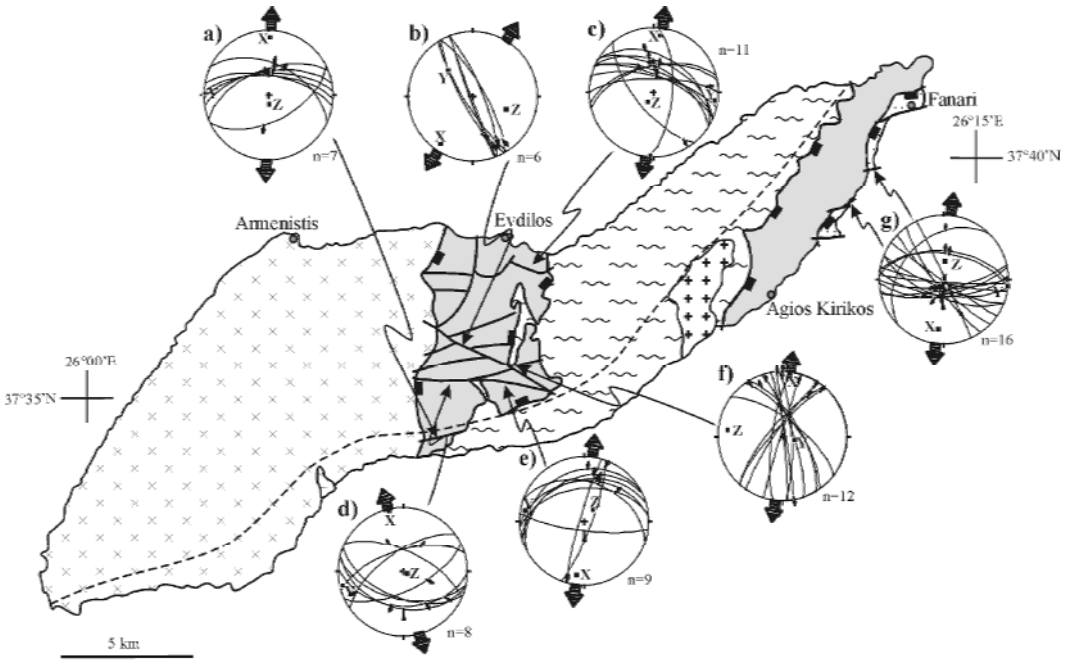

Fig. 10. Fault-slip analysis. Most small-scale faults associated with Messaria detachment dip at angles of 30-60° to the NNE, S-dipping normal faults are distinctly steeper than the N-dipping ones, NE-striking strike-slip faults are dextral and NW-striking ones are sinistral. Large arrows indicate extension directions.

Strain and rotation analysis

Finite strain and rotation

The sample localities for finite strain analysis are shown in Figure 2, the strain data are summarized in Table 3 and shown in Figure 11, which shows the relative shapes of the strain ellipsoids, i.e. prolate vs oblate. According to Hossack (1968), this classification is called strain symmetry. To infer strain type, i.e. constrictional vs flattening, information on volume strain is needed.

To prove that strain analysis by the R_f/ϕ method yields meaningful results one has to demonstrate that the measured objects deformed homogeneously with their matrix. Finite strains determined with the normalized Fry technique were primarily used to check the R_f/ϕ estimates. The Fry strains are thought to represent matrix strain, whereas the R_f/ϕ strains describe the fabric ellipsoid or clast strain (Ramsay & Huber 1983). As shown in Figure 11 and Table 3, Fry strains are not fundamentally different from R_f/ϕ strains; in some cases, the R_f/ϕ strains are slightly greater than the Fry strains, whereas in other cases the opposite is the case. Therefore, we conclude that there was no significant difference in deformation behaviour between the quartz-mica matrix and the quartz porphyroclasts during the accumulation of finite strain in the granites.

The strain ellipsoids have mostly oblate strain symmetry with some data points in the prolate field (Fig. 11). The axial ratios in XZ sections range from 2.4 to 19.9 with S_X ranging from 1.19 to 7.17 (Table 3). The stretches in the Z direction, S_Z, range from 0.31 to 0.61, indicating strong vertical shortening of 39% to 69%. S_Y ranges from 0.94 to 1.58, showing mainly extension in this direction. The strain data verify pronounced heterogeneous deformation of the granites (Fig. 12) as apparent in the field.

We have no direct control of possible volume changes during deformation. Volume changes are basically controlled by loss or gain of silica (O'Hara 1990; Bailey et al. 1994; Feehan & Brandon 1999). If the granites were affected by considerable volume change they should either be distinctly enriched or depleted in silica in the shear zone. Neither is observed in the two granites, the chemistry of them does not change towards and within the Messaria extensional fault system. Therefore, we assume constant-volume deformation.

Table 3. *Finite strain data*

Sample/ Method	Stretches			Axial Ratios		
	S_X	S_Y	S_Z	R_{XY}	R_{YZ}	R_{XZ}
S1 R_f/Φ	1.57	1.14	0.60	1.38	1.90	2.62
S2 R_f/Φ	1.64	1.29	0.57	1.27	2.26	2.88
S2 Fry	1.77	1.21	0.61	1.46	1.98	2.90
S3 R_f/Φ	2.41	1.10	0.52	2.19	2.12	4.63
S3 Fry	2.33	1.20	0.48	1.94	2.50	4.85
S4 R_f/Φ	5.41	1.20	0.41	4.51	2.93	13.20
S5 R_f/Φ	3.96	1.34	0.37	2.96	3.62	10.70
S6 R_f/Φ	2.77	1.02	0.41	2.72	2.49	6.76
S6 Fry	2.77	0.94	0.48	2.95	1.96	5.77
S7 R_f/Φ	4.19	1.13	0.50	3.71	2.26	8.38
S8 R_f/Φ	7.17	1.25	0.36	5.74	3.47	19.92
S9 R_f/Φ	1.19	1.17	0.49	1.02	2.39	2.43
S10 R_f/Φ	2.67	1.19	0.31	2.24	3.76	8.42
S11 R_f/Φ	1.80	1.52	0.37	1.19	4.15	4.94
S12 R_f/Φ	1.95	1.57	0.33	1.24	4.79	5.94
S13 R_f/Φ	2.04	1.37	0.36	1.49	3.79	5.67
S14 R_f/Φ	1.69	1.58	0.38	1.07	4.21	4.50

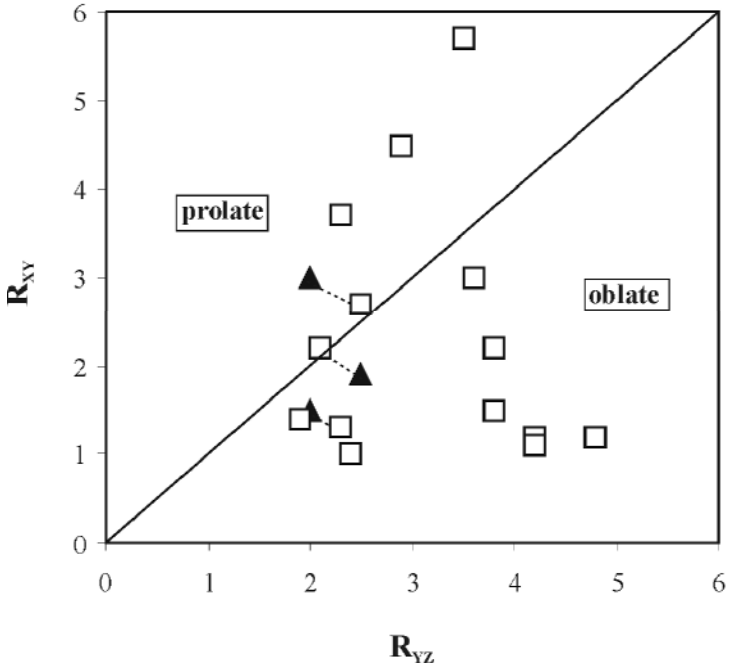

Fig. 11. Flinn diagram (Flinn 1962) showing strain symmetry as obtained by R_f/ϕ (white squares) and Fry (black triangles) analysis; R_f/ϕ and Fry data from the same sample are connected by dashed tie lines.

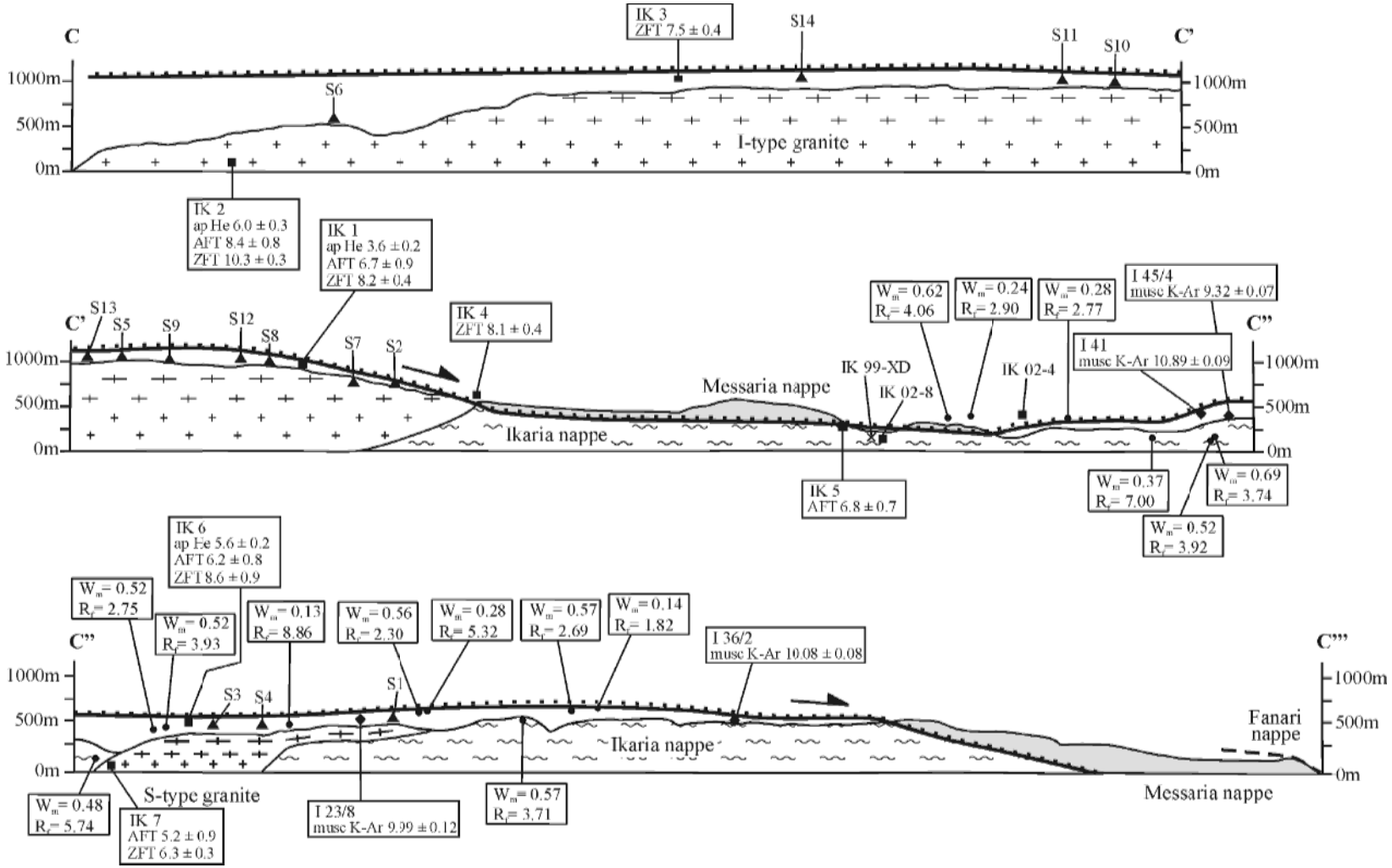

Fig. 12. Simplified cross-section C-C'-C''-C''' of Ikaria Island. The outcrops where the vein analyses were carried out have been projected in the profile plane; both the kinematic vorticity number (W_m) and the strain ratio (R_f) of deformed pegmatite veins are shown for the analyzed samples; the sample locations with the different ages of the low-temperature thermochronology (ap He = apatite (U-Th)/He, AFT = apatite fission track and ZFT = zircon fission track), of the $^{87}Rb/^{86}Sr$ data, of the $^{40}Ar/^{39}Ar$ data, the location of the data of Altherr et al. (1982), the samples of the P-T estimates and of the finite strain analyses are also shown; the dashed black line shows Fanari detachment and the black solid line shows the Messaria detachment.

Deformed vein sets

We analyzed fifteen outcrop surfaces, thirteen in metapelite of the Ikaria nappe and two in phyllite of the Messaria nappe (Fig. 2). The distribution of the deformed veins has an asymmetric distribution of vein sectors (Fig. 13a) that is consistent with top-to-the-NNE shear. The results are plotted in a Mohr diagram for H (Fig. 13b, c); W_m, R_f and A (Table 4) are calculated from the Mohr circle parameters. W_m ranges from 0.13 to 0.69 and R_f from 1.8 to 8.9 (Fig. 12). In general, R_f agrees with values of 2.4 to 19.9 for R_{XZ} of finite-strain analysis and again demonstrate heterogeneous shortening perpendicular to the shear zone (Fig. 12). The data for A indicate an area change ranging from –0.54 to +0.31 with ten samples showing area decrease and the other five area increase in the XZ section.

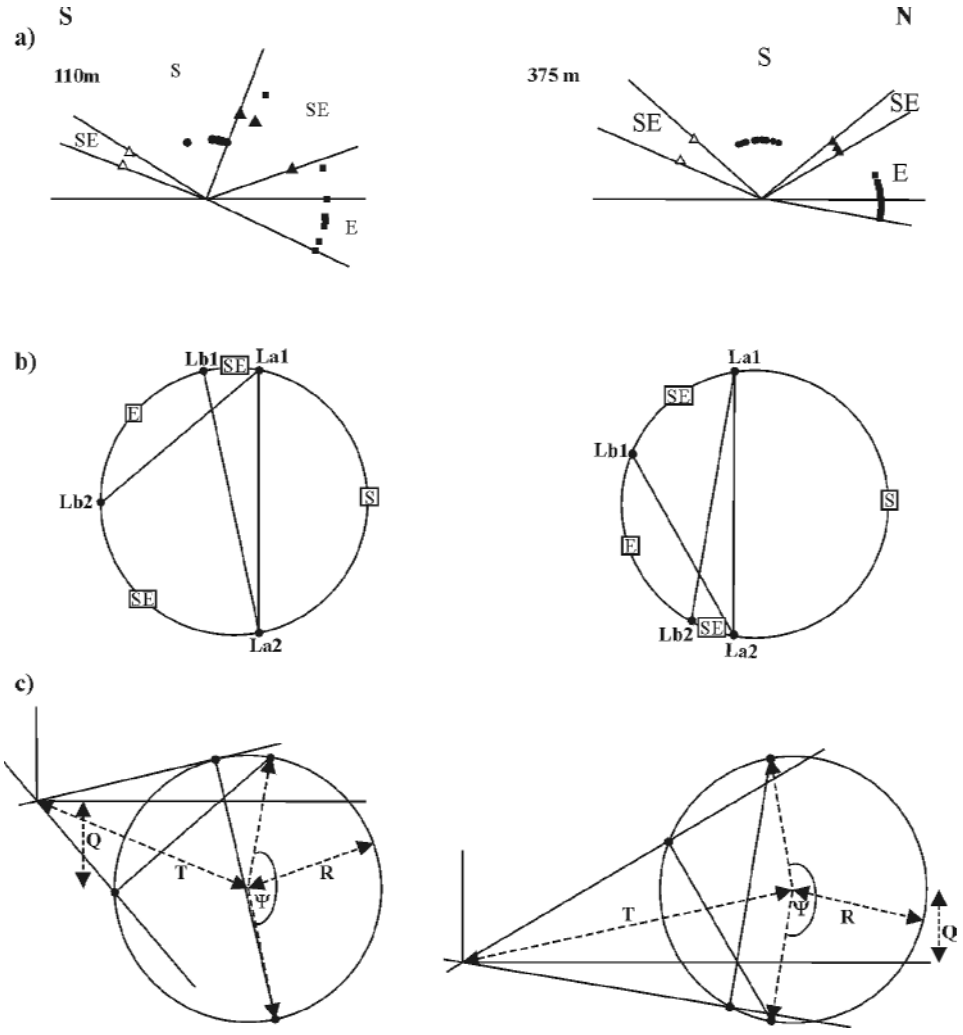

Fig. 13. (a) Results of sector calculation for two samples (vein110 and vein375) plotted in a Mohr diagram for H so that line connecting La_1 and La_2 is vertical (see Passchier 1990 for details). (b) Mohr circle for H representing the finite deformation in stretch space. The size and position of the circle can be defined by three parameters: the distance of the centre of the circle from the origin (T), the radius of the circle (R) and the distance of the centre of the circle from the horizontal axis (Q). W_m, R_f and A. (c) Distribution of deformed pegmatite veins. Black dots = shortened veins, blacktriangles = shortened and extended veins and crosses = extended veins.

Table 5. *Kinematic data of pegmatite veins*

Sample	Latitude Longitude	W_m	R_f	A
vein5	N 37°37'31" E 26°11'13"	0.30	4.45	-0.22
vein30	N 37°37'43" E 26°12'19"	0.28	2.77	-0.12
vein55	N 37°37'56" E 26°12'52"	0.52	3.92	0.05
vein100	N 37°38'07" E 26°13'40"	0.48	5.74	-0.26
vein105	N 37°37'57" E 26°12'33"	0.37	7.00	-0.34
vein110	N 37°38'01" E 26°13'11"	0.69	3.74	0.19
vein130	N 37°38'22" E 26°13'59"	0.52	2.75	0.31
vein180	N 37°38'17" E 26°14'01"	0.52	3.93	0.10
vein305	N 37°38'14" E 26°15'26"	0.13	8.86	0.14
vein350	N 37°38'40" E 26°15'49"	0.28	5.32	-0.14
vein375	N 37°38'44" E 26°15'24"	0.56	2.30	-0.16
vein400	N 37°37'44" E 26°10'56"	0.62	4.06	-0.37
vein500	N 37°38'55" E 26°16'39"	0.57	3.71	-0.26
vein560	N 37°39'14" E 26°16'57"	0.14	1.82	-0.54
vein680	N 37°39'04" E 26°16'58"	0.57	2.69	-0.26

Blocked-object analysis

In general, the finite-strain data in conjunction with the chemical data indicate flattening strain type, which suggests that deformation deviated from simple shear. To quantify the degree of non-coaxiality, we carried out a flow-path analysis. Most granite samples were not suitable for this analysis because the feldspar grains are too closely packed and could not rotate freely in the rock during deformation. Only a few samples were used for the rotation analysis (Fig. 2).

In the diagrams shown in Figure 14, a distinction can be made between measurements of relatively low aspect ratio that scatter across a wide range of orientations and those with higher aspect ratio, which have a more restricted range of orientations. The critical values for R in the granites show a wide scatter and range from ~1.3 to ~3.0. These values are interpreted as the critical values for R_C separating porphyroclasts that rotated freely from those which have attained a stable position during deformation. Accordingly, W_m ranges from

0.26 to 0.80. These values are in accord with flattening strain type and with W_m of 0.13 to 0.69 as obtained from the deformed vein sets. The data indicate vertical shortening normal to the mylonitic foliation in the granites. Furthermore, the huge spread in W_m again reflects heterogeneous strain during extension.

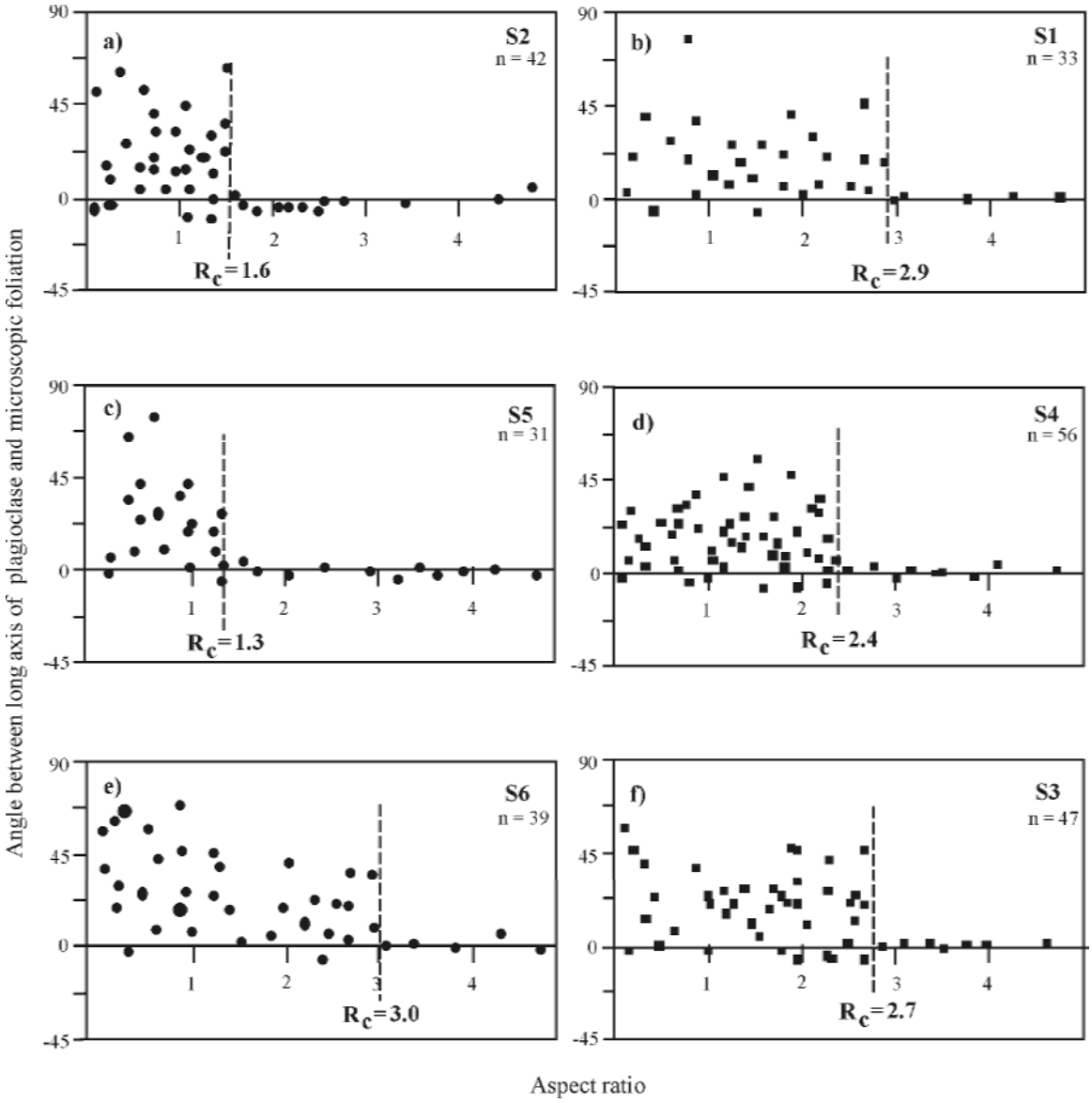

Fig. 14. Diagrams in which aspect ratios are plotted against rotation angles of feldspar grains in the granite. The dashed lines define the critical aspect ratios (R_c) which divide objects whose long axes reached a stable position subparallel to the foliation and those with lower aspect ratios that did not find a stable position and thus show a large scatter in readings.

Geochronology

$^{86}Rb/^{87}Sr$ data

Both samples are characterized by isotopic disequilibria. Detailed thin-section investigation of the quartzitic schist (sample IK 99XD) suggests complete synkinematic recrystallization; however, internal isotopic equilibrium on the mineral scale has not been achieved. On an isochron plot, the data only allow calculation of a loosely defined reference line corresponding to an age of 12.9 ± 3.5 Ma (Fig. 15, Table 5). As no alteration features are observed, disequilibria are likely to correspond to preservation of isotopic relics. The age value is therefore interpreted as a maximum age for the last stages of mylonitization.

The metapegmatite sample IK 02-4 shows severe Sr-isotopic disequilibria even for the strongly deformed domains. For all analyzed white mica fractions, apparent ages have been calculated using the isotopic signature of apatite for reference. There is a clear correlation between sieve fraction (as a proxy for grain size) and apparent age for white mica separates (Table 5). While the apparent age of 58 ± 1 Ma for the 250-160 µm sieve fraction can be interpreted as a maximum age for deformation, the apparent age of 375 ± 6 Ma for the 500-355 µm fraction points to only limited Sr isotope exchange among dynamically recrystallizing phases and/or to presence of ground, but not recrystallized primary, pegmatitic white mica. The apparent ages for slightly bent and kinked mica fish inner domains of 417 ± 6 and 458 ± 7 Ma are "mixed" ages as well, without direct geological meaning. However, 458 ± 7 Ma is a minimum age for protolith crystallization.

Table 5. *$^{87}Rb/^{86}Sr$ analytical data*

Sample/ Analysis No.	material	Rb (ppm)	Sr (ppm)	$^{87}Rb/^{86}Sr$	$^{87}Sr/^{86}Sr$	$^{87}Sr/^{86}Sr$ $2\sigma_m$(%)	apparent age (Ma)
IK 99XD (Quartzitic schist) Reference line: 12.9 ± 3.5 Ma; MSWD = 527							
PS1000	white mica 125-100 µm	220.6	95.19	6.712	0.717704	0.0018	
PS1002	quartz-feldspar	53.28	148.01	1.042	0.716825	0.0014	
PS1004	apatite	0.63	329.25	0.006	0.715842	0.0016	
PS1006	white mica 160-125 µm	301	19.46	44.82	0.724456	0.0014	
IK 02-4 (Meta-Pegmatite)							
PS966	apatite	9.9	3119	0.009	0.762616	0.0014	
PS967	feldspar yellow	36.98	190.9	0.564	0.769208	0.0018	
PS968	quartz-feldspar	89.96	105.4	2.485	0.770885	0.0014	
PS971	white mica 250-160 µm	414.6	15.04	80.69	0.828981	0.0014	58 ± 1
PS969	white mica 355-250 µm	615.8	11.48	165.9	1.412026	0.0018	275 ± 4
PS970	white mica 500-355 µm	755.1	7.84	327.7	2.512574	0.0010	375 ± 6
PS1072	prim. white mica, ~4 mm	883.6	4.93	778.6	5.840034	0.0014	458 ± 7
PS1073	prim. white mica, ~3 mm	828.2	4.57	756.9	5.257868	0.0016	417 ± 6

Errors are reported at the 2 σ level. An uncertainty of ± 1.5% has to be assigned to Rb/Sr ratios. Prim.: primary pegmatitic. Apparent ages are calculated using the isotopic signature of apatite (see text for details).

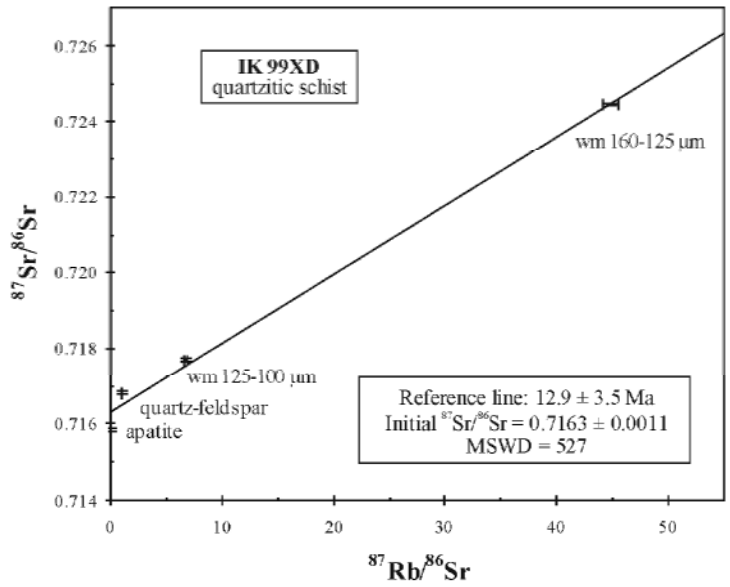

Fig. 15. $^{87}Rb/^{86}Sr$ data of sample IK 99XD. Data combine to a loosely defined reference line yielding an age of 12.9 ± 3.5 Ma.

$^{40}Ar/^{39}Ar$ data

White mica from samples IK 02-4 and IK 02-8 were dated. The chemical data indicate that white mica in the samples are phengite. (Table 6a, Fig. 16). The Si content of the phengite is between 3.03 and 3.15 per formula unit (pfu) for IK 02-4 and between 3.00 and 3.30 pfu for IK 02-8. The content of Al_{tot} is decreasing with increasing Si content. The Fe^{3+} content of phengite is low, as it plots along the celadonite/muscovite tie-line (Fig. 16). In correspondence with high Si content, the amount of Na^{+} is low.

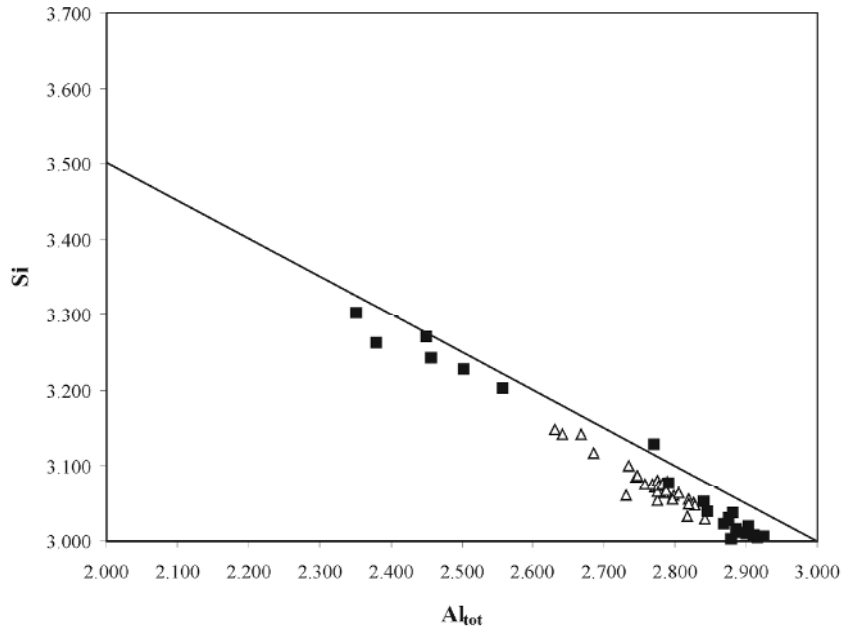

Fig. 16. Si versus Al_{tot} (pfu) in phengite indicating a low content of Fe^{3+}. The line is demonstrating the celadonite/muscovite tie-line. The white triangles are representing the phengite of sample IK 02-4 and the black squares the phengite of sample IK 02-8.

In each sections between 6 and 10 spots were analyzed. The ages of IK 02-4 rang from 13.8 ± 4.8 to 5.4 ± 1.8 Ma and have a weighted mean age of 10.8 ± 1.1 Ma. The ages from IK 02-8 rang from 11.1 ± 0.3 to 9.5 ± 0.5 Ma and show a weighted mean age of 10.5 ± 2.4 Ma (Table 6b). The absolute frequency of the different ages (per section) is represented in histograms (Fig. 17). The phengite ages date ductile deformation in the Messaria shear zone.

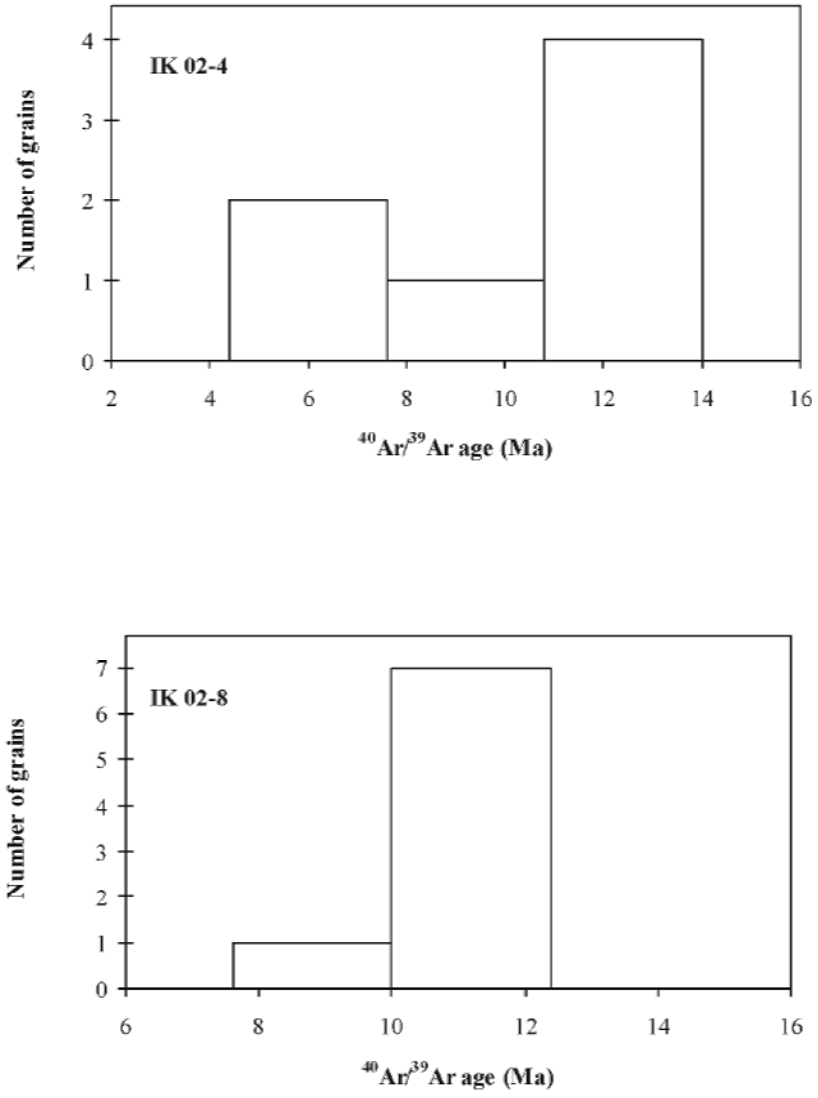

Fig. 17. $^{40}Ar/^{39}Ar$ spot fusion analyses. The absolute frequency of ages in the sections of samples IK 02-4 and IK 02-8 are represented in histograms.

Table 6a. *White mica analyses*

IK 02-4																										
SiO_2	45.890	45.530	45.630	45.450	43.850	45.300	46.620	45.430	45.550	46.890	45.500	45.470	44.970	45.380	45.410	45.160	46.060	45.920	45.490	46.810	45.570	46.130	44.880	46.130	45.890	47.060
$Al2O_3$	34.640	35.310	34.920	35.570	33.810	35.690	33.600	35.700	34.650	33.250	35.070	34.960	35.790	35.730	34.860	35.070	34.460	35.290	35.690	34.220	35.390	35.230	33.980	34.830	35.070	33.560
TiO_2	0.051	0.108	0.194	0.063	0.098	0.188	0.043	0.084	0.114	0.034	0.052	0.074	0.035	0.025	0.044	0.088	0.180	0.052	0.081	0.260	0.068	0.065	0.067	0.017	0.035	0.057
Cr_2O_3	0.099	0.020	0.079	0.085	0.019	0.027	0.058	0.025	0.064	0.013	0.051	0.014	0.028	0.050	0.010	0.041	0.013	0.050	0.052	0.051	0.010	0.082	0.029	0.033	0.000	0.000
MgO	0.949	0.734	0.767	0.685	0.676	0.794	0.846	0.635	0.938	1.394	0.888	0.876	0.711	0.769	0.905	0.585	0.883	0.681	0.680	1.039	0.645	0.716	0.864	1.001	0.816	1.321
FeO	1.910	1.730	1.620	1.420	2.770	1.740	2.090	1.600	1.720	1.780	1.980	1.880	1.650	1.490	2.010	1.420	1.640	1.700	1.610	1.980	1.990	1.920	3.220	1.780	1.970	1.900
MnO	0.068	0.022	0.027	0.085	0.000	0.083	0.036	0.051	0.107	0.045	0.014	0.064	0.000	0.000	0.040	0.000	0.068	0.017	0.026	0.098	0.016	0.091	0.049	0.000	0.065	0.014
CaO	0.045	0.000	0.000	0.000	0.047	0.000	0.000	0.000	0.000	0.000	0.000	0.000	0.000	0.000	0.008	0.036	0.000	0.000	0.020	0.000	0.000	0.000	0.012	0.013	0.000	0.000
BaO	0.000	0.023	0.192	0.067	0.000	0.025	0.000	0.012	0.000	0.150	0.064	0.000	0.000	0.130	0.084	0.028	0.158	0.128	0.008	0.000	0.218	0.124	0.147	0.252	0.000	0.000
Na_2O	0.382	0.357	0.340	0.407	0.260	0.313	0.428	0.373	0.317	0.332	0.428	0.453	0.468	0.478	0.386	0.324	0.318	0.234	0.502	0.328	0.423	0.539	0.407	0.403	0.399	0.405
K_2O	10.760	11.020	11.100	10.850	10.450	10.870	10.790	10.750	10.890	10.940	10.620	10.780	10.920	10.700	10.800	10.990	10.920	10.900	10.930	10.940	10.860	10.850	10.700	10.780	10.430	10.760
Total	94.794	94.854	94.869	94.682	91.980	95.030	94.511	94.660	94.350	94.828	94.667	94.571	94.572	94.752	94.557	93.742	94.700	94.972	95.089	95.726	95.190	95.747	94.355	95.239	94.675	95.077
Si^{4+}	3.086	3.061	3.072	3.056	3.054	3.033	3.142	3.051	3.076	3.149	3.064	3.066	3.030	3.048	3.067	3.065	3.101	3.079	3.049	3.118	3.056	3.076	3.061	3.088	3.081	3.143
Al^{IV}	0.914	0.939	0.928	0.944	0.946	0.967	0.858	0.949	0.924	0.851	0.936	0.934	0.970	0.952	0.933	0.935	0.899	0.921	0.951	0.882	0.944	0.924	0.939	0.912	0.919	0.857
Al^{VI}	1.832	1.859	1.843	1.874	1.829	1.850	1.810	1.876	1.833	1.780	1.848	1.843	1.872	1.877	1.841	1.869	1.835	1.867	1.868	1.804	1.853	1.844	1.792	1.835	1.855	1.784
Ti^{4+}	0.003	0.005	0.010	0.003	0.005	0.009	0.002	0.004	0.006	0.002	0.003	0.004	0.002	0.001	0.002	0.004	0.009	0.003	0.004	0.013	0.003	0.003	0.003	0.001	0.002	0.003
Cr^{3+}	0.005	0.001	0.004	0.005	0.001	0.001	0.003	0.001	0.003	0.001	0.003	0.001	0.001	0.003	0.001	0.002	0.001	0.003	0.003	0.003	0.001	0.004	0.002	0.002	0.000	0.000
Mg^{2+}	0.095	0.074	0.077	0.069	0.070	0.079	0.085	0.064	0.094	0.140	0.089	0.088	0.071	0.077	0.091	0.059	0.089	0.068	0.068	0.103	0.064	0.071	0.088	0.100	0.082	0.132
Fe^{2+}	0.107	0.097	0.091	0.080	0.161	0.097	0.118	0.090	0.097	0.100	0.111	0.106	0.093	0.084	0.114	0.081	0.092	0.095	0.090	0.110	0.112	0.107	0.184	0.100	0.111	0.106
Mn^{2+}	0.004	0.001	0.002	0.005	0.000	0.005	0.002	0.003	0.006	0.003	0.001	0.004	0.000	0.000	0.002	0.000	0.004	0.001	0.001	0.006	0.001	0.005	0.003	0.000	0.004	0.001
Ca^{2+}	0.003	0.000	0.000	0.000	0.004	0.000	0.000	0.000	0.000	0.000	0.000	0.000	0.000	0.000	0.001	0.003	0.000	0.000	0.001	0.000	0.000	0.000	0.001	0.001	0.000	0.000
Ba^{2+}	0.000	0.001	0.005	0.002	0.000	0.001	0.000	0.000	0.000	0.004	0.002	0.000	0.000	0.003	0.002	0.001	0.004	0.003	0.000	0.000	0.006	0.003	0.004	0.007	0.000	0.000
Na^{+}	0.050	0.047	0.044	0.053	0.035	0.041	0.056	0.049	0.042	0.043	0.056	0.059	0.061	0.062	0.051	0.043	0.042	0.030	0.065	0.042	0.055	0.070	0.054	0.052	0.052	0.052
K^{+}	0.923	0.945	0.953	0.931	0.928	0.928	0.927	0.921	0.938	0.937	0.912	0.927	0.939	0.917	0.930	0.951	0.938	0.932	0.934	0.929	0.929	0.923	0.931	0.920	0.893	0.917
Total	7.022	7.030	7.029	7.021	7.037	7.053	7.021	7.025	7.037	7.039	7.024	7.038	7.053	7.024	7.034	7.035	7.013	7.006	7.036	7.011	7.044	7.031	7.061	7.028	7.008	7.043

Table 6a. W*hite mica analyses*

IK 02-8																							
SiO_2	45.940	49.120	45.590	45.740	45.060	45.120	45.010	45.380	48.970	48.000	48.310	46.000	45.280	48.850	45.060	45.200	45.150	45.040	45.520	47.010	44.990	45.850	48.320	45.400
$Al2O_3$	35.340	29.670	36.690	36.810	36.250	37.780	37.150	36.840	31.120	32.520	31.770	36.530	37.010	30.230	37.220	37.220	36.850	36.970	36.670	35.300	36.590	36.190	31.060	36.920
TiO_2	0.268	0.315	0.328	0.351	0.251	0.230	0.120	0.361	0.247	0.131	0.181	0.468	0.357	0.439	0.422	0.121	0.233	0.261	0.228	0.208	0.450	0.115	0.162	0.410
Cr_2O_3	0.019	0.090	0.060	0.060	0.101	0.053	0.075	0.041	0.029	0.125	0.074	0.086	0.060	0.060	0.089	0.148	0.078	0.000	0.030	0.040	0.080	0.130	0.080	0.064
MgO	0.822	2.520	0.490	0.502	0.441	0.415	0.327	0.483	1.960	1.770	2.040	0.550	0.479	2.560	0.397	0.487	0.495	0.493	0.713	0.501	0.546	0.761	2.240	0.529
FeO	0.891	2.160	0.910	0.757	0.738	0.804	0.809	0.930	1.510	1.284	1.770	1.133	0.871	2.110	1.051	0.979	0.741	0.821	1.136	0.788	0.786	0.829	2.060	0.979
MnO	0.036	0.038	0.019	0.019	0.008	0.000	0.000	0.000	0.000	0.000	0.000	0.000	0.000	0.012	0.015	0.000	0.026	0.048	0.000	0.000	0.039	0.000	0.000	0.000
CaO	0.000	0.000	0.000	0.000	0.000	0.021	0.000	0.000	0.000	0.000	0.000	0.000	0.000	0.000	0.000	0.000	0.013	0.000	0.018	0.010	0.000	0.000	0.000	0.000
BaO	0.482	0.046	0.254	0.289	0.265	0.353	0.345	0.276	0.449	0.343	0.216	0.131	0.121	0.178	0.237	0.037	0.195	0.000	0.381	0.208	0.393	0.431	0.046	0.342
Na_2O	1.104	0.665	1.380	1.296	1.290	1.325	1.580	1.380	0.651	0.827	0.781	1.243	1.287	0.663	1.291	1.460	1.370	1.303	1.301	1.250	1.332	1.095	0.784	1.327
K_2O	9.660	9.370	9.440	9.330	9.060	8.960	9.150	9.520	9.520	9.600	9.590	9.340	9.580	9.820	9.300	9.270	9.120	9.360	8.890	9.040	9.420	9.660	9.670	9.170
Total	94.562	93.994	95.161	95.154	93.464	95.061	94.566	95.211	94.456	94.600	94.732	95.481	95.045	94.922	95.082	94.922	94.271	94.296	94.887	94.355	94.626	95.061	94.422	95.141
Si^{4+}	3.077	3.303	3.024	3.032	3.038	2.989	3.006	3.016	3.271	3.203	3.228	3.040	3.011	3.262	2.993	3.005	3.019	3.008	3.028	3.129	3.003	3.053	3.242	3.012
Al^{IV}	0.923	0.697	0.976	0.968	0.962	1.011	0.994	0.984	0.729	0.797	0.772	0.960	0.989	0.738	1.007	0.995	0.981	0.992	0.972	0.871	0.997	0.947	0.758	0.988
Al^{VI}	1.867	1.654	1.892	1.908	1.919	1.938	1.930	1.902	1.721	1.760	1.730	1.884	1.910	1.641	1.907	1.922	1.923	1.918	1.902	1.898	1.881	1.892	1.699	1.899
Ti^{4+}	0.014	0.016	0.016	0.017	0.013	0.011	0.006	0.018	0.012	0.007	0.009	0.023	0.018	0.022	0.021	0.006	0.012	0.013	0.011	0.010	0.023	0.006	0.008	0.020
Cr^{3+}	0.001	0.005	0.003	0.003	0.005	0.003	0.004	0.002	0.002	0.007	0.004	0.004	0.003	0.003	0.005	0.008	0.004	0.000	0.002	0.002	0.004	0.007	0.004	0.003
Mg^{2+}	0.082	0.253	0.048	0.050	0.044	0.041	0.033	0.048	0.195	0.176	0.203	0.054	0.047	0.255	0.039	0.048	0.049	0.049	0.071	0.050	0.054	0.076	0.224	0.052
Fe^{2+}	0.050	0.121	0.050	0.042	0.042	0.045	0.045	0.052	0.084	0.072	0.099	0.063	0.048	0.118	0.058	0.054	0.041	0.046	0.063	0.044	0.044	0.046	0.116	0.054
Mn^{2+}	0.002	0.002	0.001	0.001	0.000	0.000	0.000	0.000	0.000	0.000	0.000	0.000	0.000	0.001	0.001	0.000	0.001	0.003	0.000	0.000	0.002	0.000	0.000	0.000
Ca^{2+}	0.000	0.000	0.000	0.000	0.000	0.001	0.000	0.000	0.000	0.000	0.000	0.000	0.000	0.000	0.000	0.000	0.001	0.000	0.001	0.001	0.000	0.000	0.000	0.000
Ba^{2+}	0.013	0.001	0.007	0.008	0.007	0.009	0.009	0.007	0.012	0.009	0.006	0.003	0.003	0.005	0.006	0.001	0.005	0.000	0.010	0.005	0.010	0.011	0.001	0.009
Na^{+}	0.143	0.087	0.178	0.167	0.169	0.170	0.205	0.178	0.084	0.107	0.101	0.159	0.166	0.086	0.166	0.188	0.178	0.169	0.168	0.161	0.172	0.141	0.102	0.171
K^{+}	0.825	0.804	0.799	0.789	0.779	0.757	0.779	0.807	0.811	0.817	0.817	0.787	0.812	0.836	0.788	0.786	0.778	0.797	0.754	0.768	0.802	0.820	0.828	0.776
Total	6.998	6.954	7.031	6.994	6.982	7.000	7.022	7.014	6.955	6.988	6.969	6.993	7.010	7.006	7.015	7.014	6.993	7.018	6.986	6.939	7.047	6.999	6.987	7.007

Table. 6b. $^{40}Ar/^{39}Ar$ analytical data (sections; spot fusion)

Sample	Latitude Longitude	Mineral No.	$^{40}Ar^*/^{39}Ar$	$^{36}Ar/^{40}Ar$ x 1000 J = 0.013337	$^{39}Ar/^{40}Ar$	$^{37}Ar/^{39}Ar$	% Atm	Age Ma	error 1σ
IK 02-4	37°34'51"	1	0.554	1.124	1.2038	0.003	33.2	13.3	1.6
	26°10'04"	2	0.224	1.999	1.8211	0.025	59	5.4	1.8
		3	0.303	1.751	1.5915	0.068	51.7	7.3	1.9
		4	0.509	1.692	0.9803	0	50	12.2	2.3
		5	0.575	0.279	1.5926	0.088	8.2	13.8	4.8
		6	0.438	0.753	1.7719	0.051	22.2	10.5	0.8
		7	0.549	0.655	1.4663	0.101	19.3	13.2	4.3
								10.8	**1.1**
IK 02-8	37°34'51"	1	0.443	1.724	1.1063	0.036	50.9	10.6	3.6
	26°10'04"	2	0.456	1.346	1.3198	0.017	39.7	10.9	2
		3	0.448	1.347	1.3426	0.012	39.8	10.8	1.3
		4	0.435	1.352	1.3792	0.021	39.9	10.4	0.4
		5	0.422	1.272	1.4764	0.02	37.6	10.1	0.5
		6	0.396	1.501	1.4035	0.006	44.3	9.5	0.5
		7	0.461	1.25	1.3657	0.012	36.9	11.1	0.3
		8	0.452	1.381	1.3077	0.032	40.8	10.9	0.2
								10.5	**2.4**

Low-temperature thermochronology

The zircon fission track ages from the footwall of the Messaria extensional fault system range from 10.3 ± 0.3 Ma in the south to 6.3 ± 0.3 in the north (weighted mean age of 8.1 ± 0.2 Ma). The apatite fission track ages are between 8.4 ± 0.8 Ma (south) and 5.2 ± 0.9 (north) (weighted mean age of 6.6 ± 0.3 Ma) and the apatite (U-Th)/He ages range from 6.0 ± 0.3 Ma (south) to 3.6 ± 0.2 (north) (weighted mean age of 5.0 ± 0.1 Ma) (Table 7). All ages consistently young in a northward direction. Altherr et al. (1982) reported K-Ar and Rb-Sr muscovite ages of 11-10 Ma and K-Ar and Rb-Sr biotite ages of 11-8 Ma for the footwall of the Messaria extensional fault system, which are also younging from the south to the north.

The samples from the hangingwall of the Messaria extensional fault system yielded no apatite and zircon. Fission track ages form the Ampelos nappe of Samos, which is correlative with the Messaria nappe in the hangingwall of the Messaria extensional fault system, range from 20-18 Ma (Fig. 4, Table 7).

Temperature-time (T-t) paths for the I-type granite and for the metasediments (Fig. 18) in the footwall of the Messaria extensional fault system have been calculated. The data for both rock units indicate rapid cooling from ~300°C to ~80°C within <4 Ma at average rates of ~50°C

Myr^{-1} for the I-type granite and ~60°C Myr^{-1} for the metasediments of the Ikaria nappe. The mean track lengths in the apatite range from 14.14 ± 0.16 μm to 14.18 ± 0.12 μm for the I-type granite and 14.43 ± 0.21 μm to 14.51 ± 0.19 μm for the metasediments (Table 7) and support rapid cooling.

The cooling curves for the I-type granite and the metasediments of the Ikaria nappe are different (Fig. 18). We envisage that the T-t path for the Ikaria nappe reflects extension-related cooling during and after greenschist-facies metamorphism and that the relatively constant cooling rate is controlled by a constant rate of extensional slip. The I-type granite intruded synkinematically into the Messaria extensional fault system and its intrusion temperature was higher than temperatures for greenschist-facies metamorphism in the Ikaria nappe. Therefore, the I-type granite had more potential for initially fast cooling, which is reflected by the steep cooling curve between the zircon and apatite PAZ's (Fig. 18). After fast tectonically-controlled cooling from intrusion temperatures, the I-type granite had a similar cooling history as its country rocks.

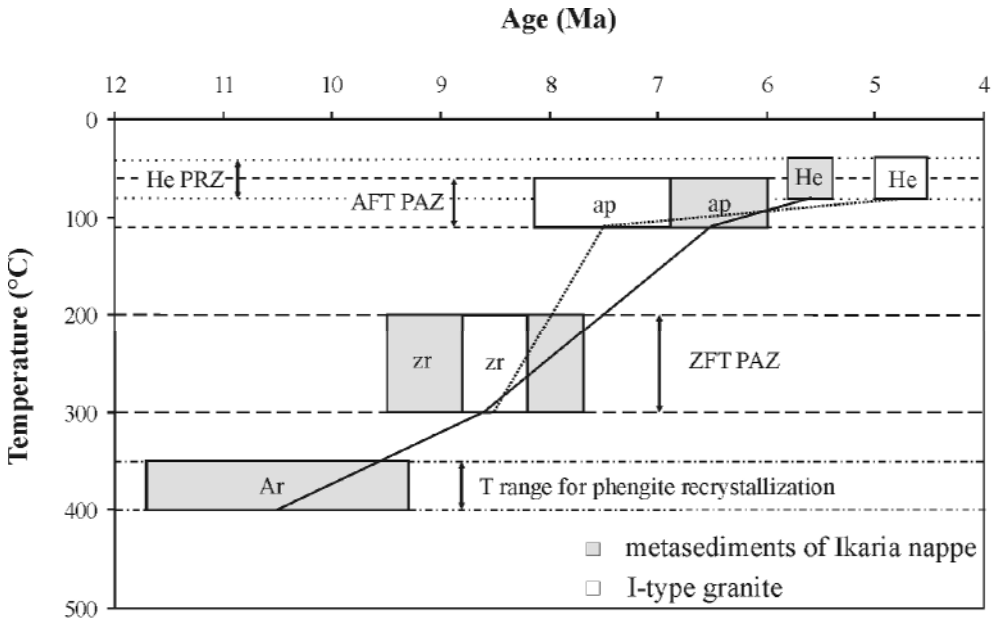

Fig. 18. T-t diagram showing cooling rates for the footwall of the Messaria extensional fault system. Shown is the T-t path (dotted black line) for the I-type granite as derived from the means of the fission track (8.5 ± 0.2 Ma for zircon and 7.5 ± 0.6 Ma for apatite) and (U-Th)/He ages (4.8 ± 0.2 Ma) of samples IK 1 to IK 4 (white boxes). The black line shows the T-t path for metasediments of the Ikaria nappe; in addition to the means of the fission track (7.4 ± 0.5 Ma for zircon and 6.0 ± 0.5 Ma for apatite) and (U-Th)/He ages (5.6 ± 0.2 Ma) of samples IK 5 and IK 6 (light grey boxes), the mean of 10.5 ± 1.2 Ma as obtained from the K-Ar muscovite ages of samples I 45/4, I 23/8, I 41 and I 36/2 from Altherr et al. (1982) and the $^{40}Ar/^{39}Ar$ ages of samples IK 02-4 and IK 02-8 (light grey boxes) are shown. He PRZ = partial retention zone of the helium in apatite (~80-40°C), AFT PAZ = apatite partial annealing zone of fission tracks (~110-60°C) and ZFT PAZ = zircon partial annealing zone of fission tracks (~300-200°C).

Table 7. *Apatite and zircon fission-track and apatite (U-Th)/He data from the islands of Ikaria (IK) and Samos (Sa)*

Sample	Latitude Longitude	Mineral type	Number of grains	Standard track density (x106 cm-2)	Fossil track density (x105 cm-2)	Induced track density (x106 cm-2)	Chi square probability (%)	Uranium (ppm)	Fission track age (Ma ± 1ó)	Mean track length (µm)	Standard deviation (± 1ó µm)	Number of tracks measured	Helium (nmol/g)	Uranium (ppm)	Thorium (ppm)	Helium age (Ma ± 1ó)
IK 1	37°38'02"	apatite	17	1.3077	1.392	4.517	93.5	43.2	6.7 ± 0.9	14.14 ± 0.16	0.87	28	0.483	28.51	30.75	3.6 ± 0.2
	26°05'09"			13389	60	1947										
		zircon	15	0.386	27.64	8.15	8.4	774.9	8.2 ± 0.4	-	-	-	-	-	-	-
				5206	1252	3692										
IK 2	37°31'11"	apatite	22	1.3285	1.477	3.865	98.3	36.4	8.4 ± 0.8	14.18 ± 0.12	0.9	52	1.38	50.63	49.97	6.0 ± 0.3
	26°00'49"			13389	117	3061										
		zircon	16	0.3593	37.36	8.264	37.3	844.2	10.3 ± 0.3	-	-	-	-	-	-	-
				5206	1954	4322										
IK 3	37°33'21"	zircon	10	0.334	18.15	5.121	57.0	562.7	7.5 ± 0.4	-	-	-	-	-	-	-
	26°02'51"			4448	450	1270										
IK 4	37°36'49"	zircon	7	0.3265	17.94	4.539	32.4	510.2	8.1 ± 0.4	-	-	-	-	-	-	-
	26°09'07"			4448	739	1870										
IK 5	37°35'09"	apatite	24	1.227	1.265	3.808	96.7	38.8	6.8 ± 0.7	14.43 ± 0.21	1.02	23	-	-	-	-
	26°12'13"			12088	104	3130										
IK 6	37°38'31"	apatite	19	1.2179	0.7226	2.374	95.5	24.4	6.2 ± 0.8	14.51 ± 0.19	1.12	35	0.26	12.08	1.32	5.6 ± 0.2
	26°14'26"			12088	56	1840										
		zircon	3	0.307	13.78	3.111	95.1	371.9	8.6 ± 0.9	-	-	-	-	-	-	-
				4448	124	280										
IK 7	37°35'44"	apatite	16	1.1906	0.4444	1.691	93.8	17.8	5.2 ± 0.9	14.19 ± 0.18	0.93	26	-	-	-	-
	26°15'22"			12088	36	1370										
		zircon	12	0.294	16.71	4.94	100	616.6	6.3 ± 0.3	-	-	-	-	-	-	-
				4448	695	2055										
Sa 2	37°40'36"	zircon	12	0.3	27.55	2.582	72.2	315.9	20.3 ± 0.9	-	-	-	-	-	-	-
	26°48'16"			3836	1102	1033										
Sa 4	37°46'58"	zircon	16	0.291	40.97	3.928	98.5	495.4	19.3 ± 0.7	-	-	-	-	-	-	-
	26°51'19"			3836	2110	2023										
Sa 5	37°45'59"	zircon	12	0.286	36.04	3.611	99.5	463.4	18.1 ± 0.8	-	-	-	-	-	-	-
	26°57'35"			3836	1038	1040										
Sa 7	37°43'48"	zircon	7	0.2629	42.05	9.603	96.3	1340.5	7.3 ± 0.5	-	-	-	-	-	-	-
	26°34'06"			3836	328	749										
Sa 9	37°42'52"	zircon	12	0.245	36.24	4.003	99.6	599.7	14.1 ± 0.6	-	-	-	-	-	-	-
	26°38'17"			3836	1080	1193										

Apatite and zircon FT ages have been calculated using zeta factors of 127.3 ± 4.4 and 332.9 ± 9.7 determined by multiple analyses of standards following the recommendations of Hurford (1990). Central ages are reported. All ages are quoted at the 1 ó level.

Tectonic significance of geochronological results

Slip rate for Messaria extensional fault system

The decrease of the zircon and apatite fission track and apatite (U-Th)/He ages in a direction parallel to hangingwall transport on the Messaria extensional fault system reflects the progressive southward migration of footwall exhumation and are related to the lateral passage of subhorizontal isotherms at the top of the footwall. Hence, the data can be used to estimate slip rates (see Foster & John 1999) for the Messaria extensional fault system from the inverse slope of mineral age with distance in the slip direction (Foster et al. 1993).

In Figure 19, samples IK 1 - IK 4 from the I-type granite in the western part of the island are plotted along cross section D-D' and yielded slip rates of 6.0 ± 0.9 km Myr^{-1} (apatite (U-Th)/He), 8.4 ± 6.0 km Myr^{-1} (apatite fission track) and 9.7 ± 2.8 km Myr^{-1} (zircon fission track). The ages of the samples IK 5 - IK 7 (open symbols in Fig. 19) are projected into this cross section but were not used for the slip rate calculation because the projection over great distances may result in relatively great errors. However, we note that, except for the (U-Th)/He age of IK 6, the ages of samples IK 5 - IK 7 plot reasonably close to the regression lines calculated for samples IK 1 – IK 4 (Fig. 19).

We also calculated a slip rate from the K-Ar muscovite ages of Altherr et al. (1982) from the Messaria shear zone. Our detailed thin-section work on samples from localities where Altherr et al. (1982) collected their samples suggests that white mica completely recrystallized during mylonitization. Therefore, we argue that mylonitization and recrystallization caused complete isotopic reequilibration and that the muscovite K-Ar ages date mylonitization-related mineral growth. The fact that the ages of Altherr et al.(1982) consistently young in a northerly direction and are consistently slightly older than the zircon fission track ages supports this interpretation, which implies that the muscovite ages of 11-10 Ma (Altherr et al. 1982) date ductile deformation in the Messaria shear zone. This interpretation is in line with our $^{87}Rb/^{86}Sr$ result of 12.9 ± 3.5 Ma for sample IK 99XD, which is a maximum age for mylonitization, and our $^{40}Ar/^{39}Ar$ data of 10.8 ± 1.1 Ma for IK 02-4 and of 10.5 ± 2.4 Ma for IK 02-8. The muscovite ages of Altherr et al. (1982) are plotted along cross section E-E' and yielded a slip rate of 7.3 ± 1 km Myr^{-1}, which is similar to the slip rates obtained from low-temperature thermochronology. The $^{40}Ar/^{39}Ar$ phengite ages are projected also into this cross section (open symbols in Fig. 19) but were not used for the slip rate calculation because the projection over great distances may result in relatively great errors.

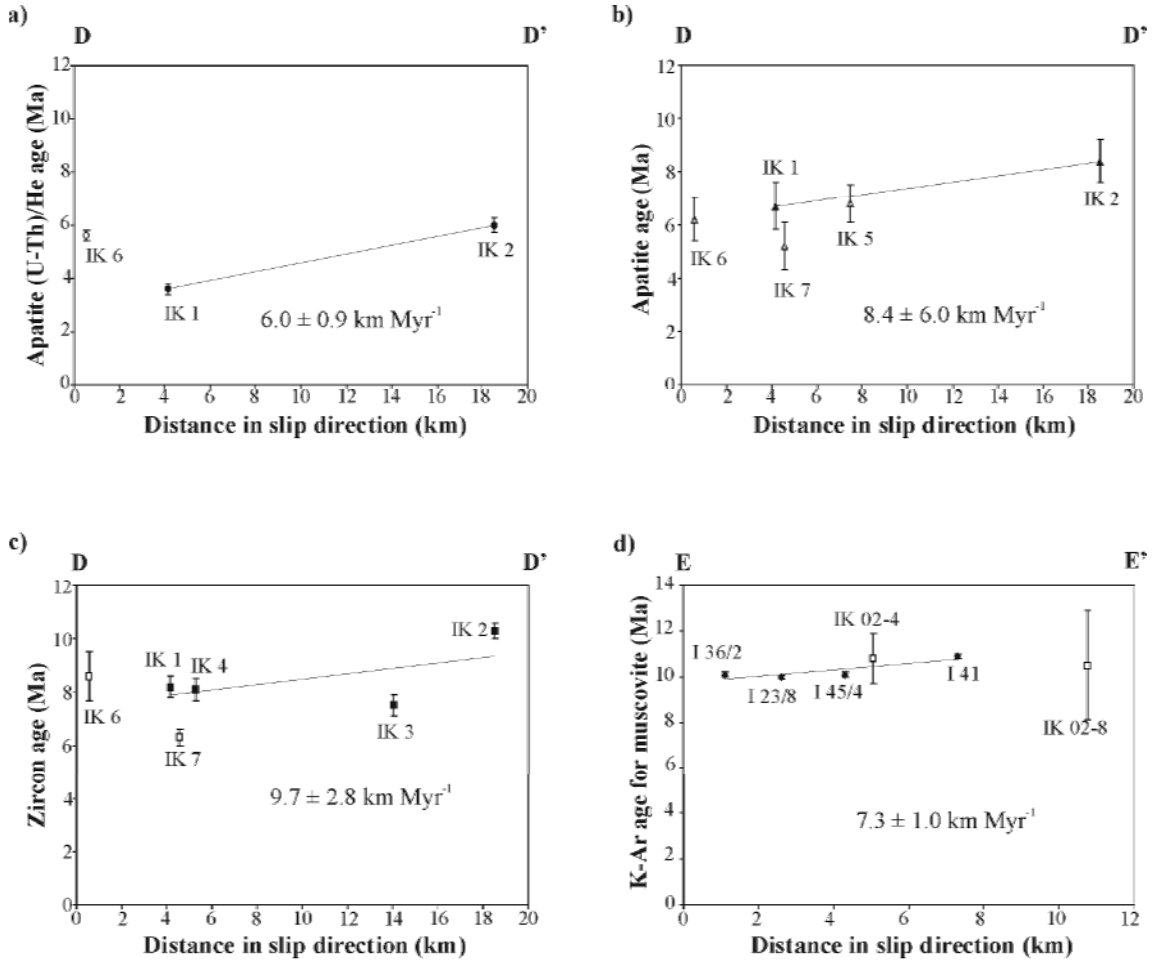

Fig. 19. Diagrams depicting mineral ages from footwall of Messaria extensional fault system against distance in slip direction. (a) Apatite (U-Th)/He ages. (b) Apatite fission track ages. (c) Zircon fission track ages. Slip rates in (a), (b) and (c) were calculated from samples IK 1 – IK 4 (bold symbols) from the I-type granite samples in the western part of the island; samples IK 5 – IK 7 (open symbols) have been projected into cross section D-D'; note that the ages from these samples plot along the regression lines calculated for samples IK 1 – IK 4. (d) K-Ar muscovite ages from Altherr et al. (1982) (solid symbols) and $^{40}Ar/^{39}Ar$ ages from samples IK 02-4 and IK 02-8 (open symbols) plotted along cross section E-E'. The slip rate was only calculated from the K-Ar age data of Altherr et al. (1982).

Vertical ductile thinning

To properly estimate the contribution that vertical ductile thinning made to the total exhumation caused by the Messaria extensional fault system, we need to consider both the vertical rate at which the rocks moved through the crust and the rate of thinning of the remaining overburden at each step along the exhumation path. For this purpose, we use a numerical method, which models exhumation and ductile strain (Feehan & Brandon 1999). To model vertical ductile thinning, we need to know the directions and magnitudes of the principle stretches, the sense and magnitude of rotation, the depth from which the rocks where exhumed in the Messaria extensional fault system, the residence time of the exhuming rocks

in the ductile crust and the azimuth of the transport direction during the accumulation of ductile strain. The principal stretches represent means of the data shown in Table 4 and are S_X:S_Y:S_Z = 1.85:1.03:0.53. The rotation axis is thought to be identical with the mean Y direction and the amount of rotation of 15° has been calculated from the data in Table 4 and Figure 14. The exhumation depth has been set at 15 km based on the P-T data from the shear-zone mylonite. The K-Ar muscovite ages of Altherr et al. (1982), our $^{40}Ar/^{39}Ar$ age data and our zircon fission track ages, the latter of which broadly reflect the time when the samples reached the brittle crust, suggest a relatively short time span of ~2 m.y. during which the rocks were in the ductile regime. The model calculations are based on a ductile-strain-rate law that is proportional with depth and indicate that the ductile thinning contributed about 20% or 3 km to the overall exhumation associated with extensional faulting.

Discussion

To which tectonic unit does the Ikaria nappe belong?

The lack of any high-pressure relics in the Ikaria nappe indicates that it does not belong to the Cycladic blueschist unit. Even in high-pressure rocks of the Cycladic blueschist unit that had a very high temperature overprint (Naxos Island), relics of the earlier high-pressure event were found (Avigad 1998). The only mid-amphibolite-facies units, which have no Tertiary high-pressure overprint in the region are the Çine and Bozdağ nappes of the Anatolide belt of western Turkey (Ring et al. 1999c; Gessner et al. 2001a, Régnier et al. 2003). Large parts of the Çine nappe are ~550 Ma old augen gneiss, which does not occur in the Ikaria nappe. However, the pegmatite of the Ikaria nappe studied here yielded a minimum crystallization age of 458 ± 7 Ma, which might be related to the ~550 Ma magmatic event. We tentatively correlate the Ikaria nappe with the Bozdağ nappe of western Turkey, which also comprises a very thick metapelite sequence and minor marble, amphibolite and quarzite (Ring et al. 2001b). The Çine and Bozdağ nappes belong to the lowest tectonic unit (Menderes nappes) of western Turkey, which was overthrust by the Cycladic blueschist along the Cyclades-Menderes thrust unit in the Eocene (Gessner et al. 2001a). We speculate that the Cyclades-Menderes thrust emplaced the Messaria nappe onto the Ikaria nappe.

Our correlation of the Ikaria nappe with the Bozdağ nappe of the Anatolide belt results in a major geometric problem in the eastern Aegean. On the islands of Fourni and Samos east of Ikaria, the Cycladic blueschist unit rests on the Basal unit (External Hellenides), which in general makes up the lowest tectonic unit in the Aegean. If the Ikaria nappe indeed belongs to the Menderes nappes it would have been derived from Anatolia (see tectonic reconstruction in

Gessner et al. 2001a, their fig. 16) and this implies that the interfingering of Adria and Anatolia has a complex geometry in the eastern Aegean.

Extensional structures on Ikaria

The progressive superposition of ductile, ductile-brittle and brittle structures in the footwall of the Messaria extensional fault system, brittle deformation in the hangingwall and the decrease of cooling ages parallel to the northward slip direction of the hangingwall reflects progressive southward migration of footwall exhumation and is typical for extensional fault systems above metamorphic core complexes.

Initial movement in the ductile Messaria shear zone of the Messaria extensional fault system at ~11 Ma was accompanied and aided by the intrusion of two synkinematic granites (Fig. 20a) and a high thermal field gradient of 25-35°C km^{-1}. Ring et al. (2003a) showed that the Vari detachment on Tinos and Syros islands also formed when the geotherm was elevated at a time when the magmatic arc of the southward retreating Hellenic subduction reached the Cycladic islands and caused a rise in thermal conditions.

The Messaria extensional fault system operated from ~350-400°C to at least 80°C between ~11-3 Ma. Because biotite in samples from the northern portion of the shear zone was, at least in part, stable during mylonitization and our interpretation of the biotite ages of Altherr et al. (1982) implies biotite growth during shearing, temperatures might have been slightly higher than 400°C in the northern part of Ikaria. T-t paths indicate rapid cooling as the footwall was exhumed to the surface. The Messaria detachment probably rooted at the brittle/ductile transition and its carapace Messaria shear zone in the directly underlying ductile crust. The fact that the cooling rates of both the I-type granite and the metapelite of the Ikaria nappe are largely similar is thought to be due to early intrusion of the granite during extensional shearing and that both rocks units were then exhumed and cooled together. This interpretation would imply intrusion ages of ~11 Ma for the two synkinematic granites.

Average slip rates at the Messaria extensional fault system were ~7-8 km Myr^{-1}. This rate would yield a displacement of ~60 km for the period from ~11-3 Ma. This displacement and the maximum depth of 15 km for the onset of extensional faulting provides a dip angle of ~15° for the Messaria extensional fault system. A prerequisite for the development of low-angle faults appears to be that they have to reactivate earlier fault planes (Ring et al. 2003b). Pre-extension thrusts were not observed on Ikaria. However, the occurrence of the high-pressure Messaria nappe above the non-high-pressure rocks of the Ikaria nappe suggests that the contact between these two nappes was a thrust, probably the Cyclades-Menderes thrust. If

so, extensional reactivation of this thrust plane would be in line with the low-angle nature of the Messaria extensional fault system.

How does the Fanari detachment relate to the Messaria extensional fault system? The occurrence of allochtonous Pliocene sediments in the hangingwall of the Fanari detachment indicates that movement on it continued until or commenced after ~5 Ma. Because movement on the Messaria extensional fault system lasted until ~3 Ma, it appears feasible to assume that the Fanari detachment is a brittle fault in the hangingwall of Messaria extensional fault system and hence is ultimately related to the latter (Fig. 20b).

The kinematic indicators in the Messaria shear zone and the brittle Messaria and Fanari detachments together with this spatial trend of footwall cooling ages indicates a general top-to-the-NNE sense of movement. However, in the southeast of the island, late-stage top-to-the-SSW shear-sense indicators occur at the Messaria detachment. We envisage that these late-stage minor antithetic extensional structures were related to updoming of Ikaria (Fig. 20c). The opposed dip to the general north-dipping Messaria extensional fault system can be interpreted as folding of the mylonitic zone similar to the model described by Reynolds & Lister (1990) for the formation of the metamorphic core complexes in the Basin and Range province.

Exhumation of the Ikaria and Messaria nappes

The strain and rotation data indicate that extensional faulting in the Messaria extensional fault system was accompanied by vertical thinning, which caused ~20% or 3 km of exhumation of the Ikaria nappe during extensional shearing from ~15 km depth. The remaining 80% of exhumation must be due to erosion and normal faulting. We have no control on erosion. Topography above a retreating subduction zone is generally considered to be subdued (Royden 1993) and therefore erosion rates were probably small. Assumed erosion rates of 0.2-0.4 km Myr^{-1} yields a total erosion of 1.5-3 km during extensional faulting. It follows that ~10 km of exhumation of the Ikaria nappe must have been due to normal faulting.

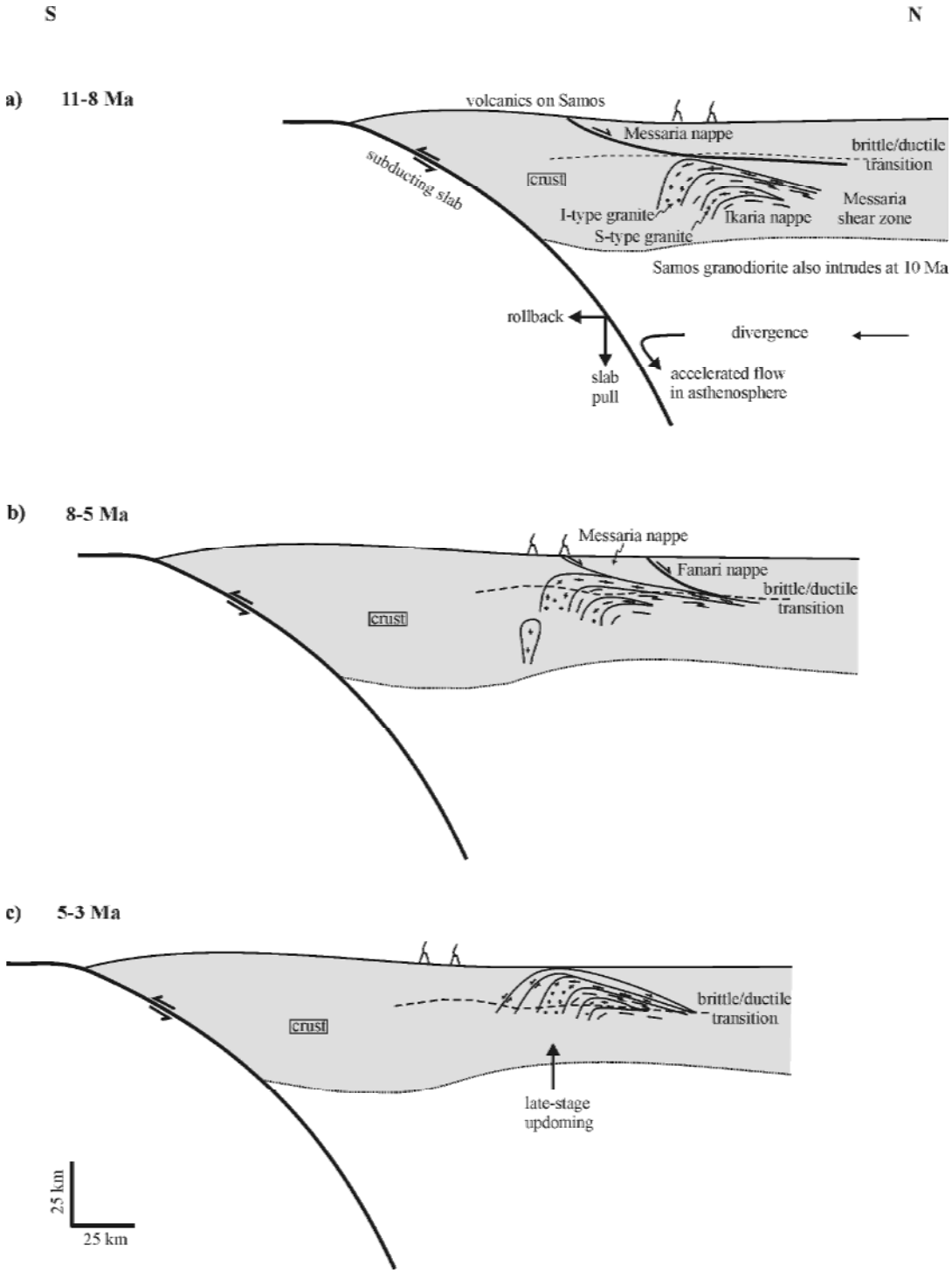

Fig. 20. Three stage evolution of extensional deformation on Ikaria. (a) Inception of Messaria extensional fault system aided by intrusion of two synkinematic granites in the magmatic arc of the Hellenic subduction zone. Note that an ~10 Ma old granodiorite in westernmost Samos and 11 Ma old volcanic rocks on Samos Island (Weidmann et al. 1984) are of the same age. Subduction-zone retreat caused intra-arc extension at this stage. The simplified arrows show accelerated corner flow in the asthenosphere behind the retreating subduction zone, which caused relative plate divergence in the intra- and back-arc area. According to the flow-line modelling of retreating subduction zones by Garfunkel *et al.* (1986), the asthenospheric flow in the arc and back-arc region behind retreating slabs is forced to accelerate in the horizontal to fill the free space caused by the retreating subduction zone causing plate divergence. (b) Messaria shear zone moved into brittle crust and is juxtaposed with Messaria detachment. The magmatic arc probably shifted shouthward. (c) Late-stage updoming of footwall as a response to unloading.

Comparisons with other extensional fault systems in the Aegean

Because most of the Aegean region is under water any regional correlations are necessarily speculative. Scaling relationship for faults suggests that large-scale structures such as the Messaria extensional fault system must continue laterally over great distances as far as Samos Island (Fig. 1). Most straightforward to us appears the correlation of the Fanari and Kallithea detachments. Both detachments have the same shear sense and have non-metamorphic units in their hangingwall, which contain Pliocene sediments. Inception of the Kallithea detachment is fairly well dated at ~10 Ma age (Ring et al. 1999c) and a granite dyke in its footwall yielded a zircon fission track age of 7.3 ± 0.6 Ma (Fig. 4). If it was accepted that the Fanari detachment is related to the Messaria extensional fault system, then the Kallithea detachment would also be part of the Messaria extensional fault system.

Ductile extensional shearing on Samos has no relationship to the brittle Kallithea detachment. One single zircon fission track age of 14.1 ± 0.8 Ma from the Basal unit (Fig. 4, Table 7) suggests that the Kerketas extensional system is slightly older than the Messaria extensional fault system on Ikaria. Ductile extension and exhumation of the Ampelos nappe at the Selçuk extensional system lasted until in the Early Miocene as indicated by zircon fission track ages of 20-18 Ma (see above), which consistently young northeastward in the direction of hangingwall slip. The zircon fission track ages indicate that the Selçuk and Kerketas extensional systems are unrelated to each other and, together with the different movement directions also show that both extensional systems are unrelated to the Messaria extensional fault system.

The progressive evolution of ductile deformation in mylonitic shear zones associated with brittle detachment fault systems has also been documented on Naxos/Paros and Ios islands (Buick 1991; Vandenberg & Lister 1996). On other islands (e.g. Tinos, Syros, Mykonos, Sifnos, Serifos) ductile extensional shearing and/or brittle detachment faulting has also been reported (Avigad & Garfunkel 1989; Urai et al. 1990; Lee & Lister 1992; Gautier & Brun 1994; Lister & Raouzaios 1996; Lister & Forster 1996; Ring et al. 2003a) but the intimate association of ductile and brittle deformation is less clear. There are also differences in the timing and depth of formation of the extensional fault systems.

On Naxos and Paros, extensional shearing at the Mountsouna extensional system commenced during anatectic conditions at or before 20-16 Ma (Buick 1991). Buick & Holland (1989) suggested that extensional shearing commenced at P-T conditions of ~400-700°C and 5-7 kbar indicating that the extensional shear zone rooted in the lower crust and not close to the brittle ductile transition as suggested herein for the Messaria extensional fault system on Ikaria. Extensional deformation caused the pronounced NNE-elongation of the migmatite

dome on Naxos, the latter of which is unique in the Aegean. Extension lasted relatively long (until ~8-12 Ma, Brichau et al. 2004) and continued during and after the intrusion of a huge granodiorite at ~12.5 ± 1.0 Ma (Wijbrans & McDougall 1988). The late kinematic evolution of the Mountsouna extensional system during and after the intrusion of the granitoid was very similar to that of the Messaria extensional fault system on Ikaria.

The structural evolution of the extensional fault system on Ios is similar to that on Ikaria. On Ios, the South Cyclades shear zone is the carapace shear zone to the brittle Ios detachment and this shear zone system operated between ~12-8 Ma (Baldwin & Lister 1998; S. Brichau unpublished zircon and apatite fission-track data) and was associated with the intrusion of minor granites. An important difference between Ios and Ikaria is that the Ios extensional system had a dominantly top-to-the-S sense of displacement (Gautier & Brun 1994).

The ductile extensional shear zone on Tinos is not obviously related to the brittle Vari detachment on this island. Top-to-the-NE ductile extensional shearing is dated at 22-20 Ma (Bröcker & Franz 1998) and top-to-the-NE movement on the Vari detachment occurred between 12-9 Ma as inferred from zircon and apatite fission track thermochronology (Ring et al. 2003a). These timing constraints suggest that both extensional structures are unrelated or that extensional movement was slow. Further work is needed to clarify the relationship between ductile and brittle extension on Tinos Island.

Important similarities among the Cycladic detachments appear to exist for the intra-arc period of the Cyclades between ~14-5 Ma. During this time span a number of granitoids intruded into the footwalls of various detachment systems (e.g. Mykonos, Naxos/Paros, Ikaria, Samos, Ios, Serifos). The intimate relationship between arc-related magmatism and extensional shearing was aided by relatively high thermal gradients and extensional stresses caused by an extensional boundary condition in the mantle caused by subduction-zone retreat (Ring et al. 1999c).

Conclusions

A low-angle ductile shear zone associated with two brittle detachment faults of Late Miocene to Pliocene age has been documented on Ikaria Island. The ductile shear zone formed in the uppermost ductile crust under mid-greenschist facies conditions. Ductile shearing was not by simple shear and involved a component of vertical shortening. Cooling in the footwall of the extensional fault system was rapid and the offset was of the order of 60 km. The dominant shear sense was top-to-the-NNE; during footwall unloading and doming of the extensional fault system minor late-stage antithetic shears developed.

References

ALTHERR, R., KREUZER, H., WENDT, I., LENZ, H., WAGNER, G.A., KELLER, J., HARRE, W. & HÖHNDORF, A. 1982. A late Oligocene/early Miocene high temperature belt in the Attic-Cycladic crystalline complex (SE Pelagonian, Greece). *Geologisches Jahrbuch*, **E23**, 97-164.

AVIGAD, D. & GARFUNKEL, T. 1989. Low-angle faults above and below a blueschist belt-Tinos Island, Cyclades, Greece. *Terra Nova*, **1**, 182-187.

AVIGAD, D. 1998. High-pressure metamorphism and cooling on SE Naxos (Cyclades, Greece). *Eur. Journal of Mineralogy*, **10** (6), 1309-1319.

BAILEY, C.M., SIMPSON, C. & DE PAOR, D.G. 1994. Diffusional mass transfer and crystal plasticity in the deformation of granitic rocks of the Blue Ridge Thrust Sheet, S.W. Virginia. *Journal of Structural Geology*, **16,** 1403-1416.

BALDWIN, S.L. & LISTER, G.S. 1998. Thermochronology of the South Cyclades shear zone, Ios, Greece: Effects of ductile shear in the argon partial retention zone. *Journal of Geophysical Research*, **103**, 7315-7336.

BRICHAU, S., RING, U., CARTER, A. & BRUNEL, M. 2004. Long-term evolution of the slip rate for a major extensional fault system, Naxos and Paros islands, Greece. *Earth and Planatary Sciences Letters* (submitted).

BRÖCKER, M., KREUZER, H., MATTHEWS, A. & OKRUSCH, M. 1993. $^{40}Ar/^{39}Ar$ and oxygen isotope studies of polymetamorphism from Tinos Island, Cycladic blueschist belt, Greece. *Journal of Metamorphic Geology*, **11**, 223-240.

BRÖCKER, M. & FRANZ, L. 1998. Rb-Sr dating of metamorphic rocks from the Upper and Intermediate Tectonic Units on Tinos (Cyclades, Greece). *Geological Magazine*, **135**, 369-382.

BUICK, I.S. 1991. Mylonite fabric development on Naxos, Greece. *Journal of Structural Geology*, **13** (6), 643-655.

BUICK, I.S. & HOLLAND, T.J.B. 1989. The P-T-t path associated with crustal extension, Naxos, Cyclades, Greece. *In*: Evolution of Metamorphic Belts (edited by Daly, J.S., Cliff, R.A. & Yardley, B.W.D.). *Special Publications of the Geological Society of London*, **43**, 365-370.

CHOUKROUNE, P. & GAPAIS, D. 1983. Strain pattern in the Aar granite (Central Alps): orthogneiss development by bulk inhomogeneous flattening. *Journal of Structural Geology*, **5**, 411-418.

COWAN, D.S. & BRANDON, M.T. 1994. A symmetry-based method for kinematic analysis of large-slip brittle fault zones. *American Journal of Science*, **294** (3), 257-306.

COWARD, M.P. 1976. Strain within ductile shear zones. *Tectonophysics*, **34**, 181-197.

DÜRR, S., ALTHERR, R., KELLER, J., OKRUSCH, M. & SEIDEL, E. 1978. The Median Aegean Crystalline Belt: Stratigraphy, structure, metamorphism, magmatism. *In*: Alps, Apennines, Hellenides, Cloos, H., Roeder, D. & Schmidt, K., E. Schweizerbart'sche Verlagsbuchhandlung, Stuttgart, 455-477.

FARLEY, K.A., WOLF, R.A., & SILVER, L.T. 1996. The effect of long alpha-stopping distances on (U-Th)/He ages. *Geochimica et Cosmochimica Acta*, **60**, 4223-4229.

FAURE, M., BONNEAU, M. & PONS, J. 1991. Ductile deformation and syntectonic granite emplacement during the late Miocene extension of the Aegean (Greece). *Bulletin de la Société Géologique de France*, **162**, 3-11.

FEEHAN, J.G. & BRANDON, M.T. 1999. Contribution of ductile flow to exhumation of low-temperature, high-pressure metamorphic rocks: San Juan-Cascade nappes, NW Washington State. *Journal of Geophysical Research-Solid Earth*, **104** (B5), 10883-10902.

FLINN, D. 1962. On folding during three-dimensional progressive deformation. *Quarternary Journal of Geological Society of London*, **118**, 385-433.

FOSTER, D.A. & JOHN, B.E. 1999. Quantifying tectonic exhumation in an extensional orogen with thermochronology: examples from the southern Basin and Range province. *In*: Exhumation Processes: Normal faulting, ductile flow and erosion (eds U. Ring et al). *Geological Society of London, Special Publications*, **154**, 343-364.

FOSTER, D.A., GLEADOW, A.J.W., REYNOLDS, S.J. & FITZGERALD, P.G. 1993. Denudation of Metamorphic Core Complexes and the Reconstruction of the Transition Zone, West Central Arizona: Constraints From Apatite Fission Track Thermochronology. *Journal of Geophysical Research*, **98**, 2167-2185.

FRY, N. 1979. Density distribution techniques and strain length methods for determination of finite strains. *Journal of Structural Geology*, **1**, 221-229.

FYTIKAS, M., INNOCENTI, F., MANETTI, P., MAZZUOLI, R., PECCERILLO, A. & VILLARI, L. 1984.Tertiary to Quaternary evolution of volcanism in the Aegean region. *In*: The geological evolution of the eastern Mediterranean (eds A.H.F. Robertson and J.E. Dixon). *Geological Society of London, Special Publication*, **17**, 687-699.

GALBRAITH, R.F. 1992. Statistical models for mixed ages. 7th International Workshop on Fission Track Thermochronology, Abstracts with Programs, Philadelphia, July, 1992.

GARFUNKEL, Z., ANDERSON, C. A. AND SCHUBERT, G. 1986. Mantle circulation and the lateral migration of subducted slabs. *Journal of Geophysical Res*earch, **91**, 7205-7223.

GAUTIER, P. & BRUN, J.P. 1994. Crustal-scale geometry and kinematics of late-orogenic extension in the central Aegean (Cyclades and Evvia Island). *Tectonophysics*, **238**, 399-424.

GESSNER, K., RING, U., PASSCHIER, C.W. & GÜNGÖR, T. 2001a. How to resist subduction: Eocene post-high-pressure emplacement of the Cycladic blueschist unit onto the Menderes nappes, Anatolide belt, western Turkey. *Journal of Geological Society of London*, **158**, 769-780.

GESSNER, K., COLLINS, A.S., RING, U. & GÜNGÖR, T. 2004. Structural and thermal history of poly-orogenic basement: U-Pb geochronology of granitoid rocks in the southern Menderes Massif, Western Turkey. *Journal Geological Society London*, **161**, 93-101.

GLODNY, J., GRAUERT, B., FIALA, J., VEJNAR, Z. & KROHE, A. 1998. Metapegmatites in the western Bohemian massif: ages of crystallisation and metamorphic overprint, as constrained by U-Pb zircon, monazite, garnet, columbite and Rb-Sr muscovite data. *Geologische Rundschau*, **87**, 124-134.

GLODNY, J., BINGEN, B., AUSTRHEIM, H., MOLINA, J.F. & RUSIN, A. 2002. Precise eclogitisation ages deduced from Rb/Sr mineral systematics: The Maksyutov complex, Southern Urals, Russia. *Geochimica et Cosmochimica Acta*, **66** (7), 1221-1235.

GODFRIAUX, I. 1968. Etude géologique de la région de l'Olympe (Gréce*). Annales Géologiques des Pays Helleniques*, **19**, 1-271.

GREEN, P.F., DUDDY, I.R, GLEADOW, A.J.W., TINEGATE, P.R. & LASLETT, G.M. 1986. Thermal annealing of fission tracks in apatite, 1.A qualitative description. *Chemical Geology*, **59**, 237-253.

HETZEL R.& GLODNY J. 2002. A crustal-scale, orogen-parallel strike-slip fault in the Middle Urals: age, magnitude of displacement, and geodynamic significance. *International Journal of Earth Sciences*, **91**, 231-245.

HOLLAND, T.J.B. 2000. AX: A program to calculate activities of mineral end members from chemical analyses which uses the activity models outlined in Holland & Powell (1998).

HOSSACK, J.R. 1968. Pebble deformation and thrusting in the Bygdin Area, Soroy, Southern Norway. *Tectonophysics*, **5**, 315-339.

HOUSE, M.A., WERNICKE, B.P., FARLEY, K.A. & DUMITRU, T.A. 1997. Cenozoic thermal evolution of the central Sierra Nevada, California, from (U-Th)/He thermochronometry. *Earth and Planetary Science Letters*, **151**, 167-179.

HURFORD, A.J. 1990. Standardization of fission track dating calibration: recommendation by the Fission Track Working Group of the I.U.G.S. Subcommission on Geochronology. *Chemical Geology (Isotope Geoscience Section)*, **80**, 171-178.

HURFORD, A.J. & GREEN, P.F. 1982. A user's guide to fission-track dating calibration. *Earth and Planetary Sciences Letters*, **59**, 343-354.

KEAY, S.M. 1998. The geological evolution of the Cyclades, Greece: constraints from SHRIMP U-Pb geochronology. PhD thesis, Australian National University, Canberra.

LEE, J. & LISTER, G.S. 1992. Late Miocene ductile extension and detachment faulting, Mykonos, Greece. *Geology*, **20**, 121-124.

LISTER, G.S. & FORSTER, M. 1996. Inside the Aegean metamorphic core complexes. *Technical Publications Australian Crustal Research Centr*e, **45**, 110p.

LISTER, G.S. & RAOUZAIOS, A. 1996. The tectonic significance of a porphyroblastic blueschist facies overprint during Alpine orogenesis, Sifnos, Aegean Sea, Greece. *Journal of Structural Geology*, **18**, 1417-1435.

LISTER, G.S., BANGA, G. & FEENSTRA, A. 1984. Metamorphic core complexes of Cordilleran type in the Cyclades, Aegean Sea, Greece. *Geology*, **12**, 221-225.

MCDOUGALL, I. & HARRISON, T.M. 1988. Geochronology and Thermochronology by the $^{40}Ar/^{39}Ar$ method. *Oxford University Press*, *New York*, 212p.

MÜLLER, W., DALLMEYER, R.D., NEUBAUER, F. & THÖNI, M. 1999. Deformation-induced resetting of Rb/Sr and $^{40}Ar/^{39}Ar$ mineral systems in a low-grade, polymetamorphic terrane (Eastern Alps, Austria). *Journal of the Geological Society of London*, **156**, 261-278.

MÜLLER, W. 2003. Strengthening the link between geochronology, textures and petrology. *Earth and Planetary Science Letters,* **206**, 237-251.

O'HARA, K. 1990. State of strain in mylonites from the western Blue Ridge province, southern Appalachians: the role of volume loss. *Journal of Structural Geology*, **15**, 849-863.

OWENS, W.H. 1984. The calculation of a best fit ellipsoid from elliptical sections on arbitrarily oriented planes. *Journal of Structural Geology*, **6**, 571-578.

PASSCHIER, C.W. 1987. Stable positions of rigid objects in non-coaxial flow-a study in vorticity analysis. *Journal of Structural Geology*, **9**, 679-690.

PASSCHIER, C.W. 1988. Analysis of deformation paths in shear zones. *Geologische Rundschau*, **77**, 309-318.

PASSCHIER, C.W. 1990. Reconstruction of deformation and flow parameters from deformed vein sets. *Tectonophysics*, **180**, 185-199.

PEACH, C.J. & LISLE, R.J. 1979. A Fortran IV program for the analysis of tectonic strain using deformed elliptical markers. *Computers and Geoscience*, **5**, 325-334.

POWELL, R., HOLLAND, T.J.B. & WORLEY, B. 1998. Calculating phase diagrams involving solid solutions via non-linear equations, with examples using Thermocalc. *Journal of Metamorphic Geology*, **16**, 577-588.

RAMSAY, J.G. & HUBER, M.I. 1983: The Techniques of Modern Structural Geology. Volume 1:Strain analysis. Academic Press, London, 307p.

RAMSAY, J.G. 1967. Folding and fracturing of rocks. McGraw-Hill, New York, 568p.

REDDY, S.M., WHEELER, J., BUTLER, R.W.H., CLIFF, R.A., FREEMAN, S., INGER, S., PICKLES, C. & KELLEY, S.P. 2003. Kinematic reworking and exhumation within the convergent Alpine Orogen. *Tectonophysics*, **365**, 77-102.

RÉGNIER, J.L., RING, U., PASSCHIER, C.W., GESSNER, K. & GÜNGÖR, T. 2003. Contrasting metamorphic evolution of metasedimentary rocks from the Çine and Selimiye nappes in the Anatolide belt, western Turkey. *Journal of Metamorphic Geology*, **21**, 1-23.

REYNOLDS, S.J. & LISTER, G.S. 1990. Folding of mylonitic zones in Cordilleran metamorphic core complexes: Evidence from near the mylonitic front. *Geology*, **18**, 216-219.

RING, U. 1999. Volume loss, fluid flow and coaxial vs noncoaxial deformation in retrograde, amphibolite-facies shear zones, northern Malawi, east-central Africa. *Geological Society of America Bulletin*, **111**, 123-142.

RING, U., BRANDON, M.T., WILLETT, S.D. & Lister, G.S. 1999a. Exhumation processes. *In*: Exhumation Processes: Normal faulting, ductile flow and erosion, Ring, U., Brandon, M.T., Lister, G.S., Willett, S. (eds.). *Geological Society London Special Publications*, **154**, 1-27.

RING, U., GESSNER, K., GÜNGÖR, T. & PASSCHIER, C.W. 1999c. The Menderes Massif of western Turkey and the Cycladic Massif in the Aegean - do they really correlate? *Journal Geological Society London*, **156**, 3-6.

RING, U., JOHNSON, C., HETZEL, R. & GESSNER, K. 2003b. Tectonic denudation of a Late Cretaceous–Tertiary collisional belt: regionally symmetric cooling patterns and their relation to extensional faults in the Anatolide belt of western Turkey. G*eological Magazine*, **140**, 421-441.

RING, U. & LAYER, P.W. 2003. High-pressure metamorphism in the Aegean, eastern Mediterranean: Underplating and exhumation from the Late Cretaceous until the Miocene to Recent above the retreating Hellenic subduction zone. *Tectonics*, **22** (3), 1022, doi: 10.1029/2001ITC001350, 23p.

RING, U., LAYER, P.W. & REISCHMANN, T. 2001a. Miocene high-pressure metamorphism in the Cyclades and Crete, Aegean Sea, Greece: Evidence for large-magnitude displacement on the Cretan detachment. *Geology*, **29**, 395-398.

RING, U., LAWS, S. & BERNET, M. 1999b. Structural analysis of a complex nappe sequence and late-orogenic basins from the Aegean Island of Samos, Greece. *Journal of Structural Geology*, **21**, 1575-1601.

RING, U. & REISCHMANN, T. 2002. The weak and superfast Cretan detachment, Greece: exhumation at subduction rates in extruding wedges. *Journal of the Geological Society of London*, **159**, 225-228.

RING, U., THOMSON, S.N. & BRÖCKER, M. 2003a. Fast extension but little exhumation: the Vari detachment in the Cyclades, Greece. *Geological Magazine*, **140**, 245-252.

RING, U., WILLNER, A.P. & LACKMANN, W. 2001b. Stacking of nappes with unrelated pressure-temperature paths: an example from the Menderes nappes of western Turkey. *American Journal of Science*, **301**, 912-944.

ROBERTSON, A.H.F., CLIFT, P., DEGNAN, P.J. & JONES, G. 1991. Palaeogeographic and palaeotectonic evolution of the Eastern Mediterranean Neotethys. *Palaeogeography, Palaeoclimatology, Palaeoecology*, **87**, 289-343.

ROYDEN, L. 1993. The tectonic expression of slab pull at continental convergent boundaries. *Tectonics*, 12, 303-325.

SAMSON, S.C. & ALEXANDER, E.C. 1987. Calibration of the interlaboratory 40Ar/39Ar dating standard MMHb-1. *Chemical Geology*, 66, 27-34.

SIMPSON, C. & DE PAOR, D.G. 1993. Strain and kinematic analysis in general shear zones. *Journal of Structural Geology*, **15**, 1-20.

TAGAMI, T., GALBRAITH, R.F., YAMADA, R. & LASLETT, G.M. 1998. Revised annealing kinetics of fission tracks in zircon and geological implications. *In:* Advances in fission-track geochronology (eds van den Haute, P. et al.). *Kluwer Academic Publishers*, 99-112.

TOMASCHEK, F., KENNEDY, A., VILLA, I.M. & BALLHAUS, C. 2003. Zircons from Syros, Cyclades, Greece- Recrystallization and mobilisation during high pressure metamorphism. *Journal of Petrology*, **44**, 1977-2002.

URAI, J.L., SCHUILING, R.D. & JANSEN, J.B.H. 1990. Alpine deformation on Naxos (Greece). *In*: KNIPE, R.J. & RUTTER, E.H. (eds) Deformation Mechanisms, Rheology and Tectonics. *Geological Society, London, Special Publication*, **54**, 509-522.

VANDENBERG, L.C. & LISTER, G.S. 1996. Structural analysis of basement tectonites from the Aegean metamorphic core complex of Ios, Cyclades, Greece. *Journal of Structural Geology*, **18**, 1437-1454.

WEI, C. & POWELL, R. 2003. Phase relations in high-pressure metapelites in the system KFMASH (K_2O-FeO-MgO-Al_2O_3-SiO_2-H_2O) with application to natural rocks. *Contributions to Mineralogy and Petrology*, **145**, 301-315.

WEIDMANN, M., SOLOUNIAS, N., DRAKE, R.E. & CURTIS, G.H. 1984. Neogene stratigraphy of eastern basin, Samos Island, Greece. *Geobis*, **17**, 477-490.

WIJBRANS, J.R., SCHLIESTEDT, M. & YORK, D. 1990. Single grain argon laser probe dating of phengites from the blueschist to greenschist transition on Sifnos (Cyclades, Greece). *Contributions to Mineralogy and Petrology*, **104**, 582-593.

WIJBRANS, J.R. & MCDOUGALL, I. 1988. Metamorphic evolution of the Attic Cycladic metamorphic belt on Naxos (Cyclades, Greece) utilising the $^{40}Ar/^{39}Ar$ age spectrum measurements. *Journal of Metamorphic Geology*, **6**, 571-594.

WILL, T., OKRUSCH, M., SCHMÄDICKE, E. & CHEN, G. 1998. Phase relations in the greenschist-blueschist-amphibolite-eclogite facies in the system Na_2O-CaO-FeO-MgO-Al_2O_3-SiO_2-H_2O (NCFMASH), with application to metamorphic rocks from Samos, Greece. *Contributions to Mineralogy and Petrology*, **132**, 85-102.

WOLF, R.A., FARLEY, K.A. & SILVER, L.T. 1996. Helium diffusion and low-temperature thermochronometry of apatite. *Geochimica et Cosmochimica Acta*, **60**, 4231-4240.

ZEITLER, P.K., HERCZEG, A.L., MCDOUGALL, I. & HONDA, M. 1987. (U-Th)/He dating of apatite: A potential thermochronometer. *Geochimica et Cosmochimica Acta*, **51**, 2865-2868.

Chapter 3

Exhumation of the Cycladic blueschist unit by a Late Eocene/Early Oligocene extrusion wedge in western Turkey

Abstract

In this study we evaluate the question how the pre-Miocene exhumation of the Cycladic blueschist unit in western Turkey was accomplished. In particular, we test if there is evidence for an extrusion wedge. The main feature of an extrusion wedge is a basal thrust which operated coevally with a normal fault at its top. It has been speculated that such an extrusion wedge aided exhumation of the Cycladic blueschist unit in western Turkey.

We sampled mylonites to constrain the timing of the upper normal fault between the Selçuk nappe and the underlying Ampelos/Dilek nappe of the Cycladic blueschist unit as well as of the thrust between the Ampelos/Dilek nappe and the underlying Menderes nappes. For dating we used both the $^{40}Ar/^{39}Ar$ and $^{87}Rb/^{86}Sr$ method. The $^{40}Ar/^{39}Ar$ ages for the upper mylonite zone range from 35.4 ± 0.8 to 41.5 ± 2.0 Ma and for the lower mylonite zone from 34.3 ± 0.6 to 38.6 ± 0.6 Ma. The $^{87}Rb/^{86}Sr$ data indicate an age of 37.0 ± 5.0 Ma for the upper contact and the ages for the lower contact range from 32.5 ± 0.4 to 34.4 ± 2.6 Ma. Our results show that both contacts formed at the same time.

We conclude that a Late Eocene/Early Oligocene extrusion wedge in western Turkey exists. Available P-T data show that ~30-35 km of exhumation of the Ampelos/Dilek nappe of the Cycladic blueschist unit was accomplished in this extrusion wedge.

Introduction

In many orogens it can be shown that the bulk of exhumation of high-pressure rocks occurred during an early stage of the orogenic history (Avigad et al. 1997; Gessner et al. 2001). How the significant exhumation of high-pressure rocks occurred in early orogenic phases is widely unknown. Since a few years so-called extrusion wedges are discussed. The typical characteristic of such a wedge is normal faulting at its top coeval with thrusting at its base. Burchfiel and Royden (1985) proposed an extrusion wedge in the Himalaya, defined by the north-dipping South Tibetan normal fault system at its top and the south-directed Main Boundary Thrust and/or Main Central Thrust at its base, and suggested that both contacts operated in the Early Miocene. They suggested that the formation of the South Tibetan normal

fault system took place between 15 and 30 Ma (Allegre et al. 1984), and the formation of Pliocene north-trending normal faults cutting the former. The thrust fault at the base of the southward-moving wedge are identical to the contemporaneous subduction boundary between India and Tibet (Burchfiel & Royden 1985). Murphy and Harrison (1999) emphasized, based on their U-Th-Pb dating of granites, which intruded into the upper contact, that Miocene Himalayan deformation was not characterized by contemporaneous extension along the South Tibetan normal fault system and shortening along the Main Central Thrust. They showed that the timing of thrusting at the Main Central Thrust occurred between 18 and 22 Ma, which is based on its hangingwall deformation (Hodges et al. 1992), and that slip along the detachment system occurred between 11 and 17 Ma. Murphy and Harrison (1999) assumed that the Main Central Thrust was inactive during the operating time of the upper normal fault contact.

In the Aegean a significant amount of exhumation of the famous Cycladic blueschist unit is attributed to normal faulting caused by the rollback of the subducting Hellenic slab (Lister et al. 1984; Royden 1993). Late Miocene low-angle normal fault (detachments) are well documented in the Aegean, e.g. on the islands of Naxos/Paros, Ikaria, Ios, Tinos, Syros, Mykonos, Sifnos and Serifos (Buick 1991; Kumerics et al. 2004; Vandenberg & Lister 1996; Avigad & Garfunkel 1989; Lee & Lister 1992; Lister & Foster 1996; Ring et al. 2003a). However, the late-stage normal faults accomplished only a few kilometer of the overall exhumation of the high-pressure rocks. Ring et al. (1999b) assumed, based on the geologic relationships on the island of Evia and Samos, that up to 30-40 km of the exhumation of the Cycladic blueschist unit must have occurred before the Middle Oligocene, more or less during subduction and blueschist-facies metamorphism. Thus, the important question is how exhumation in early orogenic phases was accomplished and if there is evidence for an extrusion wedge, which aided the exhumation of the Cycladic blueschist unit. An Early Miocene extrusion wedge on the island of Crete is well documented. It is bounded by the Cretan detachment in the hangingwall and the subjacent subduction thrust at the base and exhumed ~85-90% of the external high-pressure belt (Thomson et al. 1998). On the island of Sifnos, Raouzaios et al. (1996) showed that normal faulting was operating during the Early Oligocene at the same time as the Cycladic blueschist unit was thrust onto the Basal unit (Ring & Layer 2003) what suggests that an Early Oligocene extrusion wedge exists. Evidence for older extrusion wedges is so far more ambiguous. Gessner et al. (2001) discussed an Eocene extrusion wedge in western Turkey. They assumed that an Eocene top-NE ductile extensional shear zone between the ophiolitic Selçuk nappe and the underlying Dilek nappe of the Cycladic blueschist unit operated at the same time as the latter nappes were thrust onto the underlying Menderes nappes at ~37 Ma.

The purpose of this chapter is to evaluate the assumption made by Gessner et al (2001). We sampled mylonite rocks from the upper and lower contacts of the putative extrusion wedge and dated the mylonites. Our data indicate that both mylonite zones formed at ~35 Ma and thus provide strong evidence for a Late Eocene/Early Oligocene extrusion wedge accomplishing ~30-35 km of the exhumation of the Ampelos/Dilek nappe in western Turkey.

Overview of the geological setting

The nappe pile in the Aegean and western Turkey

The Hellenide-Anatolide orogen in the eastern Mediterranean can be subdivided into a series of tectonic units, which are different in lithology, stratigraphy and metamorphism (Fig. 1). The units are from top to bottom: (1) the Internal zone, (2) the Vardar-İzmir-Ankara zone, (3) the Lycian nappes, (4) the Cycladic zone, and the (5) External Hellenides. A difference between both orogens is that in western Turkey the Menderes nappes instead of the External Hellenides are forming the lowest tectonic unit. The Internal zone is considered part of Eurasia and Sakarya underneath which oceanic crust of the northern Neotethys was subducted. The related suture is the Vardar-İzmir-Ankara zone (Sengör & Yilmaz 1981), which was partly metamorphosed under blueschist-facies conditions in the late Cretaceous (Sherlock et al. 1999; Ring & Layer 2003). The Lycian nappes are a thin-skinned thrust belt, which is assumed to root in the Vardar-İzmir-Ankara zone (Collins & Robertson 1997) and partly metamorphosed under incipient high-pressure conditions (Franz & Okrusch 1992). They are made up of sheared red-green phyllite of the so-called Karaova series above which a Mesozoic passive-margin sequence is exposed (Güngör & Erdogan 2001). This succession is capped by Late Cretaceous flysch (Bernoulli et al. 1974). The Cycladic zone can be subdivided into three tectonic units, which are from top to bottom: (1) the Upper unit with the heterogeneous Cycladic ophiolite nappe containing unmetamorphosed to greenschist-facies ophiolitic and sedimentary rocks with high-grade metamorphic blocks of Jurassic and Cretaceous age, (2) the Cycladic blueschist unit, which is again subdivided into three high-pressure nappes comprising from top to bottom: (a) an ophiolitic mélange, (b) a Permo-Mesozoic shelf sequence composed of metabasite and metasediments including chlorizoid-kyanite schist and marble, and (c) a Carboniferous basement made up of orthogneiss (Reischmann 1997), which intruded a metasedimentary sequence. (3) The Basal unit is only exposed in a few tectonic windows and is probably part of the External Hellenides, which are a thrust pile of Permian to Tertiary sedimentary and volcanic rocks. The structurally highest units of the External Hellenides are unmetamorphosed and are tectonically separated from

high-pressure rocks on the Peleponnesos and Crete by the Cretan detachment (Thomson et al. 1999).

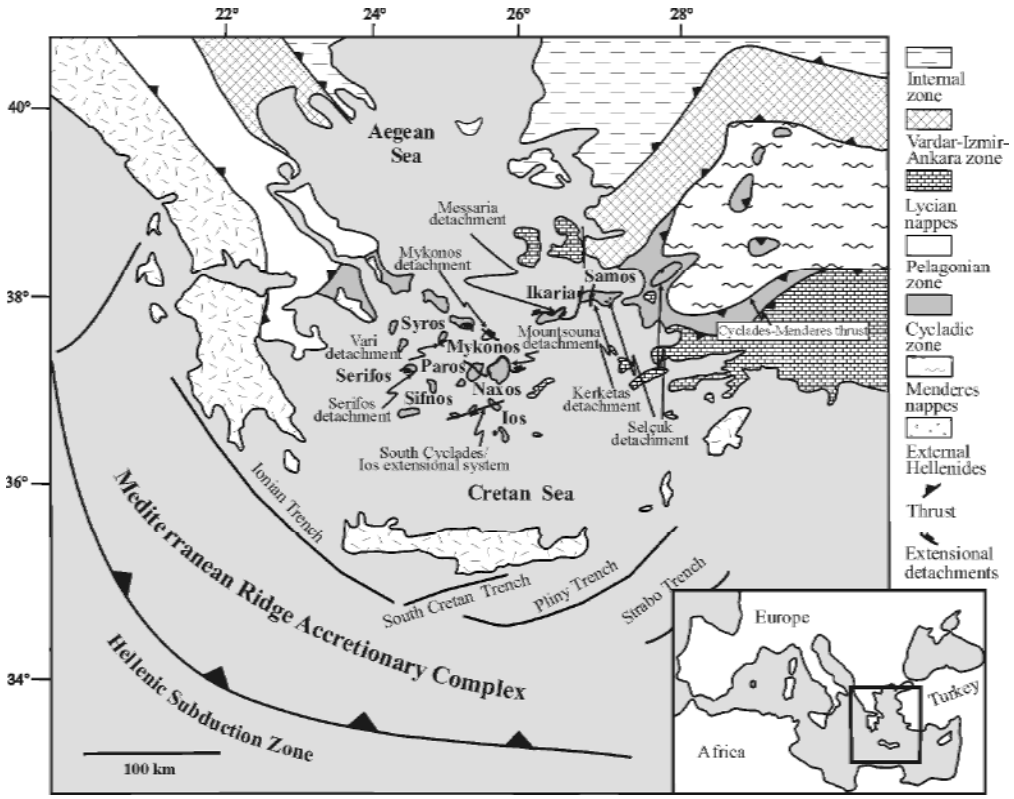

Fig. 1. Simplified tectonic map of the eastern Mediterranean showing the major tectonic units and the Hellenic subduction zone. Inset shows location of main map.

Geologic setting of western Turkey

The Cycladic blueschist unit in western Turkey is made up by the Selçuk nappe and the underlying Dilek nappe (Fig. 2) (Ring et al. 1999c). The ophiolitic Selçuk nappe consists of blocks of metagabbro, which are surrounded by a matrix of serpentinite and garnet-mica schist. The Dilek nappe is a Permo-Mesozoic shelf sequence, which includes a quartzite conglomerate with interlayered kyanite-chloritoid schist, metabasite, phyllite and marble containing partly metabauxite. The Carboniferous basement below the shelf sequence is missing in western Turkey.

Below the Cycladic blueschist unit are the Menderes nappes (Fig. 3), which show, instead of the External Hellenides in the Aegean, no Alpine high-pressure metamorphism (Ring et al. 1999c). An Eocene greenschist-facies shear zone, the so-called Cycladic-Menderes thrust, emplaced the high-pressure unit on top of the Menderes nappes, which are subdivided into four nappes (Fig. 3) (from top to bottom): (1) the Selimiye nappe, (2) the Çine nappe, (3) the

Bozdağ nappe, and (4) the Bayındır nappe (Ring et al. 1999c). The Selimiye nappe contains a metasedimentary sequence with Precambrian age in the basal part (Hetzel & Reischmann 1996). It is separated from the underlying Çine nappe by the Selimiye shear zone, which formed during prograde greenschist-facies metamorphism (Régnier 2003). The Çine nappe consists of amphibolite- to granulite-facies ortho- and paragneiss with intercalated metabasite, and the basement is of Proterozoic/Cambrian age (Hetzel & Reischmann 1996). The underlying Bozdağ nappe contains amphibolite-facies garnet-mica schist and metabasite. The Bayındır nappe at the base contains shelf sediments of Permo-Carboniferous age (Gessner et al. 2001), which were metamorphosed under lower greenschist-facies conditions at around 37 Ma (Lips 1998). The absence of Alpine high-pressure metamorphism and the lack of a well-defined subduction zone to the south of westernmost Turkey suggests that subduction ceased after the collision of the exotic Anatolide microcontinent in the Eocene (Ring et al. 1999c).

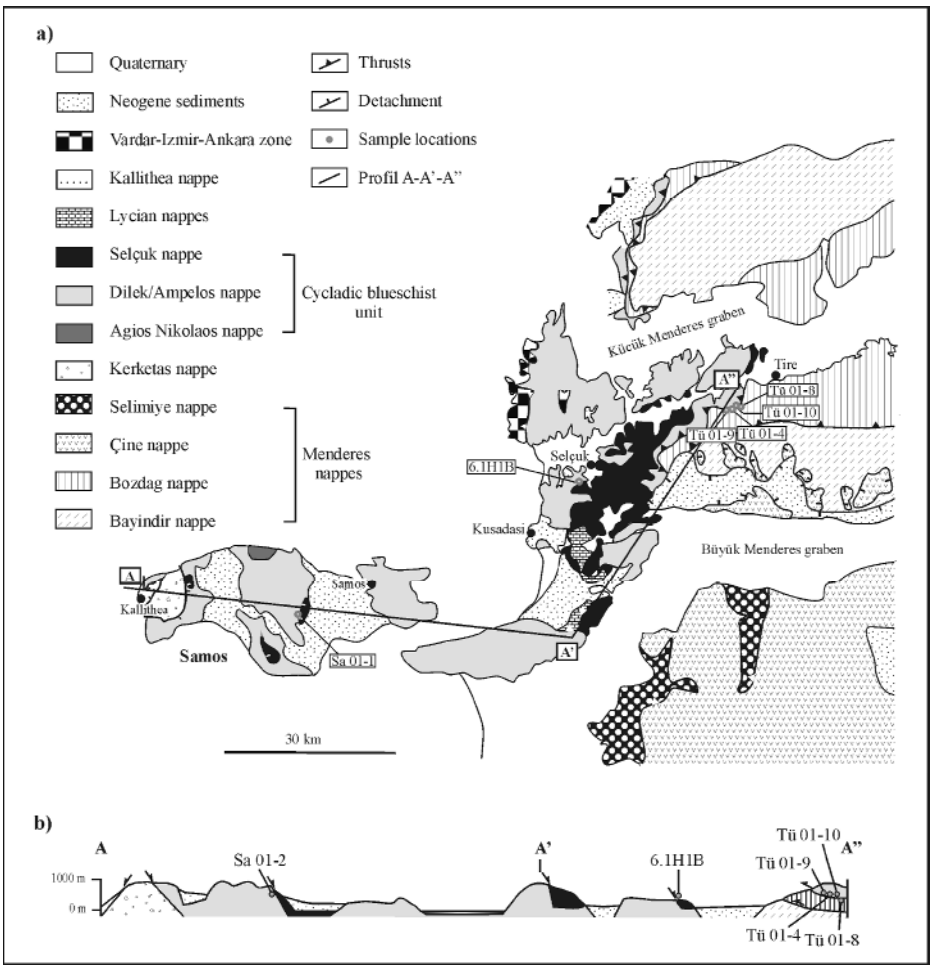

Fig. 2. (a) Tectonic map of western Turkey and Samos Island after Gessner et al. (2001). Shown are tectonic units, localities of geochronological samples and position of cross section A-A'-A''. (b) Schematic cross section A-A'-A'' of Samos Island and western Turkey showing localities of geochronological samples.

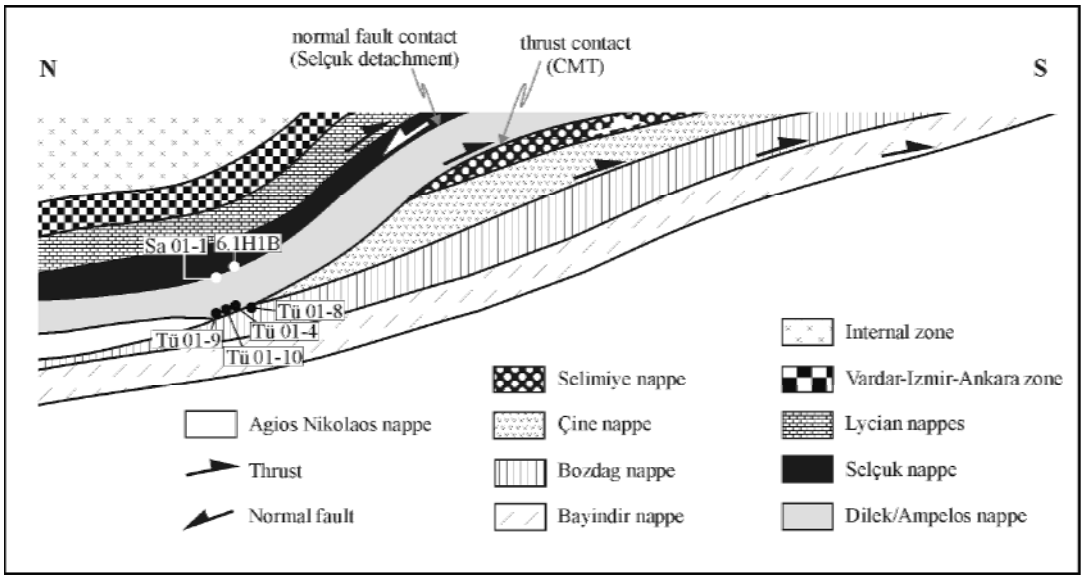

Fig. 3. Schematic sketch of the thrust sequence in western Turkey after Gessner et al. (2001). Shown are sample localities and the normal fault contact and the thrust contact (Cycladic-Menderes thrust, CMT).

The Cycladic blueschist unit in the Aegean and western Turkey

Ring et al. (1999b) showed that the Cycladic blueschist unit on Samos Island to the west of Turkey (Fig. 2) is represented by three high-pressure nappes, which are from top to bottom: (1) the Selçuk nappe (ophiolitic mélange), (2) the Ampelos nappe (Permo-Mesozoic shelf sequence), and (3) the Agios Nikolaos nappe (Carboniferous basement). The Selçuk nappe consists of blocks of metagabbro in a matrix of serpentinite and garnet-mica schist. Ring et al. (1999b) correlated the Selçuk nappe with the ophiolitic mélanges on the islands of Syros and Tinos (Okrusch & Bröcker 1990). The Ampelos nappe contains quartzite, metapelite and metabasite, which are overlain by metabauxite-bearing marble (Dürr et al. 1978) and has been interpreted as a former passive-continental margin sequence (Altherr & Seidel 1977). The Agios Nikolaos nappe consists of garnet-mica schist, which is intruded by Carboniferous orthogneiss and represents part of the former basement of the shelf sequence. The Selçuk nappe and the Ampelos nappe of Samos Island have the same lithology and protolith age as the Selçuk nappe and the underlying Dilek nappe of western Turkey and thus they have been correlated by Ring et al. (1999c).

The Selçuk nappe has P-T conditions of ~8 ± 2 kbar and ~410°C ± 40°C to ~480°C ± 80°C (Will pers. commun. 2004). The underlying Ampelos/Dilek nappe shows ~15 kbar and 500°C, and the Agios Nikolaos nappe ~19 kbar and ~550°C (Will et al. 1998).

Analytical procedure

Mineral analysis

We made microprobe work on the phengites in the mylonitic fabrics to determine the Si-content of the phengites and to see whether the phengites are chemically homogeneous (see later). For the chemical analysis we used a Jeol Superprobe (JXA 8900RL) at Johannes Gutenberg-Universität in Mainz, Germany. A complete set of mineral analyses is available in Table 1. Operating conditions were an acceleration voltage of 15 kV, a beam current of 15 nA and 20 s counting time per element. Standards used were wollastonite for Si, corundum for Al, pyrophanite for Ti, hematite for Fe, MgO for Mg, wollastonite for Ca, albite for Na, orthoclase for K, tugtupite for Cl, F-phlogopite for F, Cr_2O_3 for Cr, rhodochrosite for Mn, ZnS for Zn. The mineral analyses are considered to be accurate within a range of ~3% (relative) on any given grain.

$^{40}Ar/^{39}Ar$ dating procedure

For the $^{40}Ar/^{39}Ar$ dating phengite were degassed with a laser-probe using two procedures: (1) step-heating by increasing progressively the laser power, and (2) spot ablation on grains in sections. For the step-heating analyses, the phengite were separated under the binocular after coarse rock crushing, and then cleaned in ethanol and distilled water. For the spot ablation analyses, sections (~1 x 0.5 cm) were cut, polished on one side and afterwards cleaned in ethanol and distilled water. Both crystals and sections were packed in aluminium foil and irradiated for 70 hours in the McMaster nuclear reactor (Canada) with MMHb hornblende neutron flux monitor dated at 520.4 ± 1.7 Ma (Samson & Alexander 1987). After irradiation, the single grains and sections were placed on a Cu-holder inside an UHV gas extraction system and baked for 48 hours at 200°C. The analytical device consists of: (1) a multiline continuous 6 W argon-ion laser, (2) a beam shutter for selection of exposure times, (3) divergent and convergent lenses for definition of the beam diameter, which can produce a pit with a size varying from 50 to 100 μm in diameter for the spot fusion, (4) a CCD camera to monitor the experiments, (5) a small inlet line for the extraction and purification of gases and (6) a MAP 215-50 noble gas mass spectrometer.

The sections were placed on a copper plate, and the spot ablation was achieved using an exposure time of 30ms for each spot on the beam shutter. The single grains were placed in drilled cores and for the stepwise heating, they were exposed to the laser beam during 40s for each step. Heating for both techniques of analysis was made with a focussed or defocussed laser beam depending on the procedure chosen for degassing. Each analysis involves 5 min

for lasering and gas cleaning and 15 min for data acquisition by peak switching from mass 40 to 36, through 10 sets of data. System blanks were evaluated every three analyses and range around 2.10^{-12} cc for ^{40}Ar and 3.10^{-14} cc for ^{36}Ar. For each step-heating and spot ablation analyses, classical isotope corrections including blanks, mass discrimination radioactive decay of ^{37}Ar and ^{39}Ar and irradiation-induced mass interference were applied. The quoted errors represent one-sigma deviation and were calculated following McDougall and Harrison (1988).

$^{87}Rb/^{86}Sr$ dating procedure

For $^{87}Rb/^{86}Sr$ isotope analyses, mineral concentrates of all separable Sr-bearing phases were produced. For mineral separation we used small samples (<200 g) to avoid sampling of large-scale isotopic heterogeneities. White mica was separated into physically distinct subpopulations, following magnetic properties and grain size criteria, in order to detect possible Sr-isotopic inhomogeneity. Care was taken to avoid material altered by weathering or reflecting late-stage fluid-rock interaction. Mica sieve fractions were ground in pure ethanol in an agate mortar and then sieved in ethanol in order to obtain inclusion-free separates. All concentrates were purified by hand-picking under the binocular microscope. Whole rock powders were prepared in an agate mill.

Samples were analyzed for Rb and Sr contents by isotope dilution. They were weighed into Savillex® screw-top containers, spiked with a suitable mixed ^{87}Rb ,^{84}Sr spike solution, and dissolved in a mixture of HF and HNO_3. Solutions were processed by standard cation-exchange techniques. Determinations of Sr isotope ratios were carried out on a VG Sector 54 multicollector thermal ionisation mass spectrometer (GeoForschungsZentrum Potsdam) in dynamic mode. The values obtained for $^{87}Sr/^{86}Sr$ of the NBS standard SRM 987 during the period of analytical work was 0.710256 ± 0.000010 (n = 20). All isotopic ratios were normalized to an $^{86}Sr/^{88}Sr$ ratio of 0.1194. Rb analyses were done on the same mass spectrometer. The observed ratios were corrected for 0.25% per a.m.u. mass fractionation. Total procedural blanks were consistently below 0.15 ng for both Rb and Sr. Due to highly variable blank values, a useful blank correction is not applicable. For age calculations, an uncertainty of ± 1.5%, as derived from replicate analyses of natural mica samples, is assigned to the $^{87}Rb/^{86}Sr$ ratios. $^{87}Sr/^{86}Sr$ ratios are reported with their 2 sigma internal precision plus uncertainties from spike correction. For calculation of isochron parameters, a standard error of ± 0.005% for $^{87}Sr/^{86}Sr$ ratios was applied if individual errors were smaller than this value. This error estimate (2σ) was derived from reproducibility tests for Sr isotope ratios on spiked

samples. The program ISOPLOT/EX 2.01 (Ludwig 1999) was used to calculate regression lines and isochron parameters.

Structural data

Selçuk detachment

The Selçuk detachment is exposed on Samos Island and in western Turkey. It is a top-to-the-NE ductile extensional shear zone and separates the garnet-mica schist of the Selçuk nappe from the underlying kyanite-bearing calcschist of the Ampelos/Dilek nappe (Figs 1, 3). In Turkey, the contact is characterized by a foliation parallel to the contact and associated with a NE-trending lineation, which is expressed by stretched calcite-mica and kyanite laths (Gessner et al. 2001). In the garnet-mica schist of the Selçuk nappe garnet porphyroclasts form σ-shaped objects with strain shadows containing white mica and recrystallized quartz (Fig. 4).

On Samos Island, the Selçuk detachment is characterized by strongly sheared flaser gabbro of the Selçuk nappe. Diopside is partially replaced by glaucophane, which is transformed into blue-green calcic amphibole (Ring et al. 1999b). Kinematic indicators are characterized by the replacement of glaucophane to barroisite and supply a top-to-the-W shear sense. Sporadically, kinematic indicators supply a top-to the-E sense of shear. In rare cases, the barroiste is replaced by a later growth of actinolite. The stretching lineation is defined by elongated quartz and actinolite crystals, which have a variable orientation. Asymmetric strain shadows around amphibole porphyroblasts show a top-to-the ESE shear sense. The quartzite from the Ampelos nappe show intensely foliation made up by quartz, white mica, detrital zircon, ilmenite and traces of turmaline (Fig. 4).

Cycladic-Menderes thrust

The Cycladic-Menderes thrust (Figs 1, 3) separates the Cycladic blueschist unit from the underlying Menderes nappe pile. Thereby it cuts several nappes and defines an out-of-sequence ramp structure (Gessner et al. 2001). The Cycladic-Menderes thrust is a ~200 m thick shear zone and separates the Dilek nappe of the Cycladic blueschist unit from the underlying Bozdağ nappe of the Menderes nappes. The shear zone is divided into two parts, the upper ~100 m of the thrust contains marble and quartzite of the Dilek nappe, and the lower ~100 m consists of garnet-mica schist and amphibolite of the Bozdağ nappe. Amphibolite-facies top-N structures in the Bozdağ nappe were overprinted by the greenschist-

facies top-S shear zone and can correlated with the structures in the overlying Dilek nappe. The shear zone is characterized by increasing retrogression of biotite and garnet to chlorite, an increase in the number of cm- to dm-scale asymmetric folds, and the increasing occurrence of quartz veins towards the immediate contact of both nappes. Also shear bands and a S-trending stretching lineation expressed by elongated chlorite-white mica crystals were observed. In the lower ~100 m biotite and garnet are nearly completely retrogressed to chlorite, and the greenschist-facies mylonite indicates a top-to-the-S shear band-foliation, which can be observed across the Cycladic-Menderes thrust. Garnet show asymmetric strain shadows containing chlorite, white mica, biotite and recrystallized quartz and which developed during garnet breakdown (Fig. 4). In the upper ~100 m quartzite of the Dilek nappe show mylonitic foliation with SC'-type shear bands indicating top-to-the-S shear sense and a S-trending stretching lineation expressed by stretched chlorite, white mica and quartz crystals (Gessner et al. 2001). Also feldspar, biotite, which is partially chloritic, rutile and detrital zircon are observed. Mica is aligned in the penetrative foliation (Fig. 4).

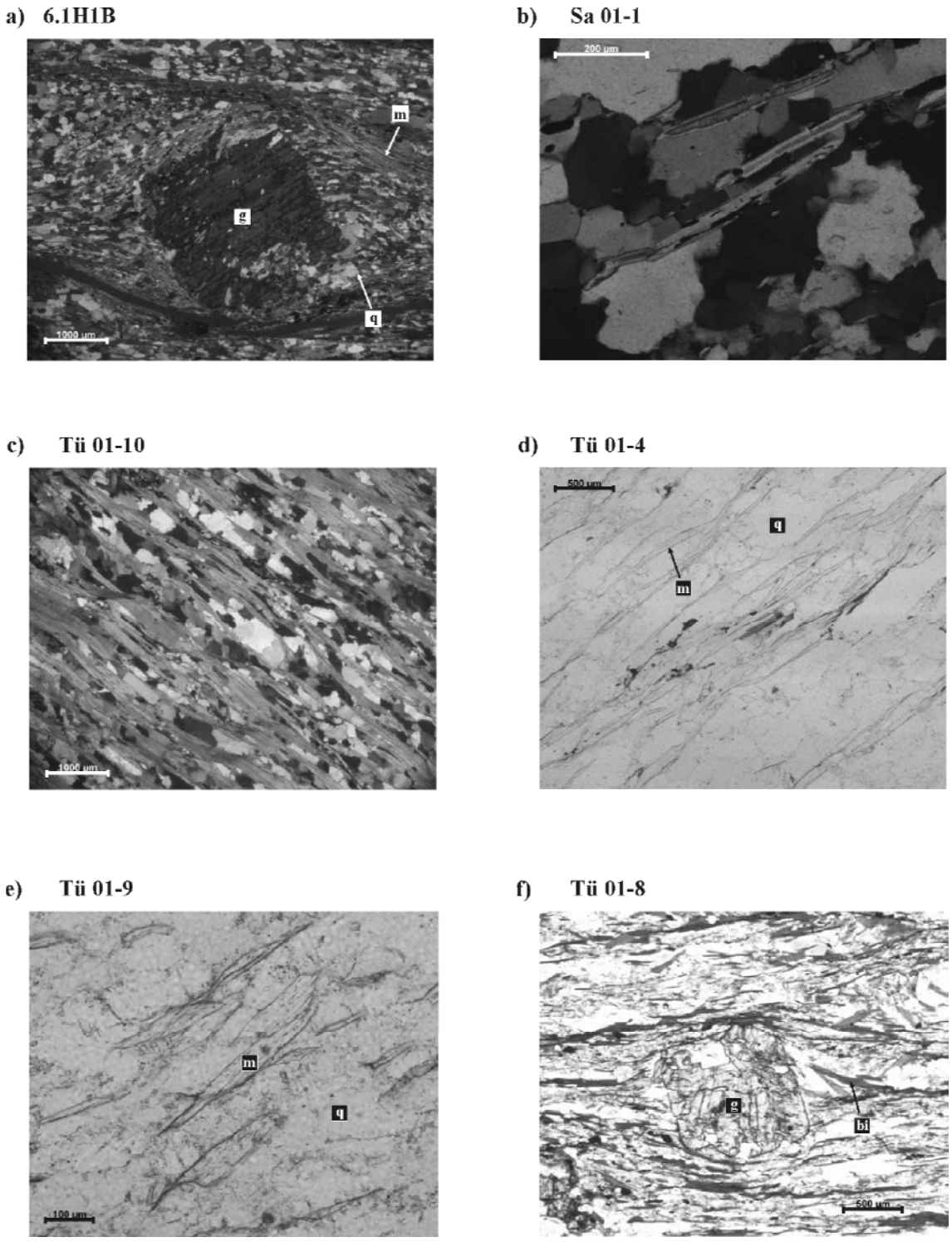

Fig. 4. Microphotographs of samples from the normal fault and thrust contact. (a) Sample 6.1H1B (normal fault contact) showing a rotated garnet with strain shadow containing recrystallized quartz and phengite (crossed nicols). (b) Sample Sa 01-1 (normal fault contact) and (c) sample Tü 01-10 (thrust contact) showing foliation represented by phengite and quartz (with subgrains) (crossed nicols). (d) Sample Tü 01-4 and (e) sample Tü 01-9 (both from thrust contact) showing also phengite and quartz grains indicating a foliation. (f) Sample Tü 01-8 (thrust contact) showing rotated garnet with inclusions and strain shadow containing recrystallized quartz and biotite. g = garnet, q = quartz, ph = phengite and bi = biotite.

Results of geochronological analysis

Six mylonite samples were used for $^{40}Ar/^{39}Ar$ and $^{87}Rb/^{86}Sr$ dating (Tables 2-4). The sample locations are illustrated in Figure 2. Two samples are from the mylonite zone of the Selçuk detachment and four samples are from the mylonite zone of the Cycladic-Menderes thrust (Fig. 3). In the following, the samples are first chemical, then the age data are presented and finally the ages are interpreted.

Mineral chemistry

Microprobe data, reported in Table 1 (Table 1 is situated at the end of this chapter), indicate that white mica in the samples is phengite. (Figs 5a, b). The Si content of the phengite from the upper mylonite zone is between 3.05 and 3.27 per formula unit (pfu) and from the lower mylonite zone between 3.00 and 3.39 pfu. The content of Al_{tot} is decreasing with increasing Si content. The Fe^{3+} content of phengite is low, as it plots along the celadonite/muscovite tie-line (Figs 5a, b). Phengite of the samples from the lower mylonite zone (Fig. 5a) indicate higher Fe^{3+} content than the phengite in the upper mylonite zone (Fig. 5b). In correspondence with high Si content, the amount of Na^{+} in the samples is low (Table 1). Element distribution maps for Na, Mg, K and Si of phengite from the samples depict homogeneous patterns. Microprobe mapping revealed no compositional zoning in the minerals.

In sample Sa 01-1 two populations of phengite were observed, which differ in their $^{87}Rb/^{86}Sr$-concentration (Table 4). Phengite in Tü 01-4, Tü 01-8, Tü 01-9 and Tü 01-10 show no evidence of a significant change in their crystal chemistry. This shows that chemically only one type of synkinematically recrystallized phengite occurs (Table 1, Figs 5a, b).

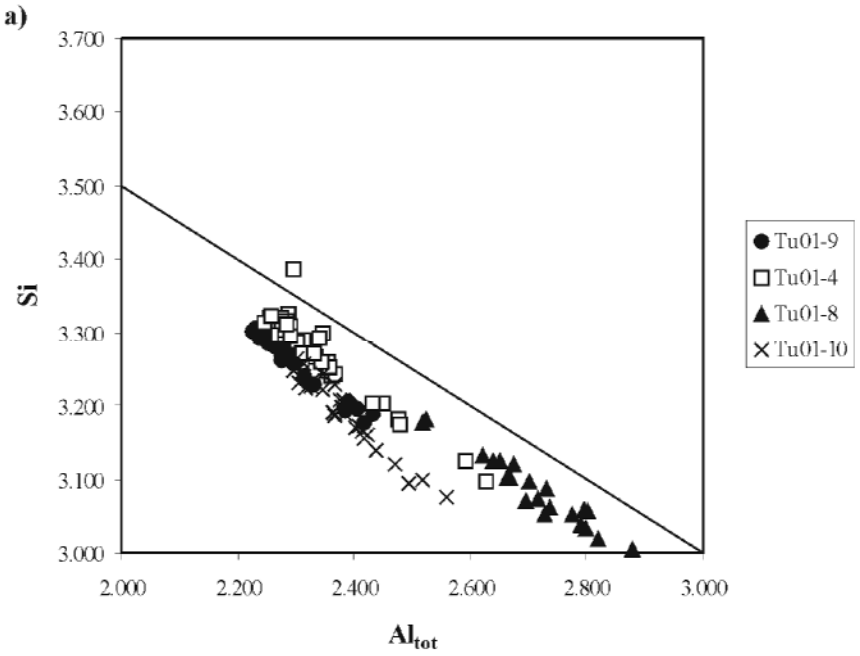

Fig. 5a. Si versus Al_{tot} (pfu) in phengite of samples Tü 01-4, Tü 01-8, Tü 01-9 and Tü 01-10 from the lower mylonite zone (thrust contact) in western Turkey. The line is demonstrating the celadonite/muscovite tie-line.

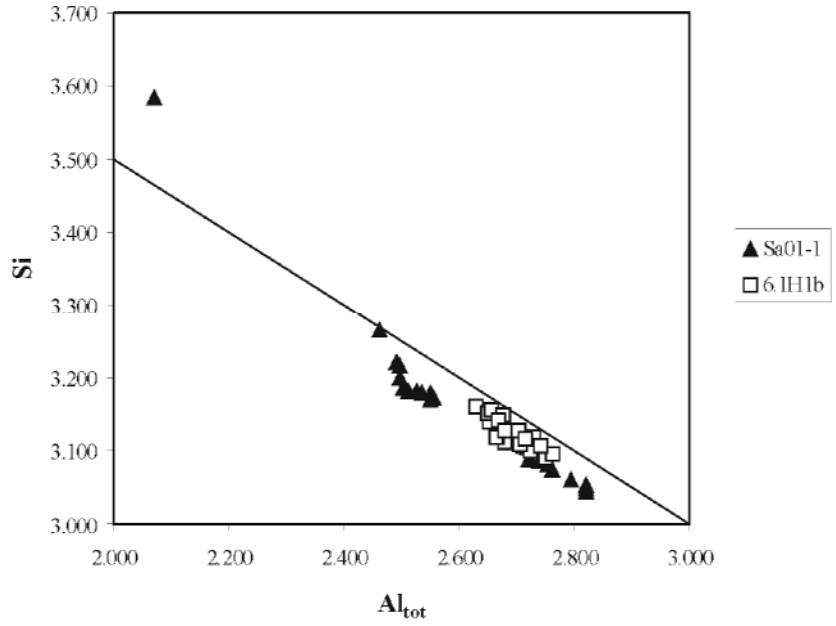

Fig. 5b. Si versus Al_{tot} (pfu) in phengite of samples Sa 01-1 and 6.1H1B from the upper mylonite zone (normal fault contact) on Samos Island and in western Turkey. The line is demonstrating the celadonite/muscovite tie-line.

Geochronology

$^{40}Ar/^{39}Ar$ data

Samples Sa 01-1 and 6.1H1B were only analyzed with the spot fusion technique. In each section six spots were analyzed. The ages for Sa 01-1 range from 36.9 ± 0.8 to 52.7 ± 1.9 Ma and have a weighted mean age of 41.5 ± 2.0 Ma (Table 2). The ages from 6.1H1B range from 31.3 ± 3.0 to 41.7 ± 1.2 Ma and show a weighted mean age of 35.3 ± 2.0 Ma (Table 2). The absolute frequency of the different ages (per section) is represented in histograms (Fig. 6).

Samples Tü 01-4, Tü 01-9 and Tü 01-10 were analyzed with the step-heating laser probe technique and give plateau ages of 38.6 ± 0.6 Ma for ~89% of released argon (Tü 01-4), 34.6 ± 0.9 Ma for ~95% of released argon (Tü 01-9), and 34.3 ± 0.6 Ma for ~88% of released argon (Tü 01-10) (Table 3, Fig. 7), respectively. The first heating step for each sample shows a large amount of atmospheric argon probably released from the surface or structural defects of the mineral at the beginning of degassing. Thus, these ages with large errors are to neglected. Spot fusion analyses have also been made on each sample, where per section between seven to eight spots were analyzed (Table 2). For sample Tü 01-4 the ages range from 30.9 ± 0.8 to 42.1 ± 1.5 Ma (weighted mean age of 36.4 ± 3.1 Ma), for sample Tü 01-9 from 28.5 ± 2.9 to 38.7 ± 1.3 Ma (weighted mean age of 35.5 ± 0.7 Ma), and for sample Tü 01-10 the ages range from 30.9 ± 1.7 to 40.8 ± 2.2 Ma (weighted mean age of 35.2 ± 0.7 Ma) (Table 2). The weighted mean ages are consistent with the age data obtained from the step-heating analysis. Sample Tü 01-8 was only analyzed by the spot fusion technique where seven spots were measured, which show ages from 29.8 ± 1.8 to 38.8 ± 2.3 Ma and a weighted mean age of 33.6 ± 1.8 Ma (Table 2). The absolute frequency of the different ages per section is represented in histograms (Fig. 6).

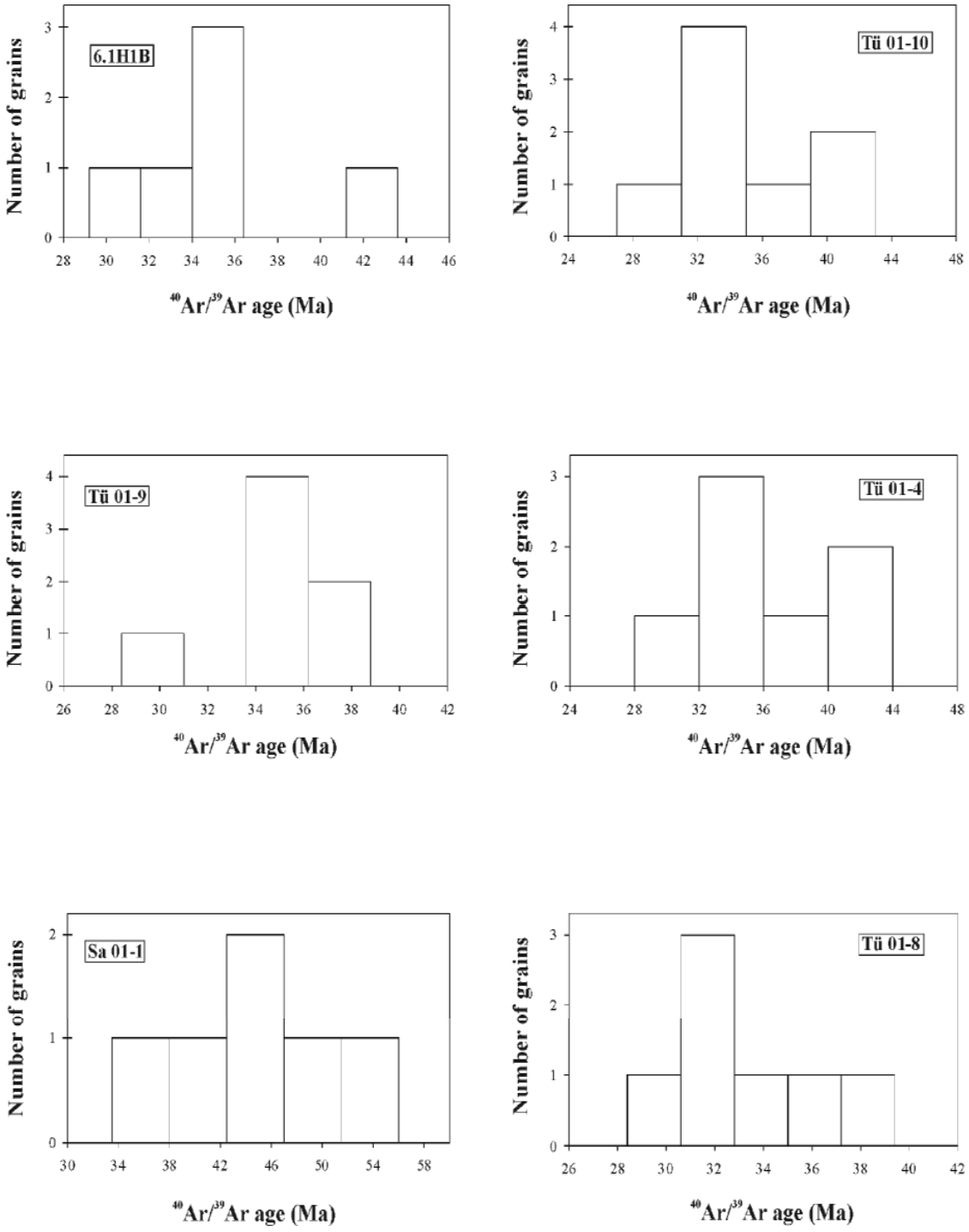

Fig. 6. $^{40}Ar/^{39}Ar$ spot fusion analyses. The absolute frequency of ages in the sections are represented in histograms.

Table 2. *$^{40}Ar/^{39}Ar$ analytical data (sections; spot fusion)*

Sample	Mineral No.	$^{40}Ar^*/^{39}Ar$	$^{36}Ar/^{40}Ar$ x 1000 J = 0.013337	$^{39}Ar/^{40}Ar$	$^{37}Ar/^{39}Ar$	% Atm	Age Ma	error 1σ
6.1H1B	1	1.487	0.014	0.6695	0.000	0.4	35.4	1.2
	2	1.501	0.034	0.6592	0.000	1.0	35.8	2.4
	3	1.752	0.389	0.5049	0.000	11.5	41.7	1.2
	4	1.434	0.244	0.6470	0.002	7.2	34.2	2.4
	5	1.414	0.038	0.6990	0.000	1.1	33.7	1.1
	6	1.313	0.468	0.6558	0.024	13.8	31.3	3.0
							35.3	**2.0**
Sa 01-1	1	2.223	0.272	0.4135	0.000	8.0	52.7	1.9
	2	1.857	0.600	0.4427	0.000	17.7	44.2	1.5
	3	1.550	0.584	0.5335	0.000	17.2	36.9	4.8
	4	1.774	0.312	0.5115	0.000	9.2	42.2	1.2
	5	1.800	0.181	0.5255	0.009	5.3	42.8	6.6
	6	2.143	0.258	0.4308	0.000	7.6	50.9	2.0
							41.5	**2.0**
Tü 01-9	1	1.194	0.682	0.6682	0.017	20.1	28.5	2.9
	2	1.443	0.154	0.6608	0.000	4.5	34.4	0.9
	3	1.625	0.057	0.6046	0.000	1.6	38.7	1.3
	4	1.543	0.060	0.6364	0.000	1.7	36.8	1.3
	5	1.450	0.132	0.6625	0.028	3.9	34.6	2.7
	6	1.423	0.102	0.6814	0.000	3.0	33.9	2.0
	7	1.445	0.082	0.6746	0.009	2.4	34.5	1.4
							35.5	**0.7**
Tü 01-10	1	1.716	0.040	0.5756	0.000	1.2	40.8	2.2
	2	1.493	0.028	0.6641	0.023	0.8	35.6	1.7
	3	1.400	0.027	0.7081	0.007	0.8	33.4	1.4
	4	1.359	0.009	0.7337	0.000	0.2	32.4	0.7
	5	1.671	0.013	0.5960	0.000	0.4	39.8	1.1
	6	1.449	0.286	0.6316	0.024	8.4	34.5	6.3
	7	1.295	0.037	0.7634	0.000	1.0	30.9	1.7
	8	1.449	0.027	0.6840	0.004	0.8	34.5	1.8
							35.2	**0.7**
Tü 01-8	1	1.310	1.280	0.4745	0.058	37.8	31.3	1.2
	2	1.429	0.732	0.5480	0.074	21.6	34.1	3.0
	3	1.341	0.984	0.5286	0.052	29.0	32.0	1.2
	4	1.351	0.977	0.5263	0.120	28.8	32.2	1.5
	5	1.628	0.906	0.4494	0.074	26.7	38.8	2.3
	6	1.551	1.033	0.4477	0.279	30.5	37.0	1.1
	7	1.250	1.210	0.5134	0.049	35.7	29.8	1.8
							33.6	**1.8**

Table 2. *$^{40}Ar/^{39}Ar$ analytical data (sections; spot fusion)*

Sample	Mineral No.	$^{40}Ar^*/^{39}Ar$	$^{36}Ar/^{40}Ar$ x 1000 J = 0.013337	$^{39}Ar/^{40}Ar$	$^{37}Ar/^{39}Ar$	% Atm	Age Ma	error 1σ
Tü 01-4	1	1.770	0.342	0.50760	0.021	10.1	42.1	1.5
	2	1.473	0.178	0.64270	0.061	5.2	35.1	1.9
	3	1.296	0.680	0.61640	0.019	20.0	30.9	0.8
	4	1.391	0.290	0.65690	0.035	8.5	33.2	1.9
	5	1.602	0.625	0.50830	0.000	18.4	38.2	5.5
	6	1.400	0.590	0.58940	0.000	17.4	33.4	2.2
	7	1.751	0.200	0.53700	0.000	5.9	41.7	4.7
							36.4	**3.1**

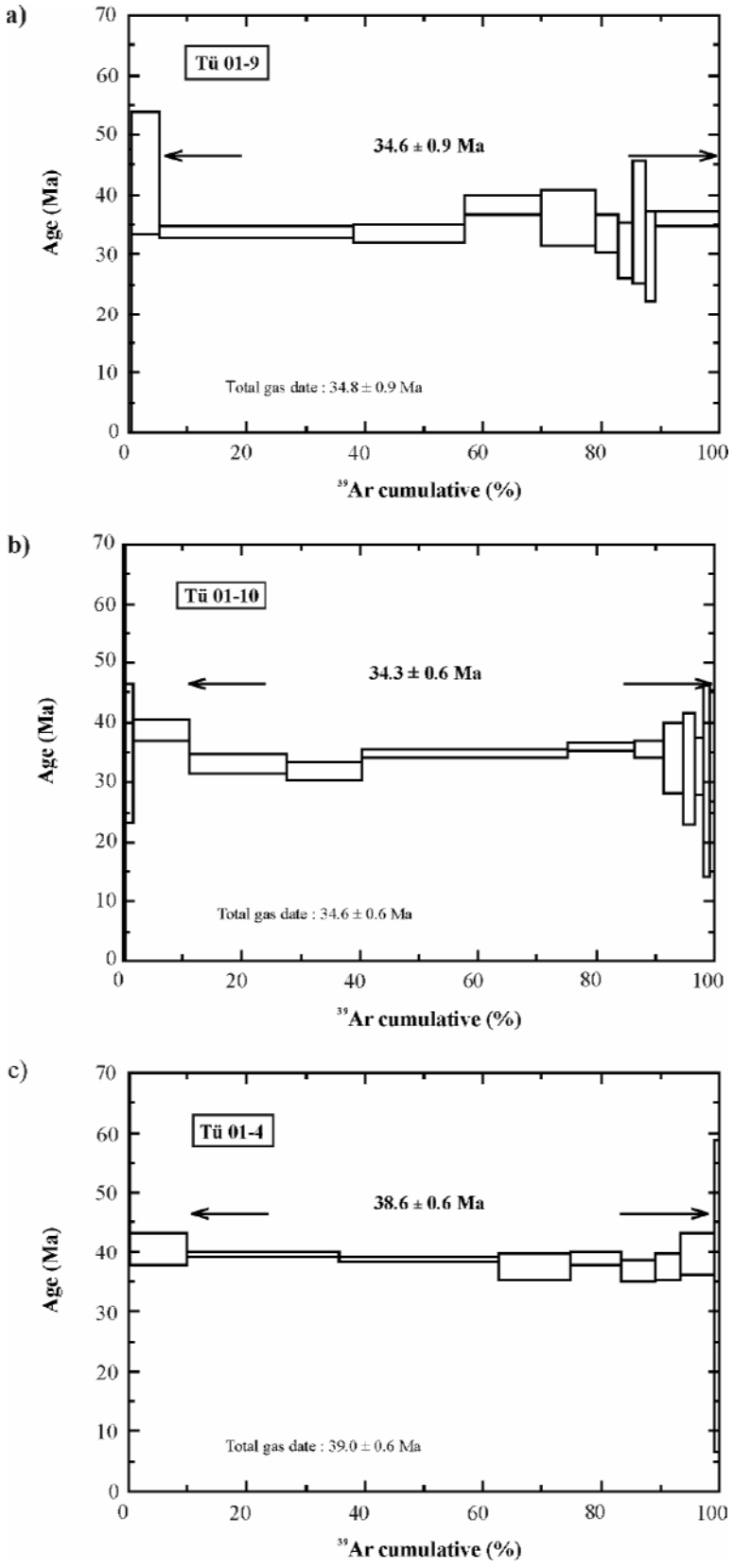

Fig. 7. $^{40}Ar/^{39}Ar$ step heating analyses. (a) $^{40}Ar/^{39}Ar$ age spectra for phengite from sample Tü 01-9, (b) phengite from sample Tü 01-10, and (c) phengite from sample Tü 01-4.

Table 3. *$^{40}Ar/^{39}Ar$ analytical data (step heating)*

Sample	Step No.	$^{40}Ar^*/^{39}Ar$	$^{36}Ar/^{40}Ar$ x 1000 J = 0.013337	$^{39}Ar/^{40}Ar$	$^{37}Ar/^{39}Ar$	% ^{39}Ar	% Atm	Age Ma	error 1σ
Tü 01-9	1	0.241	3.203	0.2215	0.463	0.6	94.6	41.9	5.8
	2	1.835	0.458	0.4708	0.394	5.1	13.5	43.6	10.1
	3	1.415	0.535	0.5946	0.012	38.2	15.8	33.7	0.9
	4	1.404	0.549	0.5963	0.017	56.8	16.2	33.5	1.5
	5	1.608	0.174	0.5895	0.002	69.8	5.1	38.3	1.7
	6	1.512	0.106	0.6403	0.000	79.1	3.1	36.0	4.6
	7	1.402	0.171	0.6768	0.000	82.9	5.0	33.4	3.2
	8	1.284	0.253	0.7203	0.080	85.4	7.4	30.6	4.7
	9	1.485	2.394	0.1967	0.000	87.4	70.7	35.4	10.2
	10	1.242	0.411	0.7066	0.000	89.1	12.1	29.7	7.6
	11	1.512	0.214	0.6190	0.021	100.0	6.3	36.0	1.2
							Total age = 34.8 ± 0.9		
Tü 01-10	1	1.778	2.725	0.1093	0.000	0.2	80.5	42.3	69.5
	2	1.461	0.327	0.6178	0.000	1.7	9.6	34.8	11.6
	3	1.626	0.297	0.5607	0.000	11.1	8.7	38.7	1.7
	4	1.393	0.396	0.6335	0.004	27.5	11.7	33.2	1.7
	5	1.337	0.512	0.6344	0.013	40.4	15.1	31.9	1.6
	6	1.464	0.072	0.6684	0.004	75.2	2.1	34.9	0.7
	7	1.509	0.030	0.6562	0.000	86.4	0.9	36.0	0.6
	8	1.493	0.068	0.6560	0.000	91.4	2.0	35.6	1.3
	9	1.431	0.203	0.6567	0.000	94.8	6.0	34.1	5.9
	10	1.350	0.212	0.6937	0.104	96.7	6.2	32.2	9.3
	11	1.374	0.251	0.6736	0.000	98.1	7.4	32.8	4.8
	12	1.264	0.320	0.7155	0.100	99.2	9.4	30.2	16.0
	13	1.515	0.420	0.5776	0.000	100.0	12.4	36.1	9.3
							Total age = 34.6 ± 0.7		
Tü 01-4	1	4.387	0.372	0.2028	0.000	0.3	11.0	102.6	22.6
	2	1.703	0.802	0.4477	0.000	9.8	23.7	40.5	2.8
	3	1.658	0.016	0.5999	0.000	35.6	0.5	39.5	0.4
	4	1.630	0.016	0.6104	0.000	62.7	0.4	38.8	0.4
	5	1.576	0.073	0.6206	0.004	75.0	2.1	37.5	2.2
	6	1.635	0.051	0.6021	0.000	83.5	1.5	38.9	1.1
	7	1.545	0.080	0.6316	0.000	89.2	2.3	36.8	1.7
	8	1.569	0.106	0.6171	0.000	93.4	3.1	37.4	2.2
	9	1.662	0.144	0.5757	0.000	99.2	4.2	39.6	3.5
	10	1.372	0.130	0.7005	0.000	110.0	3.8	32.7	26.2
							Total age = 39.0 ± 0.6		

$^{87}Rb/^{86}Sr$ data

We dated the mylonite sample Sa 01-1 from Samos Island and the mylonite samples Tü 01-4 and Tü 01-9 from western Turkey. The data, reported in Table 4 and illustrated in Figures 8a, b were obtained from whole-rock powder and hand-picked mineral separates. Sample Sa 01-1 yields an age of 37 ± 5 Ma. It shows indications of weathering and thus the data point for the whole rock can not be considered as dependable (Fig. 8a). The interpretation of the remaining data is also problematically because of the fine-grained white mica. If both populations of the white mica were late-synkinematically recrystallized, the age, defined by the white mica (35.24 ± 0.73 Ma, MSWD = 0.66), Sr(i) = 0.720522 ± 0.000086), could be interpreted as an age of late incremental deformation.

The ages of samples Tü 01-4 and Tü 01-9 are 34.4 ± 2.6 Ma (n = 6, MSWD = 6.2, Sr(i) = 0.70943 ± 0.00015) and 32.53 ± 0.38 Ma (n = 4, MSWD = 0.81, Sr(i) = 0.716403 ± 0.000035), respectively (Table 4). The data point for coarse-grained white mica (>500 µm) lies above the regression line of the other phases and the whole rock (Fig. 8b). This show that there is a small amount of white mica, which was incomplete synkinematically recrystallized during the last increment of deformation.

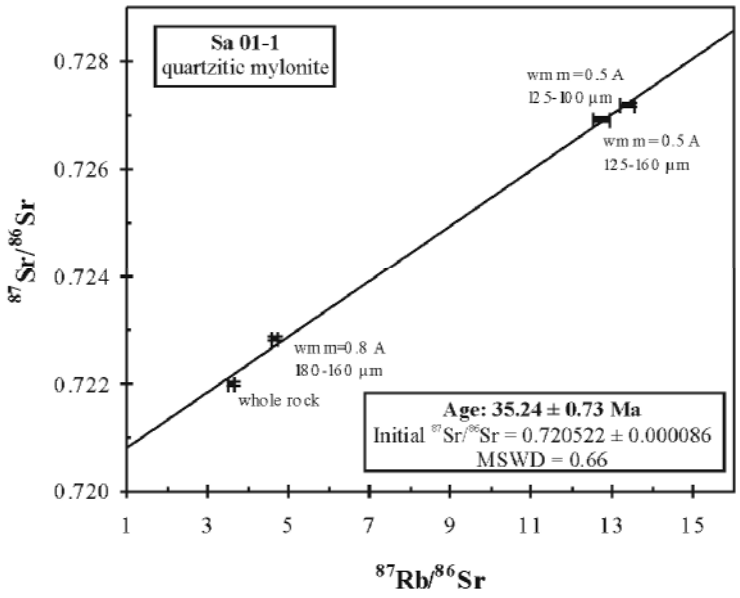

Fig. 8a. $^{87}Rb/^{86}Sr$ isochron diagram of sample Sa 01-1 from the upper normal fault contact on Samos Island.

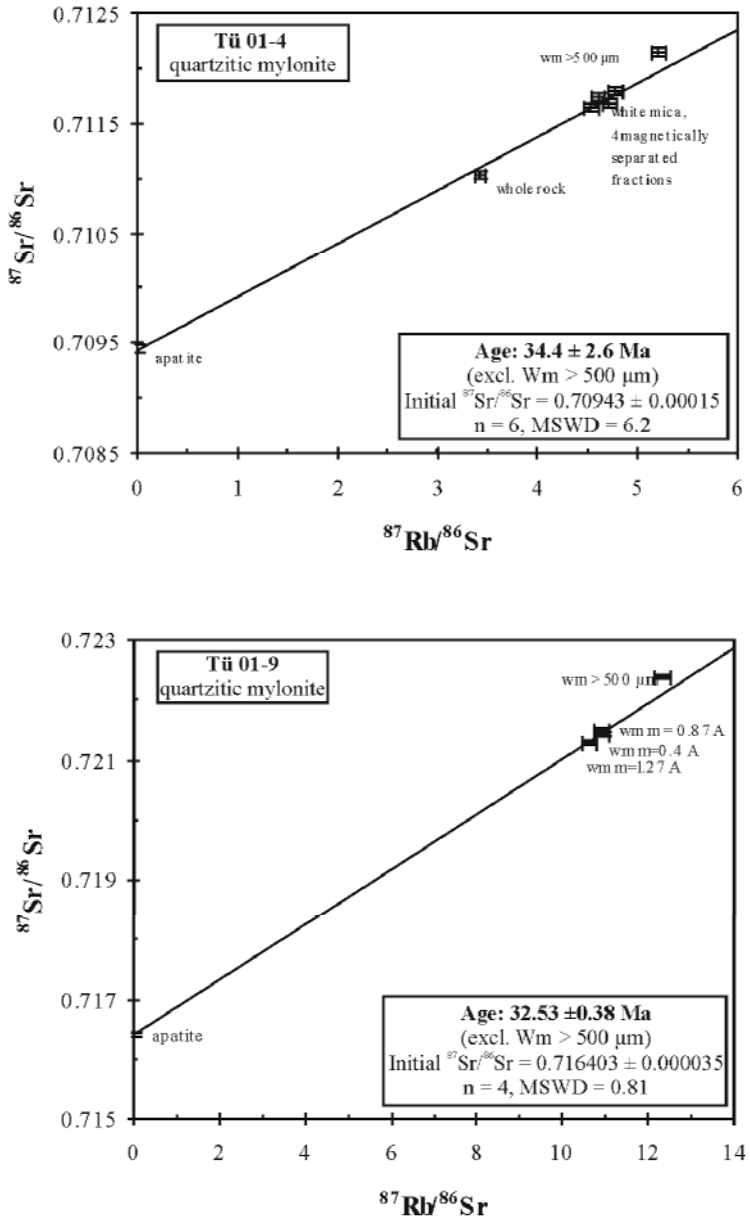

Fig. 8b. $^{87}Rb/^{86}Sr$ isochron diagrams of samples Tü 01-4 and Tü 01-9 from the lower thrust contact in western Turkey.

Table 4. *$^{87}Rb/^{86}Sr$ analytical data*

Sample/ Analysis No.	Material	Rb (ppm)	Sr (ppm)	$^{87}Rb/^{86}Sr$	$^{87}Sr/^{86}Sr$	$^{87}Sr/^{86}Sr$ $2\sigma_m$(%)
Tü 01-4 (34.4 ± 2.6 Ma; MSWD = 6.2, Sr = 0.70943 ± 0.00015)						
PS910	wm m = 0.8 A	206.5	129.7	4.609	0.711742	0.0014
PS911	wm m = 0.4 A	204.9	130.8	4.535	0.711651	0.0016
PS912	wm m = 2.2 A	204.9	124.3	4.773	0.711789	0.0016
PS913	wm > 500 µ m^x	216.1	120	5.210	0.712154	0.0012
PS914	apatite	0.68	1119	0.0017	0.709446	0.0016
PS962	whole rock	25.84	21.81	3.429	0.711026	0.0012
PS963	wm m = 1.3 A	207.4	127.4	4.713	0.711685	0.0014
Tü 01-9 (32.53 ± 0.38 Ma; MSWD = 0.81, Sr = 0.716403 ± 0.000035)						
PS915	wm > 500 µ m^x	223.7	52.54	12.34	0.722399	0.0014
PS916	wm m = 1.27 A	204.7	55.78	10.63	0.721302	0.0014
PS917	wm m = 0.4 A	221.3	58.64	10.93	0.721425	0.0012
PS919	apatite	0.94	1916	0.0014	0.716404	0.0012
PS964	wm m = 0.87 A	218.6	58.05	10.91	0.721487	0.0018
Sa 01-1 (35.24 ± 0.73 Ma; MSWD = 0.66, Sr = 0.720522 ± 0.000086)						
PS902	wm m = 0.8 A, 160-180 µ m	230.4	143.5	4.653	0.722851	0.0020
PS903	wm m = 0.5 A, 100-125 µ m	323.9	70.24	13.37	0.727183	0.0014
PS904	wm m = 0.5 A, 125-160 µ m	339.0	77.20	12.73	0.726923	0.0012
PS960	whole rock ^{x}	36.30	29.32	3.586	0.722015	0.0012

Errors are reported at the 2σm level. x: denotes analysis not used for age calculation. An uncertainty of ± 1.5% has to be assigned to Rb/Sr ratios. Abbreviations: wm: white mica; m: magnetic fraction (Frantz isodynamic separator, electric current as indicated, at 13° tilt as standard condition).

Data interpretation

A problem with interpreting phengite ages is determining an appropriate closure temperature. Given the temperatures and pressures as inferred from petrographic investigations in our samples, we follow the approach of Scaillet et al. (1992), Kirschner et al. (1996), and Villa (1998) and prefer a high closure temperature for phengite of ~500°-550°C. Scaillet et al. (1992) suggested that high Mg-phengites have higher closure temperatures of >550°C. Kirschner et al. (1996) supposed that phengites in metamorphic complexes can preserve multiple recrystallization and inferred a closure temperature of ~430°C. Villa (1998) showed that phengite can retain most or all of its Ar below 550°-580°C in the absence of subsequent greenschist-facies recrystallization. The combined U/Pb zircon and $^{40}Ar/^{39}Ar$ phengite/paragonite study of Tomaschek et al. (2003) strongly supports this conclusion. For rocks from Syros Island with peak metamorphic temperature of ~500°C, U/Pb dating of metamorphic zircon yielded the same age (52.4 ± 0.8 Ma) as $^{40}Ar/^{39}Ar$ dating on the white mica (52.3 ± 0.7 Ma). Other studies demonstrated that deformation and associated

recrystallization is much more efficient in resetting the isotope system than temperature (Freeman et al. 1997; Kühn et al. 2000). The given peak metamorphic temperatures for our study area did not exceed 500°-550°C, and given the rapid cooling of the nappes, our phengite ages date the recrystallization of phengite. Our $^{40}Ar/^{39}Ar$ age data of phengite yielded similar result as the $^{87}Rb/^{86}Sr$ data. The combined $^{40}Ar/^{39}Ar$ and $^{87}Rb/^{86}Sr$ phengite dating represents more or less the same age data for both contacts. The age data from the upper normal fault contact range from 35.3 ± 2.0 to 41.5 ± 2.0 Ma, and the ages from the lower thrust contact from 33.6 ± 1.8 to 38.6 ± 0.6 Ma.

Discussion

Pre-Miocene extensional faults correlated with an extrusion wedge

Our age data show that pre-Miocene extensional faults occur on Samos Island and western Turkey. The Selçuk nappe is separated from the underlying Ampelos/Dilek nappe by the Selçuk detachment and the Cycladic-Menderes thrust separates the Ampelos/Dilek nappe from the underlying Menderes nappe pile. Thrusting took place during the Late Eocene/Early Oligocene, coeval with normal faulting. The simultaneous age of both contacts and their opposite transport directions prove the existence of a Late Eocene/Early Oligocene extrusion wedge in western Turkey, which aided exhumation of the Cycladic blueschist unit in early orogenic phases. Evidence of early extensional faults was already discussed in the Aegean. Raouzaios et al. (1996) indicated that on the island of Sifnos normal faulting was operating between 28-34 Ma, at the same time as the Cycladic blueschist unit was thrust onto the Basal unit (Ring & Layer 2003). This thrusting at depth coupled with normal faulting at higher levels suggest the existence of an extrusion wedge in the Aegean formed during the Early Oligocene. Our results confirm the assumption made by Gessner et al. (2001) that an Eocene top-to-the-NE ductile extensional shear zone between the Dilek nappe and the overlying Selçuk nappe operated at the same time as the Dilek nappe was thrust top-to-the-S onto the underlying Menderes nappe pile in western Turkey.

Exhumation of the Cycladic blueschist unit

Gessner et al. (2001) supposed that the Cycladic blueschist unit must have been already exhumed from ~60 km depth up to ~30-40 km in the Middle to Late Eocene (37-43 Ma), which is attributed to the greenschist-facies overprinting of the upper part of the Menderes nappe pile after thrusting.

We assume for the whole Menderes nappe pile a pressure of ~6 kbar (for the Selimiye nappe; Régnier et al. 2003) and for the overlying Dilek nappe a pressure of ~15 kbar (Will et al. 1998) (Fig. 9). The pressure difference of ~9 kbar between the two tectonic units demonstrates that the Dilek nappe was already exhumed by ~35 km at the time the nappe was thrust onto the underlying Menderes nappes. The pressure difference of ~7 kbar between the Selçuk nappe (8 kbar, Will pers. commun. 2004) and the Dilek nappe shows that latter nappe was exhumed of ~25 km by the normal fault contact at the same time (Fig. 9). The last few kilometer of exhumation of the Cycladic blueschist unit can not only be explained by the normal fault contact between the Selçuk nappe and the underlying Ampelos/Dilek nappe and the thrust contact between latter nappe and the underlying Menderes nappes.

We suggest that the top-to-the-NE detachment between the Selçuk nappe and the overlying Lycian nappes could exhume the remaining ~5-10 km of the Cycladic blueschist unit. During the Late Cretaceous the Lycian nappe complex was translated top-to-the-S (Rimmelé et al. 2003) over the Cycladic blueschist unit. From the Middle Eocene until the Early Oligocene the contact between the two different tectonic units was reactivated as a top-to-the-NE shear zone during retrogression of high-pressure mineral parageneses. This shear zone allowed the exhumation of the Lycian rocks from a depth of ~30 km (Rimmelé et al. 2003). As present studies indicate, are the Lycian nappes and the Selçuk nappe also exposed on the Cycladic island of Amorgos and separated from one another by a detachment (Rosenbaum pers. commun. 2004), which can be associated with the top-to-the-NE detachment in western Turkey.

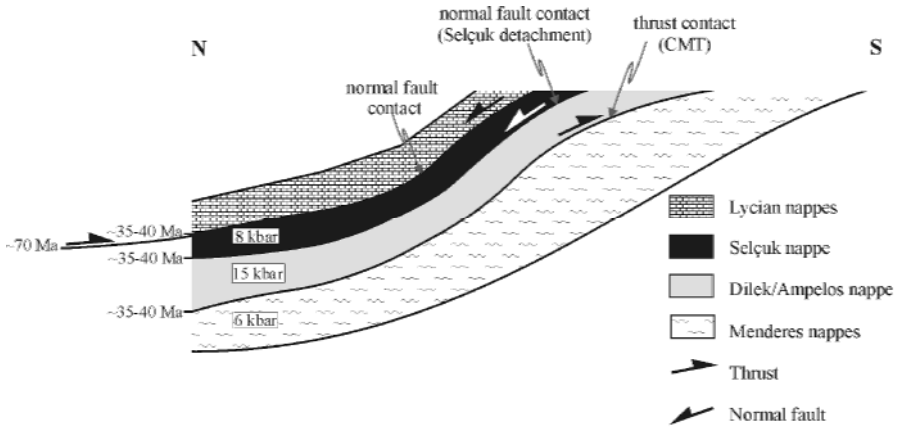

Fig. 9. Schematic sketch showing the exhumation history of the Cycladic blueschist unit. Indicated are the pressure conditions of the different nappes and the operating time scale of the normal fault and thrust contacts. CMT = Cycladic-Menderes thrust.

Conclusions

Similar geochronological $^{40}Ar/^{39}Ar$ and $^{87}Rb/^{86}Sr$ data suggest that thrusting of the high-pressure rocks of the Cyclades onto the non-high-pressure rocks of the Menderes nappes is coeval with the initial extensional movements by normal faulting in the hangingwall of the Cycladic blueschist unit. This argues for the existence of a Late Eocene/Early Oligocene extrusion wedge, which aided ~30-35 km to the exhumation of the Ampelos/Dilek nappe of the Cycladic blueschist unit to the Earth's surface.

References

ALLEGRE ET AL. 1984. Structure and evolution of the Himalaya-Tibet orogenic belt. *Nature*, **307**, 17-31.

ALTHERR, R. & SEIDEL, E. 1977. Speculations on the geodynamic evolution of the Attic-Cycladic crystalline complex during alpidic times. *In*: Kallergis, G. (ed.) Geology of the Aegean region, Proceedings VI Colloquium, Athens. Institute of Geology and Mineral Exploration, 347-351.

AVIGAD, D. & GARFUNKEL, T. 1989. Low-angle faults above and below a blueschist belt-Tinos Island, Cyclades, Greece. *Terra Nova*, **1**, 182-187.

AVIGAD, D., GARFUNKEL, Z., JOLIVET, L. & AZAÑÓN, J.M. 1997. Back-arc extension and denudation of Mediterranean eclogites. *Tectonics*, **16**, 924-941.

BERNOULLI, D., DE GRACIANSKY, P.C. & MONOD, O. 1974. The extension of the Lycian nappes (SW Turkey) into the southeastern Aegean islands. *Eclogae geol. Helv*., **67**, 39-90.

BUICK, I.S. 1991. Mylonite fabric development on Naxos, Greece. *Journal of Structural Geology*, **13** (6), 643-655.

BURCHFIEL, B.C. & ROYDEN, L.H. 1985. North-South extension within the convergent Himalayan region. *Geology*, **13**, 679-682.

COLLINS, A.S & ROBERTSON, A.H.F. 1997. Lycian mélange, southwest Turkey: An emplaced Cretaceous accretionary complex. *Geology*, **25**, 255-258.

DÜRR, S., ALTHERR, R., KELLER, J., OKRUSCH, M. & SEIDEL, E. 1978. The Median Aegean Crystalline Belt: Stratigraphy, structure, metamorphism, magmatism. *In*: Alps, Apennines, Hellenides, Cloos, H., Roeder, D. & Schmidt, K., E. Schweizerbart'sche Verlagsbuchhandlung, Stuttgart, 455-477.

FRANZ, L. & OKRUSCH, M. 1992. Aragonite-bearing blueschists on Arki Island, Dodekanese, Greece. European Journal of Mineralogy, **4**, 527-537.

FREEMAN, S.R., INGER, S., BUTLER, R.W.H. & CLIFF, R.A. 1997. Dating deformation using Rb-Sr in white mica: Greenschist facies deformation ages from the Entrelor shear zone, Italian Alps, *Tectonics*, **216**, 57-76.

GESSNER, K., RING, U. PASSCHIER, C.W. & GÜNGÖR, T. 2001. How to resist subduction: evidence for large-scale out-of-sequence thrusting during Eocene collision in western Turkey. *Journal of the Geological Society, London*, **158**, 769-784.

GÜNGÖR, T. & ERDOGAN, B. 2001. Emplacement age and direction of the Lycian nappes in the Söke-Selçuk region, western Turkey. *International Journal of Earth Science*, **89**, 870-882.

HETZEL, R. & REISCHMANN, T. 1996. Intrusion age of Pan-African augen gneisses in the southern Menderes Massif and the age of cooling after Alpine ductile extensional deformation. *Geologisches Magazin*, 565-572.

HODGES, K.V., PARRISH, R.R., HOUSH, T.B., LUX, D.R., BURCHFIELD, B.C., ROYDEN, L.H. & CHEN, Z. 1992. Simultaneous Miocene extension and shortening in the Himalayan orogen. *Science*, **258**, 1466-1470.

KIRSCHNER, D.L., COSCA, M.A., MASSON, H. & HUNZIKER, J.C. 1996. Staircase $^{40}Ar/^{39}Ar$ spectra of fine-grained white mica: Timing and duration of deformation and empirical constraints on argon diffusion. *Geology*, **24**, 747-750.

KÜHN, A., GLODNY, J., IDEN, K. & AUSTRHEIM, A. 2000. Retention of Precambrian Rb/Sr phlogopite ages through Caledonian eclogite facies metamorphism, Bergen Arc Complex, W-Norway. *Lithos*, **51**, 305-330.

KUMERICS, C., RING, U., BRICHAU, S., RÉGNIER, J.L. & GLODNY, J. 2004. The extensional Messaria shear zone and associated brittle detachments faults, Aegean Sea, Greece. *Journal of Geological Society of London*, (submitted).

LEE, J. & LISTER, G.S. 1992. Late Miocene ductile extension and detachment faulting, Mykonos, Greece. *Geology*, **20**, 121-124.

LIPS, A.L.W. 1998. Temporal constraints on the kinematics of the destabilization of an orogen; syn- to post-orogenic collapse of the Northern Aegean region. *Geol. Ultraiect*., **166**, 223p.

LISTER, G.S., BANGA, G. & FEENSTRA, A. 1984. Metamorphic core complexes of Cordilleran type in the Cyclades, Aegean Sea, Greece. *Geology*, **12**, 221-225.

LISTER, G.S. & FORSTER, M. 1996. Inside the Aegean metamorphic core complexes. *Technical Publications Australian Crustal Research Centr*e, **45**, 110p.

LUDWIG, K.R. 1999. Using Isoplot/Ex, Version 2.01: a geochronological toolkit for Microsoft Excel. *Berkeley Geochronology Center Special Publication*, **1a**, 47p.

MCDOUGALL, I. & HARRISON, T.M. 1988. Geochronology and Thermochronology by the $^{40}Ar/^{39}Ar$ method. *Oxford University Press*, *New York*, 212p.

MURPHY, M.A. & HARRISON, T.M. 1999. Relationship between leucogranites and the Qomolangma detachment in the Rongbuk Valley, south Tibet. *Geology*, **27**, 831-834.

OKRUSCH, M. & BRÖCKER, M. 1990. Eclogite facies rocks in the Cycladic blueschist belt, Greece: A review. *European Journal of Mineralogy*, **2**, 451-478.

RAOUZAIOS, A., LISTER, G.S. & FOSTER, D.A. 1996. Oligocene exhumation and metamorphism of eclogite-blueschists from the island of Sifnos, Cyclades, Greece. *Geological Society of Australia Bulletin*, **41**, 358p.

RÉGNIER, J.L., RING, U., PASSCHIER, C.W., GESSNER, K. & GÜNGÖR, T. 2003. Contrasting metamorphic evolution of metasedimentary rocks from the Çine and Selimiye nappes in the Anatolide belt, western Turkey. *Journal of Metamorphic Geology*, **21**, 1-23.

RIMMELÉ, G., JOLIVET, L., OBERHÄNSLI, R. & GOFFÉ, B. 2003. Deformation history of the high-pressure Lycian Nappes and implications for tectonic evolution of SW Turkey. *Tectonics*, **22** (2), 1007 (doi: 10.1029/2001TC901041).

RIMMELÉ, G., OBERHÄNSLI, R., GOFFÉ, B., JOLIVET, L., CANDAN, O. & ÇETINKAPLAN, M. 2003. First evidence of high-pressure metamorphism in the "Cover Series" of the southern Menderes Massif. Tectonic and metamorphic implications for the evolution of SW Turkey. *Lithos*, **71**, 19-46.

RING, U., LAWS, S. & BERNET, M. 1999b. Structural analysis of a complex nappe sequence and late-orogenic basins from the Aegean Island of Samos, Greece. *Journal of Structural Geology*, **21**, 1575-1601.

RING, U., GESSNER, K., GÜNGÖR, T. & PASSCHIER, C.W. 1999c. The Menderes Massif of western Turkey and the cycladic massif in the Aegean – do they really correlate? *Journal of Geological Society*, **156**, 3-6.

RING, U., THOMSON, S.N. & BRÖCKER, M. 2003a. Fast extension but little exhumation: the Vari detachment in the Cyclades, Greece. *Geological Magazine*, **140**, 245-252.

RING, U. & LAYER, P.W. 2003. High-pressure metamorphism in the Aegean, eastern Mediterranean: Underplating and exhumation from the Late Cretaceous until the Miocene to Recent above the retreating Hellenic subduction zone. *Tectonics*, **22** (3),1022, doi: 10.1029/2001ITC001350, 23p.

ROYDEN, L. 1993. The tectonic expression of slab pull at continental convergent boundaries. *Tectonics*, 12, 303-325.

SAMSON, S.C. & ALEXANDER, E.C. 1987. Calibration of the interlaboratory 40Ar/39Ar dating standard MMHb-1. *Chemical Geology*, **66**, 27-34.

SCAILLET, S., FERAUD, G., BALLEVRE, M. & AMOURIE, M. 1992. Mg/Fe and [(Mg,Fe)Si-Al_2] compositional controlon argon behaviour in high-pressure white micas: A $^{40}Ar/^{39}Ar$ continuous laser-probe study from the Dora-Maira nappe of the internal western Alps, Italy. *Geochim. Cosmochim. Acta*, **56**, 2851-2872.

ŞENGÖR, A.M.C. & YILMAZ, Y. 1981. Tethyan evolution of Turkey: a plate tectonic approach. *Tectonophysics*, **75**, 181–241.

SHERLOCK, S., KELLEY, S., INGER, S., HARRIS, N. & OKAY, A. 1999. ^{40}Ar-^{39}Ar and Rb-Sr geochronology of high-pressure metamorphism and exhumation history of the Tavsanli Zone, NW Turkey. *Contribution to Mineralogy and Petrology*, **137**, 46-58.

THOMSON, S.N., STÖCKHERT, B. & BRIX, M.A. 1998. Thermochronology of the high-pressure metamorphic rocks of Crete, Greece: Implications for the speed of tectonic processes. *Geology*, **26**, 259-262.

THOMSON, S.N., STÖCKHERT, B. & BRIX, M.A. 1999. Miocene high-pressure metamorphic rocks of Crete, Greece: rapid exhumation by buoyant escape, *In*: Exhumation processes: Normal faulting, Ductile Flow and Erosion (eds Ring, U. et al.). *Geological Society of London, Special Publication*, **154**, 87-107.

TOMASCHEK, F., KENNEDY, A., VILLA, I.M. & BALLHAUS, C. 2003. Zircons from Syros, Cyclades, Greece- Recrystallization and mobilisation during high pressure metamorphism. *Journal of Petrology*, **44**, 1977-2002.

VANDENBERG, L.C. & LISTER, G.S. 1996. Structural analysis of basement tectonites from the Aegean metamorphic core complex of Ios, Cyclades, Greece. *Journal of Structural Geology*, **18**, 1437-1454.

VILLA, I. 1998. Isotopic closure. *Terra Nova*, **10**, 42-47.

WIJBRANS; J.R. & MCDOUGALL, I. 1986. $^{40}Ar/^{39}Ar$ dating of white micas from an Alpine high-pressure metamorphic belt on Naxos (Greece): The resetting of the argon isotopic system. *Contribution to Mineralogy and Petrology*, **93**, 187-194.

WILL, T., OKRUSCH, M., SCHMÄDICKE, E. & CHEN, G. 1998. Phase relations in the greenschist-blueschist-amphibolite-eclogite facies in the system Na_2O-CaO-FeO-MgO-Al_2O_3-SiO_2-H_2O (NCFMASH), with application to metamorphic rocks from Samos, Greece. *Contributions to Mineralogy and Petrology*, **132**, 85-102.

Table 1. White *mica analyses*

Sa 01-1																									
SiO_2	47.830	48.160	47.730	48.670	47.810	55.840	47.790	59.620	47.760	48.400	47.580	47.770	47.560	46.700	47.270	47.240	46.270	46.410	46.010	46.450	47.730	46.540	46.340	47.090	46.740	45.680
$Al2O_3$	32.370	32.120	32.500	31.930	32.030	27.370	30.590	25.250	32.200	31.860	32.530	31.620	32.450	34.210	34.370	34.710	36.280	36.490	34.180	34.770	34.490	35.050	35.120	34.880	33.580	35.860
TiO_2	0.152	0.245	0.174	0.107	0.191	0.113	0.189	0.074	0.144	0.153	0.118	0.168	0.141	0.111	0.151	0.114	0.133	0.129	0.099	0.041	0.124	0.135	0.072	0.074	0.117	0.122
Cr_2O_3	0.000	0.000	0.024	0.000	0.051	0.037	0.000	0.020	0.025	0.000	0.057	0.021	0.000	0.066	0.131	0.000	0.062	0.076	0.080	0.110	0.066	0.099	0.025	0.103	0.096	0.025
MgO	1.179	1.309	1.190	1.142	1.225	1.032	0.828	0.911	1.217	1.245	1.173	1.329	1.214	0.850	1.047	1.083	0.515	0.580	0.950	0.896	0.757	0.762	0.739	1.011	1.029	0.561
FeO	4.060	4.530	4.230	4.210	4.270	3.880	4.080	3.400	4.180	4.030	3.890	4.120	4.090	2.490	2.440	2.340	2.220	2.210	2.220	2.610	2.420	2.600	2.480	2.270	2.520	2.350
MnO	0.029	0.000	0.000	0.000	0.000	0.009	0.013	0.043	0.000	0.000	0.011	0.007	0.014	0.000	0.013	0.050	0.056	0.034	0.009	0.013	0.000	0.007	0.063	0.047	0.010	0.000
CaO	0.080	0.000	0.071	0.000	0.012	0.020	0.039	0.000	0.000	0.021	0.000	0.010	0.000	0.000	0.000	0.024	0.017	0.007	0.014	0.000	0.010	0.016	0.010	0.000	0.000	0.021
BaO	0.087	0.242	0.192	0.126	0.320	0.193	0.083	0.233	0.000	0.134	0.354	0.095	0.183	0.237	0.228	0.211	0.342	0.185	0.328	0.090	0.291	0.094	0.160	0.378	0.000	0.053
Na_2O	0.840	0.692	0.635	0.684	0.706	0.671	0.474	0.684	0.731	0.762	0.794	0.510	0.683	1.100	1.005	0.999	1.410	1.450	1.053	1.071	1.312	1.170	1.420	1.047	1.060	1.321
K_2O	9.530	9.730	9.270	9.660	9.700	8.810	8.900	8.150	9.740	9.570	9.620	9.950	9.620	9.240	9.250	9.010	8.760	8.860	9.130	9.430	8.850	9.260	8.960	9.190	9.210	8.950
Total	96.232	97.061	96.021	96.601	96.425	97.975	93.068	98.385	96.078	96.175	96.136	95.678	96.034	95.009	96.065	96.004	96.065	96.501	94.085	95.585	96.192	95.803	95.431	96.180	94.408	94.971
Cations per 22 oxygens																										
Si^{4+}	3.179	3.186	3.178	3.221	3.182	3.583	3.265	3.765	3.181	3.217	3.172	3.199	3.170	3.122	3.120	3.111	3.053	3.045	3.105	3.089	3.139	3.085	3.082	3.106	3.139	3.048
Al^{IV}	0.821	0.814	0.822	0.779	0.818	0.417	0.735	0.235	0.819	0.783	0.828	0.801	0.830	0.878	0.880	0.889	0.947	0.955	0.895	0.911	0.861	0.915	0.918	0.894	0.861	0.952
Al^{VI}	1.715	1.691	1.729	1.711	1.694	1.653	1.728	1.644	1.709	1.713	1.729	1.695	1.720	1.818	1.793	1.805	1.874	1.866	1.824	1.813	1.813	1.823	1.835	1.817	1.797	1.868
Ti^{4+}	0.008	0.012	0.009	0.005	0.010	0.005	0.010	0.004	0.007	0.008	0.006	0.008	0.007	0.006	0.007	0.006	0.007	0.006	0.005	0.002	0.006	0.007	0.004	0.004	0.006	0.006
Cr^{3+}	0.000	0.000	0.001	0.000	0.003	0.002	0.000	0.001	0.001	0.000	0.003	0.001	0.000	0.003	0.007	0.000	0.003	0.004	0.004	0.006	0.003	0.005	0.001	0.005	0.005	0.001
Mg^{2+}	0.117	0.129	0.118	0.113	0.122	0.099	0.084	0.086	0.121	0.123	0.117	0.133	0.121	0.085	0.103	0.106	0.051	0.057	0.096	0.089	0.074	0.075	0.073	0.099	0.103	0.056
Fe^{2+}	0.226	0.251	0.236	0.233	0.238	0.208	0.233	0.180	0.233	0.224	0.217	0.231	0.228	0.139	0.135	0.129	0.122	0.121	0.125	0.145	0.133	0.144	0.138	0.125	0.142	0.131
Mn^{2+}	0.002	0.000	0.000	0.000	0.000	0.000	0.001	0.002	0.000	0.000	0.001	0.000	0.001	0.000	0.001	0.003	0.003	0.002	0.001	0.001	0.000	0.000	0.004	0.003	0.001	0.000
Ca^{2+}	0.006	0.000	0.005	0.000	0.001	0.001	0.003	0.000	0.000	0.001	0.000	0.001	0.000	0.000	0.000	0.002	0.001	0.000	0.001	0.000	0.001	0.001	0.001	0.000	0.000	0.002
Ba^{2+}	0.002	0.006	0.005	0.003	0.008	0.005	0.002	0.006	0.000	0.003	0.009	0.002	0.005	0.006	0.006	0.005	0.009	0.005	0.009	0.002	0.007	0.002	0.004	0.010	0.000	0.001
Na^{+}	0.108	0.089	0.082	0.088	0.091	0.084	0.063	0.084	0.094	0.098	0.103	0.066	0.088	0.143	0.129	0.128	0.180	0.185	0.138	0.138	0.167	0.150	0.183	0.134	0.138	0.171
K^{+}	0.808	0.821	0.787	0.815	0.823	0.721	0.776	0.656	0.828	0.811	0.818	0.850	0.818	0.788	0.779	0.757	0.737	0.741	0.786	0.800	0.742	0.783	0.760	0.773	0.789	0.762
Total	7.015	7.010	6.972	6.993	7.028	6.778	6.926	6.662	7.022	6.982	7.003	7.016	7.015	6.988	7.014	7.016	6.987	7.011	6.992	7.031	6.995	7.015	7.016	7.001	6.994	7.006

Table 1. *White mica analyses*

6.1H1B																							
SiO_2	46.200	45.810	46.090	46.630	46.360	46.950	46.440	45.800	46.950	46.460	46.020	45.650	46.450	46.400	46.240	46.070	46.430	46.880	46.710	46.610	46.660	46.450	46.490
$Al2O_3$	34.470	34.040	34.350	34.310	34.980	34.120	33.980	33.480	33.650	33.930	33.360	33.730	34.470	34.020	35.000	34.460	34.320	33.110	33.310	33.290	33.650	33.470	33.800
TiO_2	0.117	0.083	0.054	0.154	0.149	0.116	0.094	0.161	0.063	0.098	0.143	0.126	0.149	0.106	0.111	0.127	0.103	0.128	0.082	0.111	0.110	0.108	0.113
Cr_2O_3	0.091	0.076	0.031	0.040	0.068	0.069	0.055	0.055	0.056	0.085	0.055	0.061	0.000	0.037	0.012	0.045	0.034	0.056	0.062	0.027	0.086	0.046	0.049
MgO	0.691	0.706	0.871	0.765	0.643	0.961	1.074	0.878	1.067	0.961	0.967	0.758	0.577	0.791	0.541	0.585	0.766	1.178	0.960	0.855	0.796	0.892	0.950
FeO	2.260	2.320	2.400	2.340	2.170	2.380	2.420	2.340	2.330	2.400	2.510	2.460	2.230	2.210	2.170	2.310	2.210	2.250	2.240	2.130	2.200	2.350	2.520
MnO	0.000	0.039	0.037	0.039	0.000	0.010	0.011	0.000	0.000	0.000	0.037	0.000	0.018	0.062	0.024	0.000	0.025	0.042	0.000	0.000	0.011	0.019	0.023
CaO	0.038	0.115	0.055	0.027	0.000	0.017	0.032	0.296	0.022	0.012	0.000	0.162	0.019	0.036	0.000	0.083	0.000	0.023	0.008	0.000	0.010	0.000	0.094
BaO	0.168	0.242	0.160	0.146	0.041	0.110	0.155	0.484	0.000	0.312	0.319	0.122	0.187	0.000	0.359	0.025	0.145	0.016	0.295	0.181	0.286	0.209	0.266
Na_2O	1.301	1.370	1.196	1.410	1.380	1.163	1.110	1.140	1.175	1.008	1.162	1.256	1.309	1.242	1.610	1.500	1.331	0.937	1.172	1.305	0.965	1.151	1.125
K_2O	9.080	8.720	9.210	8.940	8.980	9.260	9.190	8.780	9.170	9.360	9.070	8.280	8.760	8.900	8.460	8.450	8.790	9.070	8.780	8.830	8.870	8.930	8.850
Total	94.416	93.521	94.454	94.801	94.771	95.156	94.561	93.414	94.483	94.626	93.643	92.605	94.169	93.804	94.527	93.655	94.154	93.690	93.619	93.339	93.644	93.625	94.280
Cations per 22 oxygens																							
Si^{4+}	3.102	3.108	3.101	3.113	3.091	3.128	3.113	3.113	3.140	3.112	3.119	3.109	3.119	3.127	3.095	3.108	3.117	3.160	3.152	3.155	3.150	3.141	3.129
Al^{IV}	0.898	0.892	0.899	0.887	0.909	0.872	0.887	0.887	0.860	0.888	0.881	0.891	0.881	0.873	0.905	0.892	0.883	0.840	0.848	0.845	0.850	0.859	0.871
Al^{VI}	1.829	1.829	1.824	1.813	1.840	1.806	1.797	1.796	1.793	1.791	1.784	1.816	1.848	1.830	1.855	1.848	1.832	1.790	1.801	1.811	1.827	1.808	1.810
Ti^{4+}	0.006	0.004	0.003	0.008	0.007	0.006	0.005	0.008	0.003	0.005	0.007	0.006	0.008	0.005	0.006	0.006	0.005	0.006	0.004	0.006	0.006	0.005	0.006
Cr^{3+}	0.005	0.004	0.002	0.002	0.004	0.004	0.003	0.003	0.003	0.005	0.003	0.003	0.000	0.002	0.001	0.002	0.002	0.003	0.003	0.001	0.005	0.002	0.003
Mg^{2+}	0.069	0.071	0.087	0.076	0.064	0.095	0.107	0.089	0.106	0.096	0.098	0.077	0.058	0.079	0.054	0.059	0.077	0.118	0.097	0.086	0.080	0.090	0.095
Fe^{2+}	0.127	0.132	0.135	0.131	0.121	0.133	0.136	0.133	0.130	0.134	0.142	0.140	0.125	0.125	0.121	0.130	0.124	0.127	0.126	0.121	0.124	0.133	0.142
Mn^{2+}	0.000	0.002	0.002	0.002	0.000	0.001	0.001	0.000	0.000	0.000	0.002	0.000	0.001	0.004	0.001	0.000	0.001	0.002	0.000	0.000	0.001	0.001	0.001
Ca^{2+}	0.003	0.008	0.004	0.002	0.000	0.001	0.002	0.022	0.002	0.001	0.000	0.012	0.001	0.003	0.000	0.006	0.000	0.002	0.001	0.000	0.001	0.000	0.007
Ba^{2+}	0.004	0.006	0.004	0.004	0.001	0.003	0.004	0.013	0.000	0.008	0.008	0.003	0.005	0.000	0.009	0.001	0.004	0.000	0.008	0.005	0.008	0.006	0.007
Na^{+}	0.169	0.180	0.156	0.183	0.178	0.150	0.144	0.150	0.152	0.131	0.153	0.166	0.171	0.162	0.209	0.196	0.173	0.122	0.153	0.171	0.126	0.151	0.147
K^{+}	0.778	0.755	0.790	0.761	0.764	0.787	0.786	0.761	0.782	0.800	0.784	0.719	0.750	0.765	0.722	0.727	0.753	0.780	0.756	0.762	0.764	0.770	0.760
Total	7.009	6.993	7.007	7.019	7.013	7.002	7.023	7.008	7.021	7.042	7.035	7.000	6.973	6.983	6.991	6.977	6.993	6.986	6.996	6.991	6.958	6.992	6.977

Table 1. *White mica analyses*

Tü 01-4																									
SiO_2	47.000	46.650	47.860	47.090	47.260	47.750	46.790	48.420	47.210	48.730	47.710	47.960	49.130	45.790	49.310	48.190	48.980	48.190	48.750	46.450	44.030	47.320	46.670	47.950	51.450	47.750
$Al2O_3$	28.190	28.310	27.920	28.860	28.970	28.030	30.890	28.390	30.620	28.470	29.360	29.660	28.490	32.980	28.390	28.660	28.770	28.970	28.140	27.210	26.540	28.230	28.620	27.890	29.580	28.370
TiO_2	0.303	0.341	0.175	0.353	0.432	0.208	0.596	0.281	0.511	0.243	0.448	0.491	0.245	0.557	0.298	0.355	0.235	0.364	0.299	0.261	0.274	0.223	0.377	0.245	0.386	0.295
Cr_2O_3	0.069	0.019	0.014	0.065	0.051	0.036	0.027	0.032	0.062	0.036	0.044	0.000	0.030	0.000	0.000	0.113	0.019	0.000	0.064	0.049	0.026	0.000	0.070	0.020	0.060	0.033
MgO	2.890	2.770	2.970	2.830	2.800	2.850	2.060	2.910	2.110	3.040	2.660	2.770	2.930	1.551	3.030	2.670	2.960	2.920	2.930	2.900	2.760	2.750	2.570	2.980	3.110	2.910
FeO	2.860	2.970	2.530	2.740	2.650	2.740	3.160	3.140	3.160	3.260	3.170	3.170	2.980	3.210	3.060	3.370	3.210	3.030	3.140	2.840	2.180	2.570	2.950	2.820	2.990	2.840
MnO	0.041	0.036	0.053	0.023	0.000	0.000	0.000	0.033	0.000	0.095	0.039	0.009	0.015	0.000	0.015	0.036	0.009	0.000	0.044	0.000	0.035	0.048	0.039	0.000	0.000	0.015
CaO	0.000	0.052	0.000	0.000	0.000	0.032	0.019	0.000	0.000	0.000	0.023	0.000	0.016	0.021	0.000	0.040	0.000	0.000	0.014	0.000	0.000	0.000	0.028	0.000	0.010	0.000
BaO	0.218	0.076	0.289	0.212	0.415	0.065	0.313	0.180	0.215	0.230	0.144	0.419	0.243	0.243	0.203	0.129	0.275	0.376	0.366	0.131	0.154	0.368	0.177	0.120	0.324	0.272
Na_2O	0.423	0.488	0.355	0.412	0.415	0.333	0.617	0.371	0.538	0.437	0.565	0.511	0.399	0.386	0.458	0.329	0.392	0.371	0.402	0.407	0.399	0.380	0.518	0.384	0.192	0.448
K_2O	9.100	8.920	9.340	9.240	9.460	9.310	9.650	9.690	9.640	9.890	9.520	9.790	10.030	10.100	10.000	9.630	9.900	9.980	9.880	8.770	8.140	9.380	9.170	9.420	5.630	9.490
Total	91.094	90.632	91.506	91.825	92.453	91.354	94.122	93.447	94.066	94.431	93.683	94.780	94.508	94.838	94.764	93.522	94.750	94.201	94.029	89.018	84.538	91.269	91.189	91.829	93.732	92.423
Cations per 22 oxygens																										
Si^{4+}	3.298	3.277	3.266	3.324	3.258	3.258	3.308	3.181	3.306	3.203	3.296	3.247	3.241	3.317	3.097	3.321	3.286	3.297	3.274	3.316	3.303	3.293	3.289	3.258	3.321	3.387
Al^{IV}	0.702	0.723	0.734	0.676	0.742	0.742	0.692	0.819	0.694	0.797	0.704	0.753	0.759	0.683	0.903	0.679	0.714	0.703	0.726	0.684	0.697	0.707	0.711	0.742	0.679	0.613
Al^{VI}	1.643	1.593	1.602	1.610	1.611	1.611	1.597	1.656	1.591	1.651	1.566	1.602	1.603	1.584	1.725	1.574	1.589	1.579	1.594	1.573	1.583	1.632	1.601	1.613	1.597	1.682
Ti^{4+}	0.012	0.016	0.018	0.009	0.018	0.022	0.011	0.030	0.014	0.026	0.012	0.023	0.025	0.012	0.028	0.015	0.018	0.012	0.019	0.015	0.014	0.015	0.012	0.020	0.013	0.019
Cr^{3+}	0.000	0.004	0.001	0.001	0.004	0.003	0.002	0.001	0.002	0.003	0.002	0.002	0.000	0.002	0.000	0.000	0.006	0.001	0.000	0.003	0.003	0.002	0.000	0.004	0.001	0.003
Mg^{2+}	0.326	0.300	0.289	0.308	0.292	0.288	0.294	0.209	0.296	0.213	0.307	0.270	0.279	0.295	0.156	0.304	0.271	0.297	0.296	0.297	0.307	0.308	0.285	0.268	0.308	0.305
Fe^{2+}	0.119	0.167	0.174	0.147	0.159	0.153	0.159	0.180	0.179	0.179	0.184	0.180	0.179	0.168	0.182	0.172	0.192	0.181	0.172	0.179	0.169	0.136	0.149	0.172	0.163	0.165
Mn^{2+}	0.002	0.002	0.002	0.003	0.001	0.000	0.000	0.000	0.002	0.000	0.005	0.002	0.001	0.001	0.000	0.001	0.002	0.001	0.000	0.003	0.000	0.002	0.003	0.002	0.000	0.000
Ca^{2+}	0.000	0.000	0.004	0.000	0.000	0.000	0.002	0.001	0.000	0.000	0.000	0.002	0.000	0.001	0.002	0.000	0.003	0.000	0.000	0.001	0.000	0.000	0.000	0.002	0.000	0.001
Ba^{2+}	0.005	0.006	0.002	0.008	0.006	0.011	0.002	0.008	0.005	0.006	0.006	0.004	0.011	0.006	0.006	0.005	0.003	0.007	0.010	0.010	0.004	0.005	0.010	0.005	0.003	0.008
Na^{+}	0.049	0.057	0.066	0.048	0.055	0.055	0.045	0.081	0.049	0.071	0.057	0.075	0.067	0.052	0.051	0.060	0.044	0.051	0.049	0.053	0.056	0.058	0.051	0.070	0.052	0.025
K^{+}	0.761	0.809	0.797	0.828	0.815	0.832	0.823	0.837	0.844	0.834	0.853	0.827	0.844	0.864	0.871	0.859	0.838	0.850	0.865	0.857	0.795	0.776	0.832	0.817	0.832	0.473
Total	6.927	7.005	7.004	6.961	7.000	6.995	7.004	7.014	6.983	7.011	7.028	7.017	7.009	7.004	7.022	7.003	6.996	7.022	7.004	6.997	7.004	6.944	7.026	6.999	6.970	6.707

Table 1. *White mica analyses*

Tü 01-8																									
SiO_2	35.290	45.790	44.980	44.920	44.660	45.740	44.810	46.150	46.990	45.270	45.250	62.190	98.540	43.980	47.160	45.970	35.330	45.250	45.700	45.660	46.380	46.910	46.140	47.260	45.240	45.650
$Al2O_3$	18.170	35.600	36.590	34.070	34.970	33.250	33.380	33.720	33.670	34.360	32.980	22.830	0.042	35.740	31.720	35.650	17.950	35.290	34.280	34.270	32.930	33.770	34.140	31.770	35.830	35.220
TiO_2	1.680	0.385	0.419	0.391	0.402	0.374	0.409	0.444	0.414	0.417	0.416	0.032	0.000	0.358	0.417	0.361	1.700	0.361	0.442	0.404	0.411	0.411	0.423	0.403	0.410	0.378
Cr_2O_3	0.107	0.067	0.085	0.101	0.022	0.073	0.095	0.058	0.060	0.009	0.047	0.000	0.010	0.075	0.039	0.082	0.009	0.043	0.091	0.086	0.036	0.065	0.044	0.026	0.054	0.057
MgO	11.010	0.947	0.714	1.523	1.220	1.161	1.483	1.609	1.547	1.421	1.750	0.009	0.000	0.976	2.190	0.882	10.970	1.142	1.375	1.460	1.690	1.211	1.399	2.110	1.091	1.050
FeO	17.480	1.245	1.101	1.670	1.570	1.640	1.720	1.620	1.630	1.540	1.610	0.009	0.095	1.228	1.870	1.400	16.710	1.500	1.550	1.520	1.860	1.520	1.470	2.230	1.410	1.510
MnO	0.024	0.013	0.000	0.009	0.000	0.000	0.000	0.030	0.000	0.000	0.000	0.000	0.034	0.000	0.000	0.032	0.070	0.011	0.000	0.000	0.000	0.000	0.010	0.035	0.000	0.000
CaO	0.119	0.009	0.000	0.000	0.008	0.000	0.015	0.000	0.021	0.000	0.000	3.890	0.009	0.000	0.000	0.000	0.149	0.000	0.035	0.000	0.016	0.140	0.020	0.000	0.050	0.010
BaO	0.227	0.853	0.870	0.390	0.374	0.384	0.401	0.431	0.522	0.375	0.166	0.000	0.164	0.610	0.000	0.419	0.025	0.540	0.439	0.378	0.269	0.592	0.401	0.293	0.788	0.585
Na_2O	0.091	0.834	1.293	1.036	1.328	1.216	1.123	1.122	1.055	1.124	0.868	9.640	0.000	1.063	0.667	0.874	0.262	1.122	1.282	1.014	1.113	1.460	0.902	0.863	1.285	1.131
K_2O	8.830	9.350	8.710	9.610	8.820	9.140	9.330	9.500	9.760	9.640	9.600	0.104	0.025	9.760	10.150	9.670	8.870	9.650	9.310	8.670	9.370	9.430	9.640	9.780	9.120	9.650
Total	93.028	95.093	94.762	93.720	93.374	92.978	92.766	94.684	95.669	94.156	92.687	98.704	98.919	93.790	94.213	95.340	92.045	94.909	94.504	93.462	94.075	95.509	94.589	94.770	95.278	95.241
Cations per 22 oxygens																										
Si^{4+}	2.719	3.057	3.004	3.051	3.032	3.121	3.072	3.100	3.126	3.060	3.101	3.834	5.490	2.991	3.182	3.059	2.736	3.037	3.073	3.086	3.132	3.125	3.098	3.178	3.020	3.052
Al^{IV}	1.281	0.943	0.996	0.949	0.968	0.879	0.928	0.900	0.874	0.940	0.899	0.166	0.000	1.009	0.818	0.941	1.264	0.963	0.927	0.914	0.868	0.875	0.902	0.822	0.980	0.948
Al^{VI}	0.369	1.859	1.884	1.778	1.830	1.795	1.768	1.770	1.766	1.798	1.764	1.492	0.003	1.856	1.705	1.855	0.375	1.828	1.790	1.816	1.753	1.777	1.799	1.695	1.839	1.827
Ti^{4+}	0.097	0.019	0.021	0.020	0.021	0.019	0.021	0.022	0.021	0.021	0.021	0.001	0.000	0.018	0.021	0.018	0.099	0.018	0.022	0.021	0.021	0.021	0.021	0.020	0.021	0.019
Cr^{3+}	0.007	0.004	0.004	0.005	0.001	0.004	0.005	0.003	0.003	0.000	0.003	0.000	0.000	0.004	0.002	0.004	0.001	0.002	0.005	0.005	0.002	0.003	0.002	0.001	0.003	0.003
Mg^{2+}	1.265	0.094	0.071	0.154	0.123	0.118	0.152	0.161	0.153	0.143	0.179	0.001	0.000	0.099	0.220	0.088	1.267	0.114	0.138	0.147	0.170	0.120	0.140	0.212	0.109	0.105
Fe^{2+}	1.126	0.070	0.061	0.095	0.089	0.094	0.099	0.091	0.091	0.087	0.092	0.000	0.004	0.070	0.106	0.078	1.082	0.084	0.087	0.086	0.105	0.085	0.083	0.125	0.079	0.084
Mn^{2+}	0.002	0.001	0.000	0.001	0.000	0.000	0.000	0.002	0.000	0.000	0.000	0.000	0.002	0.000	0.000	0.002	0.005	0.001	0.000	0.000	0.000	0.000	0.001	0.002	0.000	0.000
Ca^{2+}	0.010	0.001	0.000	0.000	0.001	0.000	0.001	0.000	0.001	0.000	0.000	0.257	0.001	0.000	0.000	0.000	0.012	0.000	0.003	0.000	0.001	0.010	0.001	0.000	0.004	0.001
Ba^{2+}	0.007	0.022	0.023	0.010	0.010	0.010	0.011	0.011	0.014	0.010	0.004	0.000	0.004	0.016	0.000	0.011	0.001	0.014	0.012	0.010	0.007	0.015	0.011	0.008	0.021	0.015
Na^{+}	0.014	0.108	0.168	0.136	0.175	0.161	0.149	0.146	0.136	0.147	0.115	1.153	0.000	0.140	0.087	0.113	0.039	0.146	0.167	0.133	0.146	0.189	0.117	0.113	0.166	0.147
K^{+}	0.868	0.796	0.742	0.833	0.764	0.796	0.816	0.814	0.828	0.831	0.839	0.008	0.002	0.847	0.874	0.821	0.876	0.826	0.799	0.748	0.807	0.801	0.826	0.839	0.777	0.823
Total	7.829	6.973	7.000	7.063	7.020	7.002	7.056	7.021	7.015	7.039	7.027	6.919	5.513	7.050	7.015	6.989	7.849	7.034	7.030	6.967	7.012	7.022	7.001	7.022	7.023	7.025

Table 1. *White mica analyses*

Tü 01-9																									
SiO_2	48.330	48.650	46.040	48.560	48.090	48.410	48.820	48.250	48.700	48.230	47.700	48.790	47.030	48.030	48.360	99.840	48.760	48.910	48.200	49.340	47.130	48.810	47.640	49.040	48.970	48.360
$Al2O_3$	28.520	28.720	29.720	28.900	29.420	28.810	28.530	28.110	28.860	28.190	29.240	28.400	29.810	29.090	28.570	0.020	28.240	28.440	28.830	28.210	29.870	28.130	28.880	28.610	28.650	28.750
TiO_2	0.484	0.487	0.717	0.573	0.907	0.595	0.442	0.521	0.458	0.554	0.803	0.551	0.771	0.737	0.527	0.000	0.567	0.461	0.766	0.538	0.749	0.521	0.929	0.469	0.602	0.680
Cr_2O_3	0.013	0.075	0.049	0.000	0.071	0.000	0.019	0.031	0.028	0.044	0.046	0.040	0.050	0.112	0.021	0.018	0.000	0.000	0.034	0.042	0.074	0.061	0.057	0.000	0.087	0.000
MgO	2.570	2.540	1.950	2.440	2.160	2.280	2.260	2.400	2.390	2.230	2.060	2.280	1.910	2.300	2.190	0.000	2.450	2.550	2.280	2.630	1.930	2.500	2.160	2.350	2.400	2.270
FeO	4.520	4.450	4.880	4.140	4.480	4.730	4.960	4.580	4.400	4.880	4.570	4.790	4.680	4.560	4.650	0.044	4.360	4.640	4.430	4.570	4.280	4.610	4.320	4.640	4.780	4.570
MnO	0.000	0.000	0.057	0.000	0.062	0.076	0.000	0.000	0.039	0.000	0.024	0.000	0.074	0.020	0.009	0.029	0.018	0.015	0.000	0.046	0.000	0.000	0.000	0.028	0.000	0.000
CaO	0.009	0.034	0.047	0.049	0.000	0.031	0.018	0.000	0.010	0.010	0.007	0.000	0.000	0.017	0.020	0.010	0.024	0.000	0.012	0.017	0.000	0.000	0.047	0.000	0.000	0.000
BaO	0.438	0.529	0.300	0.346	0.558	0.384	0.384	0.296	0.357	0.460	0.496	0.281	0.431	0.234	0.173	0.000	0.512	0.230	0.332	0.274	0.221	0.394	0.359	0.394	0.006	0.338
Na_2O	0.298	0.269	0.296	0.265	0.314	0.342	0.227	0.241	0.257	0.322	0.280	0.253	0.378	0.296	0.238	0.000	0.241	0.333	0.311	0.279	0.375	0.320	0.334	0.326	0.287	0.336
K_2O	10.340	10.200	9.530	10.470	10.200	10.220	10.420	10.580	10.540	10.200	10.660	10.470	10.500	10.450	10.670	0.000	10.120	10.470	10.510	10.500	10.540	10.490	10.520	10.680	10.460	10.430
Total	95.522	95.954	93.586	95.743	96.262	95.878	96.080	95.009	96.039	95.120	95.886	95.855	95.634	95.846	95.428	99.961	95.292	96.049	95.705	96.446	95.169	95.836	95.246	96.537	96.242	95.734
Cations per 22 oxygens																										
Si^{4+}	3.270	3.275	3.176	3.267	3.230	3.265	3.286	3.284	3.274	3.283	3.228	3.285	3.193	3.240	3.277	5.496	3.299	3.285	3.257	3.302	3.202	3.292	3.236	3.288	3.281	3.266
Al^{IV}	0.730	0.725	0.824	0.733	0.770	0.735	0.714	0.716	0.726	0.717	0.772	0.715	0.807	0.760	0.723	0.000	0.701	0.715	0.743	0.698	0.798	0.708	0.764	0.712	0.719	0.734
Al^{VI}	1.544	1.553	1.591	1.559	1.558	1.555	1.550	1.539	1.561	1.544	1.560	1.538	1.578	1.553	1.558	0.001	1.551	1.537	1.552	1.528	1.594	1.528	1.549	1.549	1.543	1.554
Ti^{4+}	0.025	0.025	0.037	0.029	0.046	0.030	0.022	0.027	0.023	0.028	0.041	0.028	0.039	0.037	0.027	0.000	0.029	0.023	0.039	0.027	0.038	0.026	0.047	0.024	0.030	0.035
Cr^{3+}	0.001	0.004	0.003	0.000	0.004	0.000	0.001	0.002	0.001	0.002	0.002	0.002	0.003	0.006	0.001	0.001	0.000	0.000	0.002	0.002	0.004	0.003	0.003	0.000	0.005	0.000
Mg^{2+}	0.259	0.255	0.201	0.245	0.216	0.229	0.227	0.244	0.240	0.226	0.208	0.229	0.193	0.231	0.221	0.000	0.247	0.255	0.230	0.262	0.195	0.251	0.219	0.235	0.240	0.229
Fe^{2+}	0.256	0.250	0.281	0.233	0.252	0.267	0.279	0.261	0.247	0.278	0.259	0.270	0.266	0.257	0.263	0.002	0.247	0.261	0.250	0.256	0.243	0.260	0.245	0.260	0.268	0.258
Mn^{2+}	0.000	0.000	0.003	0.000	0.004	0.004	0.000	0.000	0.002	0.000	0.001	0.000	0.004	0.001	0.001	0.001	0.001	0.001	0.000	0.003	0.000	0.000	0.000	0.002	0.000	0.000
Ca^{2+}	0.001	0.002	0.003	0.004	0.000	0.002	0.001	0.000	0.001	0.001	0.001	0.000	0.000	0.001	0.001	0.001	0.002	0.000	0.001	0.001	0.000	0.000	0.003	0.000	0.000	0.000
Ba^{2+}	0.012	0.014	0.008	0.009	0.015	0.010	0.010	0.008	0.009	0.012	0.013	0.007	0.011	0.006	0.005	0.000	0.014	0.006	0.009	0.007	0.006	0.010	0.010	0.010	0.000	0.009
Na^{+}	0.039	0.035	0.040	0.035	0.041	0.045	0.030	0.032	0.034	0.043	0.037	0.033	0.050	0.039	0.031	0.000	0.032	0.043	0.041	0.036	0.049	0.042	0.044	0.042	0.037	0.044
K^{+}	0.892	0.876	0.838	0.899	0.874	0.879	0.895	0.919	0.904	0.886	0.920	0.899	0.909	0.899	0.922	0.000	0.873	0.897	0.906	0.896	0.913	0.902	0.912	0.913	0.894	0.898
Total	7.040	7.015	7.028	7.038	7.023	7.023	7.028	7.043	7.033	7.021	7.043	7.046	7.054	7.032	7.034	5.503	7.002	7.049	7.029	7.028	7.043	7.045	7.041	7.036	7.025	7.027

Table 1. *White mica analyses*

Tü 01-10																									
SiO_2	46.400	44.400	46.760	43.970	44.540	44.670	46.890	45.520	45.500	46.640	47.470	46.970	46.400	47.420	46.040	46.500	47.070	47.440	47.380	46.870	47.400	46.400	47.660	46.290	46.300
$Al2O_3$	29.220	30.610	28.920	30.060	31.450	28.170	29.450	30.580	29.970	29.370	28.210	28.750	29.450	28.980	29.920	30.110	28.490	29.130	28.350	30.190	28.450	29.190	28.790	30.130	29.800
TiO_2	0.699	0.634	0.445	0.646	0.531	0.681	0.298	0.868	0.703	0.259	0.484	0.465	0.361	0.489	0.805	0.719	0.532	0.297	0.366	0.600	0.365	0.660	0.394	0.818	0.677
Cr_2O_3	0.000	0.036	0.061	0.000	0.042	0.029	0.038	0.069	0.026	0.000	0.000	0.000	0.066	0.072	0.063	0.061	0.024	0.028	0.036	0.018	0.100	0.020	0.019	0.055	0.053
MgO	2.650	2.110	2.660	2.330	1.950	2.390	2.480	2.100	2.210	2.540	2.630	2.790	2.710	2.600	2.220	2.270	2.750	2.570	2.610	2.300	2.720	2.490	2.670	2.130	2.280
FeO	4.210	3.930	3.700	3.930	4.000	3.810	4.010	3.950	4.070	3.800	3.810	3.650	3.800	3.890	3.990	3.840	3.890	3.600	3.560	4.230	3.930	3.860	3.950	3.950	4.240
MnO	0.000	0.000	0.000	0.000	0.000	0.025	0.059	0.034	0.039	0.000	0.000	0.017	0.000	0.034	0.000	0.000	0.016	0.000	0.013	0.000	0.000	0.022	0.012	0.000	0.000
CaO	0.037	0.016	0.013	0.000	0.000	0.000	0.012	0.000	0.000	0.012	0.000	0.000	0.000	0.015	0.000	0.014	0.000	0.010	0.019	0.000	0.011	0.000	0.010	0.000	0.030
BaO	0.000	0.161	0.311	0.231	0.158	0.000	0.000	0.101	0.044	0.116	0.164	0.157	0.018	0.138	0.000	0.102	0.113	0.027	0.243	0.132	0.028	0.190	0.076	0.130	0.226
Na_2O	0.429	0.360	0.368	0.419	0.368	0.353	0.448	0.459	0.424	0.366	0.509	0.360	0.308	0.487	0.411	0.453	0.417	0.385	0.423	0.440	0.373	0.340	0.410	0.378	0.431
K_2O	10.500	10.800	10.430	10.730	10.950	10.380	10.730	10.700	10.770	10.900	10.510	10.800	10.920	10.550	11.090	10.840	10.650	10.660	10.430	10.780	10.730	10.920	10.550	10.740	10.660
Total	94.145	93.057	93.668	92.316	93.989	90.508	94.415	94.381	93.756	94.003	93.787	93.959	94.033	94.675	94.539	94.909	93.952	94.147	93.430	95.560	94.107	94.092	94.541	94.621	94.697
Cations per 22 oxygens																									
Si^{4+}	3.187	3.098	3.221	3.095	3.075	3.187	3.208	3.121	3.139	3.208	3.262	3.226	3.188	3.233	3.157	3.164	3.231	3.243	3.265	3.171	3.247	3.190	3.246	3.160	3.169
Al^{IV}	0.813	0.902	0.779	0.905	0.925	0.813	0.792	0.879	0.861	0.792	0.738	0.774	0.812	0.767	0.843	0.836	0.769	0.757	0.735	0.829	0.753	0.810	0.754	0.840	0.831
Al^{VI}	1.553	1.615	1.568	1.588	1.634	1.555	1.582	1.592	1.576	1.589	1.547	1.552	1.572	1.561	1.574	1.579	1.535	1.591	1.567	1.578	1.544	1.555	1.556	1.584	1.573
Ti^{4+}	0.036	0.033	0.023	0.034	0.028	0.037	0.015	0.045	0.036	0.013	0.025	0.024	0.019	0.025	0.042	0.037	0.027	0.015	0.019	0.031	0.019	0.034	0.020	0.042	0.035
Cr^{3+}	0.000	0.002	0.003	0.000	0.002	0.002	0.002	0.004	0.001	0.000	0.000	0.000	0.004	0.004	0.003	0.003	0.001	0.002	0.002	0.001	0.005	0.001	0.001	0.003	0.003
Mg^{2+}	0.271	0.219	0.273	0.244	0.201	0.254	0.253	0.215	0.227	0.260	0.269	0.286	0.278	0.264	0.227	0.230	0.281	0.262	0.268	0.232	0.278	0.255	0.271	0.217	0.233
Fe^{2+}	0.242	0.229	0.213	0.231	0.231	0.227	0.229	0.226	0.235	0.219	0.219	0.210	0.218	0.222	0.229	0.219	0.223	0.206	0.205	0.239	0.225	0.222	0.225	0.225	0.243
Mn^{2+}	0.000	0.000	0.000	0.000	0.000	0.002	0.003	0.002	0.002	0.000	0.000	0.001	0.000	0.002	0.000	0.000	0.001	0.000	0.001	0.000	0.000	0.001	0.001	0.000	0.000
Ca^{2+}	0.003	0.001	0.001	0.000	0.000	0.000	0.001	0.000	0.000	0.001	0.000	0.000	0.000	0.001	0.000	0.001	0.000	0.001	0.001	0.000	0.001	0.000	0.001	0.000	0.002
Ba^{2+}	0.000	0.004	0.008	0.006	0.004	0.000	0.000	0.003	0.001	0.003	0.004	0.004	0.000	0.004	0.000	0.003	0.003	0.001	0.007	0.003	0.001	0.005	0.002	0.003	0.006
Na^{+}	0.057	0.049	0.049	0.057	0.049	0.049	0.059	0.061	0.057	0.049	0.068	0.048	0.041	0.064	0.055	0.060	0.056	0.051	0.057	0.058	0.050	0.045	0.054	0.050	0.057
K^{+}	0.920	0.961	0.916	0.963	0.964	0.945	0.936	0.936	0.948	0.956	0.921	0.946	0.957	0.917	0.970	0.941	0.932	0.930	0.917	0.930	0.938	0.958	0.916	0.935	0.931
Total	7.082	7.114	7.072	7.144	7.133	7.108	7.092	7.108	7.132	7.091	7.075	7.097	7.108	7.070	7.108	7.108	7.106	7.057	7.058	7.104	7.093	7.113	7.079	7.093	7.091